1064 nm injection mode-locked Nd:YAG laser optimized for guide star applications

by

Thomas P. Rutten

Thesis submitted for the degree of
Doctor of Philosophy
in
the University of Adelaide
Department of Physics
December, 2009

Contents

Abstract

In recent years, the emergence of powerful, sodium-resonant laser sources has led to a dramatic improvement in resolution at many of the world's large aperture observatories. The lasers are used to create artificial beacons (or guide stars) by fluorescing atmospheric sodium. Light from the beacon, returning from altitude, probes the intervening turbulence and the phase distortions detected are subsequently corrected using adaptive optics. Near-diffraction limited imaging has now been achieved on observatories with diameters up to 8 m using this technique. Future 30-100 m diameter telescopes will require new laser sources having higher average powers and innovative pulse formats to implement new forms of atmospheric tomography and correction. In this thesis I present the design and development of a new laser system for this purpose.

The laser design that I describe uses sum frequency generation (SFG) of 1064 nm and 1319 nm Nd:YAG lasers to produce the sodium wavelength, and introduces the novel application of injection mode-locking as a robust method to control the lasers wavelength and bandwidth. The high peak power and low timing jitter of the mode-locked (micro) pulses allows for efficient SFG of the 1064 and 1319 nm beams. Each slave laser is Q-switched and the duration of the Q-switched (macro) pulses are optimised to reduce star elongation and bleaching of the sodium.

The experimental work presented in this thesis is focused on the realization of a 1064 nm injection mode-locked slave laser, whose performance is optimised for use in the SFG guide star system. The work can be roughly divided into two sections. Firstly, results are presented from a low average power proof of principle laser which was used for risk reduction experiments, then secondly, a higher average power laser using a new laser head design is presented.

With the proof of concept laser it is shown that the injection mode-locking technique is robust and can be used to generate an ideal pulse burst with both wavelength and bandwidth control. A new method of Q-switched pulse stretching was implemented and the results show that the Q-switched pulses can be extended by a factor of 4.5 without a reduction in pulse energy.

The later part of the experimental work consists of a description of the design, construction and testing of a new high average power laser head used to generate the power levels required for the final guide star system. The laser head uses a zigzag Nd:YAG slab, pumped from each side by high average power laser diode arrays. This laser is shown to be capable of generating one of the highest average powers reported in the literature for an electro-optically Q-switched, diffraction limited Nd:YAG laser in a stable cavity.

This work contains no material which has been accepted for the award of any other degree or diploma in any university or other tertiary institution to Thomas Rutten and, to the best of my knowledge and belief, contains no material previously published or written by another person, except where due reference has been made in the text.

I give consent to this copy of my thesis when deposited in the University Library, being made available for loan and photocopying, subject to the provisions of the Copyright Act 1968. The author acknowledges that copyright of published works contained within this thesis (as listed below) resides with the copyright holder(s) of those works.

I also give permission for the digital version of my thesis to be made available on the web, via the Universitys digital research repository, the Library catalogue, the Australasian Digital Theses Program (ADTP) and also through web search engines, unless permission has been granted by the University to restrict access for a period of time.

Publications resulting from this work:

- T. P. Rutten, P. J. Veitch, C. d'Orgeville and J. Munch, "Injection mode-locked guide star laser concept and design verification experiments," Opt. Express vol. 15 (5), pp. 2369-2374 Mar. 2007.
- T. P. Rutten, N. Wild and P. J. Veitch, "Fast rise time, long pulse width, kilohertz repetition rate Q-switch driver," Rev. Sci. Instrum. vol. 78, 073108 Jun. 2007.
- T. P. Rutten, P. J. Veitch and J. Munch, "Efficient pulse stretching of Q-switched lasers," IEEE J. Quantum Electron. vol. 44 (10), pp. 911-915 Oct. 2008.
- J. Munch, T. P. Rutten, N. Simakov, M. Hamilton, C. d'Orgeville and P. Veitch, "A new guide star laser using optimized injection mode-locking," Proc. SPIE, vol. 7015, June 2008

SIGNED: ....
DATE: ....

Supervisors: Prof. J. Munch and A/Prof. P. Veitch

Acknowledgments

It is tough road to travel when undertaking a PhD. When I first started, I stood back and observed what seemed to be an impenetrable wilderness, with tangled undergrowth and dangerous creatures lurking within. My supervisors, Jesper and Peter were the first to show me where I had to go. They pointed to a region far on the horizon and, with promises of great rewards and adventure, they showed me the direction in which to travel and set me upon the road to completion. Thank you Jesper and Peter for your guidance and support, without your help I would surely have been lost along the way.

To my colleagues in the optics group: Alex H, Alex D, Damian M, David H, Francois, Keiron, Nikita, Miftar, Nick, Sean, Shu, Aidan, Mathew and Ka, you provided so much helpful advice, thankyou for your assistance and for providing a place to rest where I could forget about work and relax.

Damien, Murray and Dave O., we had many helpful discussions and you contributed a great deal to the solution of many important problems I faced.

I would also like to thank all the technical staff who provided assistance with this project. Neville, I am deeply indebted to you for being so generous with your time and for having the patience to teach me. To Blair and Trevor, your assistance in the workshop was essential and without your assistance I could not have progressed. I also thank the two Bobs and Peter A. for the excellent contributions and advice you gave.

To Eva and my colleagues at the RAH, your encouragement and support while writing was greatly appreciated.

I would like to thank the Gemini Observatory for providing funding for this work and Northrop Grumman for the loan of vital hardware.

Lastly I would like to thank my Family and friends. You provided the personal support and encouragement I needed to stick to my goals and keep going when times were tough. Thank you.

Chapter 1

Adaptive optics systems for astronomy

1.1 Introduction

Were it not for the last millisecond of its long journey through space, the light from distant stars, emitted some millions of years earlier, would descend upon the Earths surface in perfect plane waves and be focused by our telescopes with diffraction limited resolution. In that last millisecond, unfortunately, the light must pass through a thin but turbulent atmosphere, whose constant motions convey a time varying phase shift to wavefronts of passing light. The distortion in phase is only small, around 2 wavelengths pk-pk at 2 μm over an 8 m aperture [1], but this slight change is enough to blur the images of ground based telescopes. A consequence of this effect is that there is a limit to the maximum resolution achievable by ground based telescopes that is independent of the telescope diameter. If there were no atmospheric turbulence, the angular resolution θ of a diffraction limited telescope would scale as the inverse of the telescope diameter, D, according to the well known formula $1.22\lambda/D$, but in the presence of turbulence, the maximum resolution is limited by the "seeing" of the atmosphere and is given by $\theta = 1.22\lambda/r_0$, where r_0 is Fried's coherence length and is a measure of the seeing at a specific location [2]. For this reason, many of the world's best observatories are located atop tall mountains where the thinner air affords better seeing. But even at the best locations, such as Mauna Kea in Hawaii, the Fried's parameter is typically around 10-20 cm [3]. This means that a telescope with a diameter larger than this, while providing an increased capacity to view dim objects, will not have any improvement in resolution unless, of course, the telescope mirror is actively compensated for the turbulence using adaptive optics.

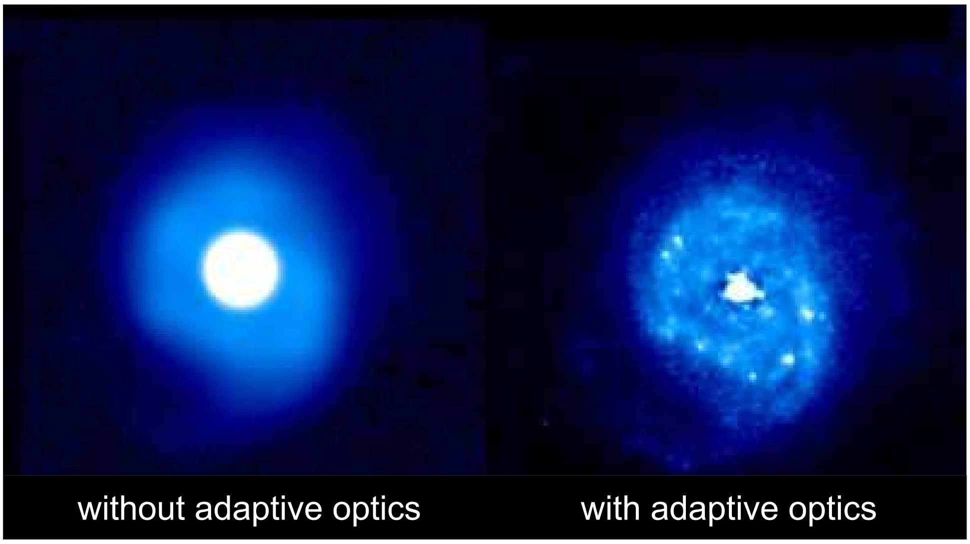

Figure 1.1: Image credit: the Gemini Observatory. Dramatic differences in image quality can be obtained by actively compensating for the effects of atmospheric turbulence using adaptive optics.

The concept of atmospheric adaptive optics was first proposed by Babcock in 1953 [4] and later developed by Fried [2], Greenwood [5], Thompson and Gardner [6], Fugate et al. [7], Primmerman et al. [8] and others. The technique involves measuring the atmospheric distortion by monitoring the phase fronts of light from a reference star (or guide star) near the science object, computing the amount of compensation required, then applying this compensation to a deformable telescope mirror to shape the surface to the conjugate of the incident wavefronts and thereby restore the plane waves of the distant source for diffraction limited observations. A demonstration of the power of adaptive optics can be seen in the images of Figure 1.1 which shows the difference in resolution obtainable by correcting for atmospheric turbulence.

In this chapter an overview of current and future adaptive optics systems is presented, with a particular emphasis on the laser systems required to generate the reference beacons for these systems. Current adaptive optics systems are described in Section 1.2 and the lasers for these systems are presented in Section 1.3. Both Rayleigh and Sodium beacons are discussed and the present research on Sodium lasers is summarized.

Section 1.4.1 describes the next generation of adaptive optics systems, being planned for use on future large aperture observatories. The laser systems required by these systems have yet to be developed. Laser requirements from the Gemini observatory are listed in Section 1.4.2 and an explanation of the these requirements is given. Finally, in Section 1.5, an outline of this thesis is presented that describes the work undertaken by the author to develop a new type of laser system aimed at meeting the Gemini requirements for future

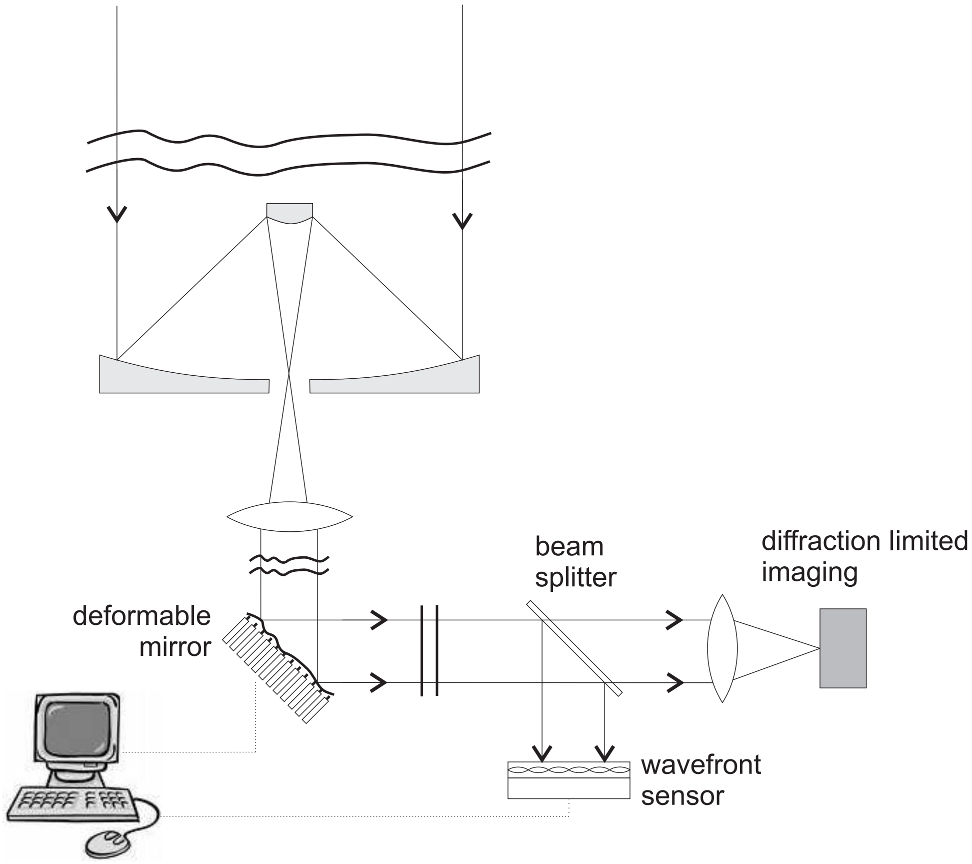

Figure 1.2: A simplified diagram of an astronomical adaptive optics system showing the wavefront sensor, deformable mirror and control system used for correction of atmospheric turbulence.

large aperture adaptive optics systems.

1.2 Conventional single-conjugate adaptive optics systems

Single conjugate adaptive optics systems have now been fitted on most of the world's large diameter telescopes including Lick, Gemini, Keck, SOR, ESO, Subaru and Mt. Palomar. Each system has its own particular variations but most conform to the common generalization depicted in Figure 1.2.

Key components of the system include a wavefront sensor to measure the atmospheric distortion, a deformable mirror to correct it and a computer system to link the two.

Light from a reference beacon located close to the science object is collected by the telescope primary mirror and directed onto the deformable mirror as shown. The deformable mirror is usually 10-40 cm in diameter and consists of a thin reflective membrane dis-

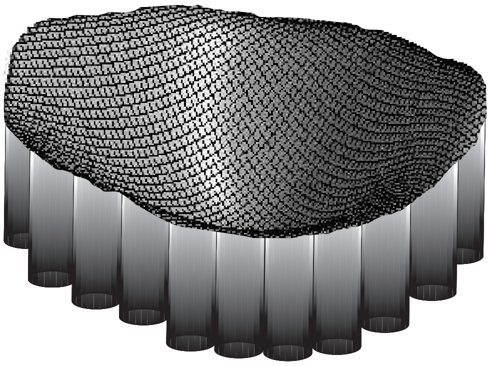

Figure 1.3: A schematic representation of a deformable mirror consisting of a continuous faceplate sitting atop an array of piezo electric actuators.

tributed over an array of (usually piezo-electric) actuators as shown in Figure 1.3. The number of actuators in the deformable mirror is a trade-off between the level of correction required and the corresponding impact on system complexity and budgetary constraints. The number of actuators used in present systems ranges from around 100 to as many as 1377, used by the ESO.

A Shack-Hartmann wavefront sensor is often used for the wavefront measurements as these systems provide high signal to noise ratios in low light conditions [9]. A schematic diagram outlining the principle of this device is shown in Figure 1.4. Incident wavefronts from the guide star are directed onto an array of lenslets which focus the light into a series of spots that are detected by a CCD. A computer algorithm is then used to locate the centroids of the spots. The relative change in spot location represents the slope of the wavefront incident on each lenslet. By collating the information from each lenslet, the shape of the entire wavefront can be reconstructed, showing the change in phase caused by the turbulence. This information is then fed back to the deformable mirror which adjusts its contour to cancel the changes and generate a near plane wave that is incident on the sensor.

The success of the adaptive optics system is dependent on having a suitably bright reference star (magnitude 12 or brighter [10]) within an isoplanatic angle[1] of the science object. This star must be sufficiently bright that enough photons are recorded at the wavefront sensor to provide a sufficient signal to noise ratio within the time period dictated by the bandwidth of the adaptive optics system ($\approx$ 1 ms). This represents a major limitation to systems using natural guide stars, as the number of suitably bright stars is relatively few, resulting in a sky coverage of less than 1 % [11]. This problem has led to

---

[1] The isoplanatic angle is another measure of atmospheric seeing and represents the angle over which wavefronts can pass through the atmosphere suffering only minimal distortion

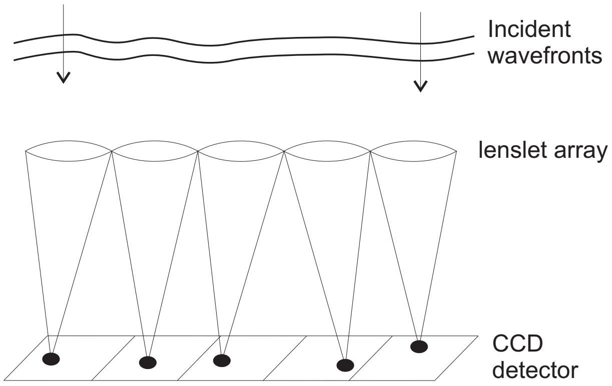

Figure 1.4: A 2-D view of a Shack-Hartmann interferometer showing the wavefronts incident on a lenslet array which focus the light into a series of spots read by the detector. The location of the spot provides information on the slope of the incident wavefront at a particular lenslet.

the conception of artificial guide stars, created by powerful laser beams directed into the sky in the vicinity of the science object.

1.3 Artificial guide stars

The first public report detailing the feasibility of generating an artificial guide star using a laser was published by Foy and Labeyrie in 1985 [12] although credit for the idea has also been given to Happer and MacDonald from the U.S. Department of Defence for a confidential military report in 1983 [7]. The first detailed experiments on laser guide stars were presented by Thompson and Gardner [6] in 1987 before the U.S. Department of Defence declassified much of its experimental work into laser guide star systems resulting in the publication of results from the first adaptive optics system to use an artificial beacon generated by Rayleigh scatter to compensate for atmospheric distortion in 1991 [7] [8]. Results of the first turbulence measurements using a sodium layer beacon were also released in 1991 with the report by Humphreys et al. [13]. Rayleigh and sodium guide stars are both discussed in this section.

1.3.1 Rayleigh guide stars

Rayleigh guide stars are generated by the Rayleigh backscatter from laser light in the lower atmosphere. The advantage of using this approach is that there is no specific requirement on the wavelength of the laser source, other than that it should have a short wavelength (the magnitude of Rayleigh scatter depends inversely on the fourth power of wavelength)

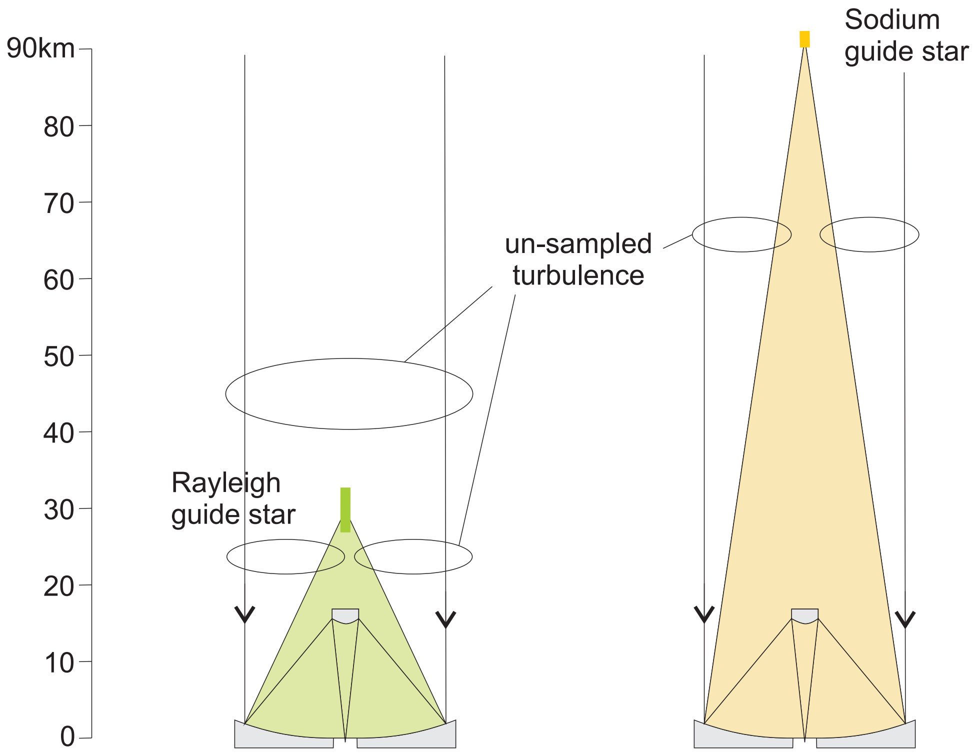

Figure 1.5: The low altitude of guide stars generated by Rayleigh scatter results large sections of the atmosphere that are not sampled. This phenomenon is known as focus anisoplanatism (or the cone effect) as the beacon is located at a different focus to the science object. Sodium guide stars ameliorate the problem to a certain extent, but the field of view is still limited and there are some sections of the atmosphere that cannot be compensated using a single guide star. This problem gets worse for larger aperture observatories

so mature and relatively inexpensive laser technology can be used such as frequency doubled Nd:YAG at 532 nm. A limitation of this technique is that Rayleigh scatter is primarily concentrated in the lower 20-30 km of the atmosphere where the air is densest, and the resulting close proximity of the beacon to the telescope means that turbulence in the upper atmosphere cannot be corrected and the level of image correction reduces rapidly in regions away from the beacon. This phenomena, known as focus anisoplanatism or the cone effect (see Figure 1.5), is worse for large aperture observatories.

1.3.2 Sodium guide stars

An improvement on the early Rayleigh guide stars was the shift to sodium guide stars which rely on resonant excitation of the sodium atoms in the upper atmosphere to generate the beacon [14]. The high altitude of the sodium layer (90-100 km) provides a reduction in focus anisoplanatism, but comes with an increase in laser system complexity as the laser wavelength must be tuned to the exact resonant frequency of sodium (589.159 nm). Generating light at the sodium wavelength with sufficient power to produce a reference beacon bright enough to adequately illuminate a wavefront sensor is no trivial task, however, and numerous laser system designs have been proposed and used to address this problem.

Current status of sodium guide star laser systems

The first sodium laser guide star adaptive optics system to be used routinely for astronomical imaging was installed on the 3 m Shane telescope at the Lick observatory in 1995 [15] [16]. This system used a pulsed dye laser, initially designed by LLNL for use in its isotope separation program, which was capable of delivering 20 W of 589 nm laser power with 100 ns pulses at a repetition rate of 10 kHz. Since this time, research has moved towards the development of sum frequency Nd:YAG lasers owing to the reliability and longevity of these lasers. Research was first performed by Jeys et al. [17] who made use of the fact that, coincidentally, the two strongest laser lines of Nd:YAG (1064 nm and 1319 nm) can be combined to produce the exact resonance frequency of sodium by sum frequency generation ($1/1064 + 1/1319 = 1/589$). This approach has been used by other authors, including Denman et al. [18], who generated a 50 W cw beacon for the SOR observatory, Tracy et al. [19] who produced 12 W of cw mode-locked light for the Gemini North observatory and Jeys et al. [17] who, together with Kibblewhite et al. [20], developed a quasi-cw mode-locked laser which delivers an average power of 8 W in mode-locked pulse bursts lasting 150 μs at a pulse repetition frequency (PRF) of 400 Hz.

Another method of generating the sodium wavelength is to frequency shift a 532 nm laser using an optical parametric amplifier [21]. With this system, 5.5 W was generated in a cw mode-locked pulse train.

In recent times there has been a push to develop cw fibre lasers by Raman shifting and frequency doubling the output of a ytterbium doped fibre [22] [23]. At present these systems have reported powers of up to 3 Watts [22] in a diffraction limited cw beam.

With the introduction of multi conjugate adaptive optics systems (MCAO), currently under development at a number of sites around the world, there will be new and demanding requirements on the laser source being used to produce the reference beacons. This will be discussed in the next section.

1.4 Adaptive optics systems for future large-aperture observatories

1.4.1 Multiple beacons for atmospheric tomography

With the shift to telescopes of larger diameter, such as the extremely large telescopes (ELTs) with diameters > 30 m, the current systems of single beacon adaptive optics will not be acceptable as focus anisoplanatism will greatly restrict the level of atmospheric correction achievable [24]. Any astronomical object that is angularly separated from the reference beacon will receive only partial correction for turbulence because light from it will take a different path through the atmosphere than the beacon. To improve the correction, an approach using multiple beacons has been developed. This technique is known as multi conjugate adaptive optics (MCAO) [11], and is illustrated in Figure 1.6. With this approach, multiple beacons are used to probe the atmosphere and generate a 3D map of turbulence within the whole volume of atmosphere contained in the telescopes field of view. The system uses multiple deformable mirrors, that are optically conjugate to different altitudes, to correct for the turbulence encountered by rays of light from all objects within the telescopes field of view, even if they are angularly separated from a beacon.

Another method of atmospheric correction using multiple guide star beacons is a simplification of MCAO, known as ground layer adaptive optics (GLAO) [25]. With this approach, only one deformable mirror is used, conjugated to the lower atmosphere. This allows correction over the telescopes full field of view, as does MCAO, but the correction is only partial, as most of the turbulence in the upper atmosphere is not compensated.

1.4.2 Gemini guide star requirements for MCAO on ELTs

A MCAO system requires additional performance features from the laser source used to generate the Na beacons. The current generation of guide star laser systems are all fitted on telescopes with diameters ≤ 10 m and use either cw, cw mode-locked or quasi-cw mode-locked beams to generate the beacon. For the next generation of guide star lasers that are required for MCAO on ELTs, it has been acknowledged that a system that delivers short optical pulses would be beneficial to eliminate problems such as spot elongation and cross-talk between beacons (explained later) [24]. This led the Gemini Observatory to issue a call for proposals for vendors to conduct research and development on pulsed laser systems suitable for MCAO [26]. Table 1.1 lists the performance requirements they set. The remainder of this section discusses the physics behind these requirements.

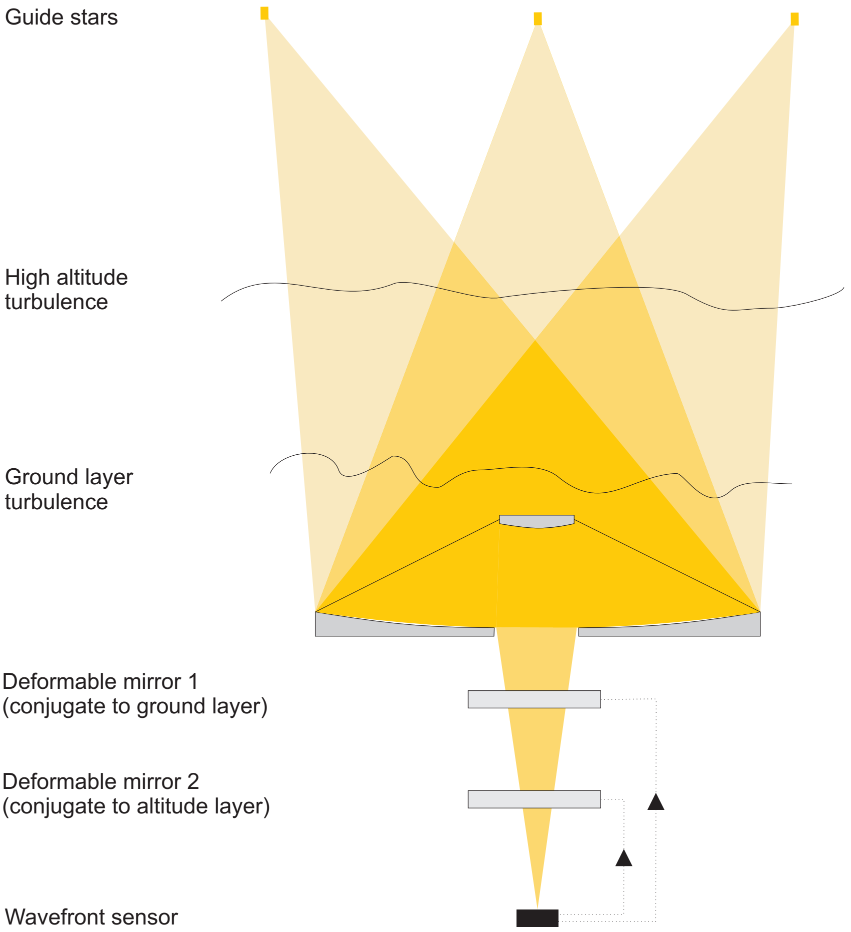

Figure 1.6: A diagram illustrating the concept of multi conjugate adaptive optics. Multiple guide star beacons are used to probe the whole volume of atmosphere in the telescopes field of view. The wavefront sensors detect the turbulence and drive deformable mirrors, which are optically conjugated to different layers of the atmosphere.

Output power	$\geq$ 10 W per beam, 5 beams (50 W total)
Temporal format	Pulsed, PRF variable 600 Hz -800 Hz, pulse length 1-3 μs
Wavelength	Na D2 line
Bandwidth	1-3 GHz
Beam quality	$<$ 1.2 x diffraction limited

Table 1.1: The Gemini performance requirements for a pulsed guide star system for MCAO on ELTs [26]

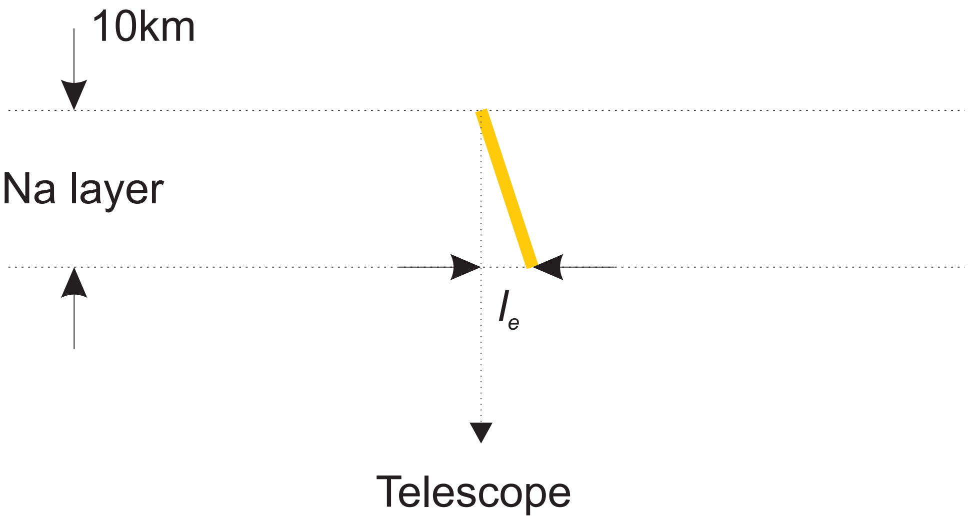

Figure 1.7: When the beacon is viewed from the telescope, an elongated spot of length l_e will be observed due to the thickness of the Na layer.

The elongation effect

The primary advantage of a pulsed laser system is that the problem of spot elongation can be solved. Spot elongation occurs due to the thickness of the Na layer producing a streak of Na fluorescence, which is viewed as an elongated spot by the wavefront sensor [27], see Figure 1.4.2. A pulsed laser can overcome this if the pulse duration is short enough ($<$ 3 μs) that the beacon appears as a point source moving through the sodium layer. As the pulse moves through the atmosphere, it can be followed by, for example, a fast tilting mirror, to image the beacon onto the same spot of a CCD camera, thereby increasing the brightness of the spot and improving the signal to noise ratio of the sensor.

In the presence of elongation, the spot will cover more pixels on the CCD, reducing the signal to noise ratio of the wavefront sensor. More laser power will therefore be required to achieve the same signal to noise ratio. It has been predicted that if spot elongation is present, as it will be for cw or quasi-cw beacons, around three times more laser power is required to achieve the same signal to noise ratio as a beacon that is not elongated. [26]. Hence by using a pulsed laser system that has pulses short enough to defeat spot elongation (< 3 μs) the total average power required from the laser source is only a third as much as for cw systems.

A laser with good beam quality is also advantageous in producing point source beacons, as the beam can be tightly focused in the atmosphere to produce a spot with minimal dimensions and thereby improve the signal to noise ratio of the wavefront sensor.

Rayleigh scatter in the lower atmosphere

Rayleigh scatter in the lower regions of the atmosphere is a potential noise source for wavefront measurements for Na beacons. For cw beacons, the noise from the Rayleigh scatter can be removed by using wavefront sub-apertures to block the majority of the Rayleigh plume and by periodically de-tuning the reference beacons from the sodium wavelength to measure the Rayleigh background, then subsequently subtracting this background from the wavefront measurements [15]. These systems require both power stability and pointing stability of the laser source for the subtraction to be successful [15] as well as a wavelength tuning capability. With a pulsed laser system, the Rayleigh scatter can be simply and robustly gated out (without the need for background subtraction) provided the laser is pulsed at a rate that ensures that there is never more than one pulse in the lower atmosphere and sodium layer at one time. If this is the case, a shutter can be used to cover the wavefront sensor while the pulse is traversing the lower atmosphere, then it can be opened to view the beacon in the sodium layer. For this reason, the laser repetition rate should be 600-800 Hz, enabling range gating at various telescope angles from zenith to 45 degrees.

Sodium bleaching

There is only a limited number of sodium atoms in the atmosphere[2] and to maximise the brightness of the beacon, all of these atoms should be used. The Doppler broadened linewidth of the D2 line of atmospheric sodium is shown in Figure 1.8. It consists of two lines (D2a and D2b) separated by 1.8 GHz. The relative motions of the atoms broaden these lines to a total FWHM of approximately 3 GHz. The spectral width of the laser source should not be greater than this, or laser power will be wasted. Conversely, if the laser linewidth is too narrow, the high energy density of the laser pulses could saturate all the sodium at the laser's frequency and a loss of star brightness will result. If bleaching is not found to be a problem a laser bandwidth of approximately 1 GHz may be beneficial, as this spectrum can be matched to the higher cross-section D2a line giving better photon returns. Alternatively, if bleaching is found to be significant, it may be better to use a broad spectrum pulse (3 GHz) and cover the whole of the sodium linewidth. A laser system that has an adjustable spectral width in the range of 1-3 GHz would have an advantage as it could be optimised experimentally to maximise the brightness of the beacon.

---

[2] The mesospheric sodium is thought to originate from meteorites that disintegrate in the upper atmosphere [28]

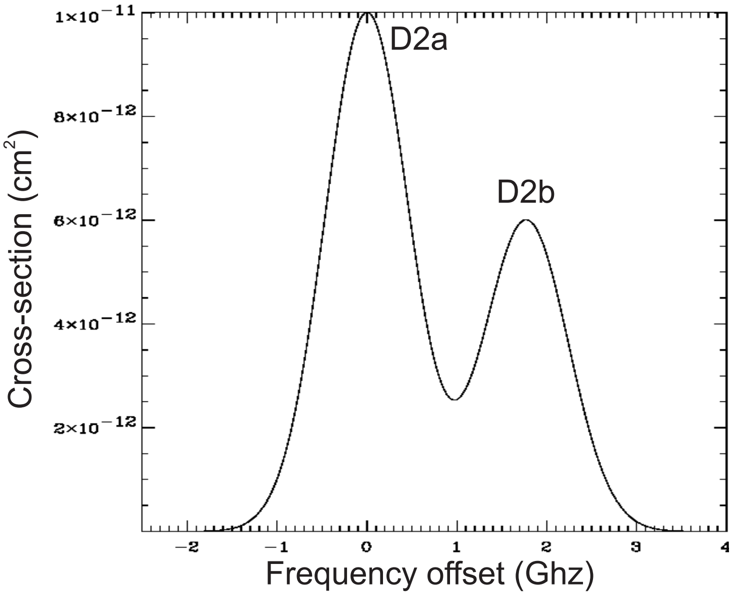

Figure 1.8: The Doppler broadened D2 absorption cross section of atmospheric sodium [29]

Another factor that will effect sodium bleaching is the pulse duration. It was stated in Section 1.4.2 that the pulse duration should be kept less that 3 μs to defeat spot elongation, but the pulse should not be made too short or the high energy density of the short pulse could cause bleaching and reduce the brightness of the beacon to unacceptable levels. Hence pulse widths of 1 - 3 μs was stated as an appropriate range in Table 1.1.

While a narrow band Na laser system making use of optical pumping [30] can produce a very bright Na resonance output, this will only work for cw or quasi-cw systems, and not for short 1 - 3 μs macro-pulses. If the bandwidth of the 1 - 3 μs pulse source is broad enough, however, such that the spectrum will overlap regions of both the D2a and D2b lines of sodium, all mesospheric sodium will be able to participate in resonance for a 1 - 3 μs macro-pulse laser system, without optical pumping.

1.5 This thesis

In this thesis, a new laser design is described and verified, which produces a pulse burst waveform that can meet all the Gemini performance requirements of Table 1.1. The design concept was first proposed by Munch and Veitch in 2004 [31] then developed and verified by the author [32] [33].

The laser produces a pulse burst waveform that consists of a series of short micro-pulses modulated by a macro-pulse envelope as shown in Figure 1.9. By using short micro-pulses, the bandwidth of the laser can be controlled, as the pulse width and bandwidth are Fourier

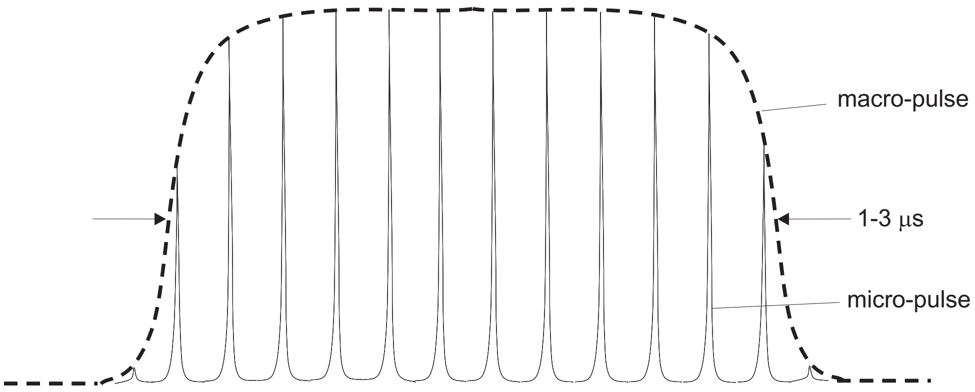

Figure 1.9: An ideal macro-micro pulse format, optimised for MCAO systems: The micro-pulse width is set to control the laser's bandwidth; the macro-pulse duration is optimised to reduce spot elongation and sodium bleaching; the macro-pulse repetition rate is 600-800 Hz to enable gating of Rayleigh scatter.

transform pairs. An additional feature is that the separation of micro-pulses can be made close to the fluorescence lifetime of sodium (16 ns) to allow sodium atoms to relax between micro-pulses and participate in more fluorescence.

Details of the laser system design are presented in Chapter 2. Chapter 3 presents experimental results from a proof of principle laser and shows the successful generation of macro-micro pulse bursts with both wavelength and bandwidth control. Chapter 4 presents a novel method for stretching the duration of Q-switched laser pulses and the technique is used to lengthen the macro-pulse duration to 1-3 μs as required. Finally, Chapters 5, 6 and 7 present the design and construction of a 800 Hz laser source with the average power, pulse format and beam quality required from the final system design.

Chapter 2

Injection mode-locked guide star laser design

2.1 Introduction

The design of the laser system for next generation adaptive optics systems presents an interesting challenge for laser physics. The combined requirements of laser pulse format, power, beam quality, wavelength and bandwidth, listed in Table 1.1, are difficult to fulfil given that there is no reliable high power laser source that can emit directly at the sodium wavelength. Previous authors have demonstrated various approaches for generating the 589 nm light including sum frequency generation (SFG) of Nd:YAG [17] [19] [20] and fibre systems [23], dye lasers [34], second harmonic generation (SHG) of fibre raman lasers [22] [35] [36] and optical parametric oscillators [21]. These systems have been successful in meeting some of the requirements of Table 1.1, but there is still, at present, no complete guide star system available that can simultaneously meet all the requirements.

The aim of this chapter is to present a system design for advanced guide star laser systems, capable of meeting the complete set of performance requirements set down by the Gemini observatory [26] (Table 1.1). The chapter begins with an overview of the design in Section 2.2, injection mode-locking is described in Section 2.3, then each component of the system design is described in detail during later sections.

2.2 Guide star system design overview

The outline of the guide star laser system design is represented by the block diagram of Figure 2.1. It uses SFG of two mode-locked Nd:YAG lasers to achieve the sodium wavelength similar to previous designs [17] [19] [20], but with the novel application of injection

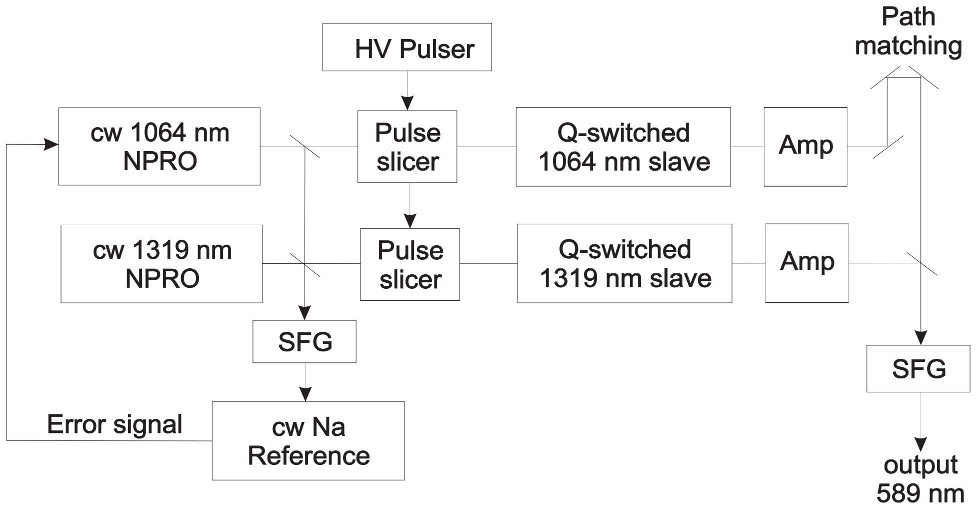

Figure 2.1: Overall design concept. Two cw NPRO lasers provide the absolute wavelength control and tuning, and synchronized pulse slicers provide timing and bandwidth control of injection mode-locked slave lasers for subsequent SFG at the Na wavelength.

mode-locking as a robust method to control the wavelength, bandwidth, peak power and timing for SFG. An additional feature is the use of stretched Q-switching as an efficient method of producing the 1-3 μs pulses required to overcome spot elongation and avoid bleaching of the Sodium. The combination of these two features enable the production of a burst of high-peak-power micro-pulses optimized for efficient SFG, contained within a longer macro-pulse, that has a duration that can be controlled by the Q-switching. The power scalability of this design is assured by the use of Nd:YAG as the gain medium, together with a master oscillator power amplifier (MOPA) configuration. This approach has already been proven in previous studies to deliver output powers in excess of 50 W with diffraction limited beam quality [37] [38].

A highlight of the design is that it uses cw, non planar ring oscillator (NPRO) lasers for the master sources to guarantee the wavelength. These lasers each produce a stable, single-frequency output that can be tuned to produce the exact wavelengths near 1064.59 nm and 1319.25 nm required to achieve sodium resonance by SFG [17]. A robust frequency lock can then be obtained by using the master lasers and a secondary, low power SFG system to illuminate a sodium cell and generate an absolute frequency reference to the sodium line. A simple feedback circuit can then be used to keep the lasers locked to the sodium line [39] [33].

For injection mode-locking, a seed pulse of about 1 ns duration is sliced from the NPRO beam and injected into the slave resonator [40]. In our case, the wavelength of the slave laser is thereby set by the frequency locked master source and the bandwidth is controlled by adjusting the width of the seed pulse (a seed pulse width of 1 ns will have a Fourier transform bandwidth of around 1 GHz for example). The seed pulse can be produced using a Pockels cell placed between crossed polarisers, driven by a fast, high voltage pulser. To eliminate timing jitter between 1064 nm and 1319 nm micro-pulses for efficient SFG, the two pulse slicers are driven in series by the one high voltage pulser to ensure perfect synchronization of the micro-pulses, without the need for complicated servo electronics.

Given the high-peak-powers expected from the short duration macro and micro-pulses, a simple single or double pass SFG stage can be used to generate the high power sodium light. This offers a significant reduction in complexity when compared to cw systems, which require two lasers to be locked to a resonant SFG cavity to increase the power circulation through the SFG crystal [41].

2.3 Injection mode-locking

2.3.1 Objective

The aim of this section is to explain the theory of injection mode-locking and to show how injection mode-locking can be used to control the bandwidth, wavelength and timing of the output pulses of a laser, as required for advanced SFG guide star sources. The section gives a general description of mode-locking in Section 2.3.2 then presents details specific to injection mode-locking in Section 2.3.3.

2.3.2 Mode-locking of laser resonators

The total electric field, $E(t)$, inside a laser resonator consists of the superposition of the electric fields, E_n, from each frequency component or longitudinal mode, n, that is able to resonate inside the cavity. The total electric field, $E(t)$, can thus be written as [42]

$$E(t) = \sum_n E_n e^{i[(\omega_0 + n\Delta\omega)t + \phi_n]} \tag{2.1}$$

where ω_0 is the angular frequency of the mode at the centre of the laser's spectrum, $\Delta\omega = \frac{\pi c}{2L}$ (L is the cavity length) is the frequency difference between modes and ϕ_n is the phase.

If the phase difference between modes, $\Delta\phi_n$, is non-zero at all points inside the laser cavity, the electric field amplitude has a random nature and the laser output fluctuates with time as depicted in Figure 2.2(a). If there is no time varying phase shift between

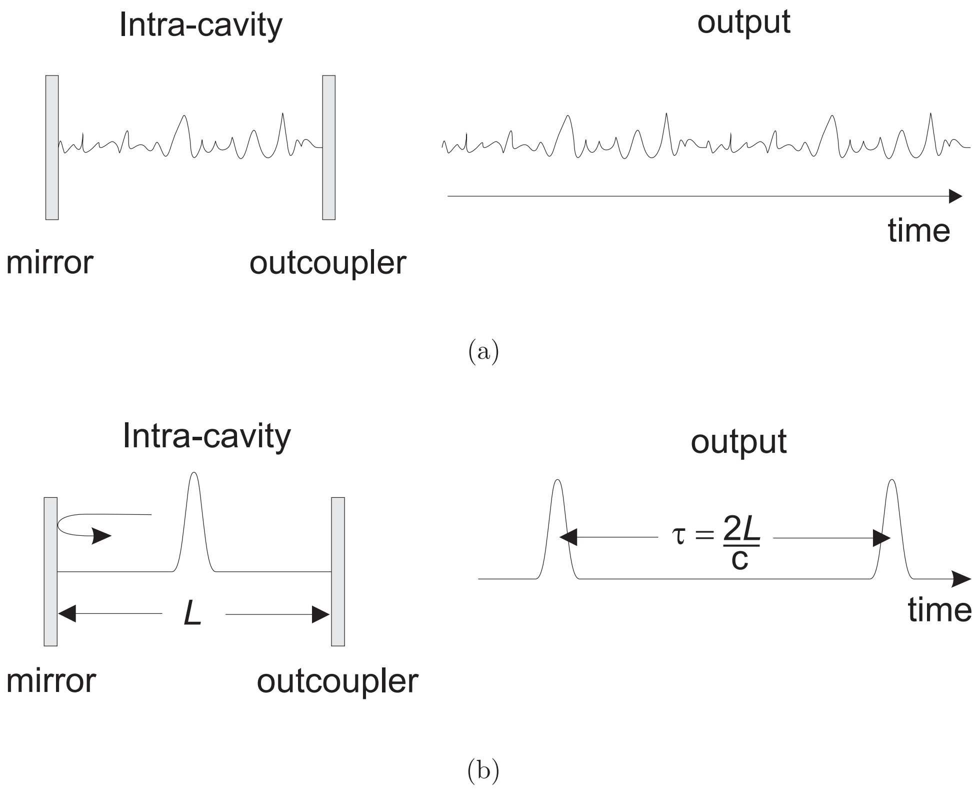

Figure 2.2: The superposition of longitudinal modes inside a laser cavity can result in a) an irregular output if there is no fixed phase relationship between modes, or, b) a well defined pulse if there is a fixed phase relationship (ie. the laser is mode-locked). In the mode-locked case (part b), the output consists of a train of pulses separated by the round trip time of the resonator.

modes (ie. $\Delta\phi_n = 0$ at some point inside the cavity), the laser is said to be mode-locked and the electric field can be written as

$$E(t) = \sum_{-\frac{N-1}{2}}^{\frac{N-1}{2}} E_n e^{i(\omega_0 + n\Delta\omega)t} \tag{2.2}$$

$$= e^{i\omega_0 t}\frac{\sin(N\Delta\omega t/2)}{\sin(\Delta\omega t/2)} \tag{2.3}$$

Where N is the total number of modes. The laser power $P(t) \sim E^*(t)E(t)$ is thus proportional to

$$\frac{\sin^2(N\Delta\omega t/2)}{\sin^2(\Delta\omega t/2)} \tag{2.4}$$

resulting in a pulsed output from the laser as sketched in Figure 2.2(b). In this case, the superposition of longitudinal modes in the cavity has resulted in constructive interference to produce the short, high-peak-power intra-cavity pulse and has produced destructive interference in the low light level regions between pulses.

In practice, a laser can be mode-locked in a number of ways including both passive and active techniques. For passive mode-locking, a nonlinear element such as a saturable absorber or a Kerr lens is inserted into the optical cavity. Saturable absorbers are opaque at low power levels but become highly transparent at high optical powers and thus favour the generation of a short duration high-peak-power optical pulse in the laser cavity and thereby mode-lock the laser resonator. Kerr lenses have an intensity-dependent focal power and can be used to alter the stability and loss of the resonator so that only a high-peak-power intra-cavity pulse will run stably.

Lasers can be actively mode-locked using an intra-cavity AM or FM modulator, which also favour the production of short duration pulses inside the resonator and by injection-mode-locking, which is the topic of the following section.

2.3.3 Injection mode-locking

The technique of injection mode-locking was first demonstrated by Alcock et al. in 1977 using CO_2 lasers [40]. The technique is different from other methods of mode-locking in that no intra-cavity element is required to mode-lock the laser. Rather, a short duration seed pulse is injected into the resonator, and the frequencies in this pulse that match the longitudinal modes of the resonator will be amplified and grow with a fixed phase relationship to each other, mode-locking the slave resonator. Thus, in contrast to other methods where the losses are increased for all but the mode-locked pulse, in this case the gain for the preferred modes is increased.

To explain the process more clearly, Figures 2.3, 2.4 and 2.5 have been included sketching the temporal and frequency structure of the seed pulse and the mode-locked slave resonator. Figure 2.3 shows the seed pulse prior to injection into the slave resonator. For the guide star laser, this seed pulse is sliced from a cw single frequency NPRO beam using a Pockels cell as mentioned in Section 2.2 and discussed in detail in Section 3.4. If the temporal shape of the pulse is Gaussian then the spectral content of the pulse in frequency space is also Gaussian according to the Fourier transform relationship

$$e^{-\alpha t^2} \Leftrightarrow \sqrt{\frac{\pi}{\alpha}} e^{-\frac{(\pi\nu)^2}{\alpha}} \tag{2.5}$$

for which the constant, α, is related to the FWHM pulse duration, Δt, by

$$\Delta t = \sqrt{4/\alpha \ln(2)} \tag{2.6}$$

When the seed pulse is injected into the slave laser resonator, the only frequency components of it that can resonate are those which match the longitudinal modes of

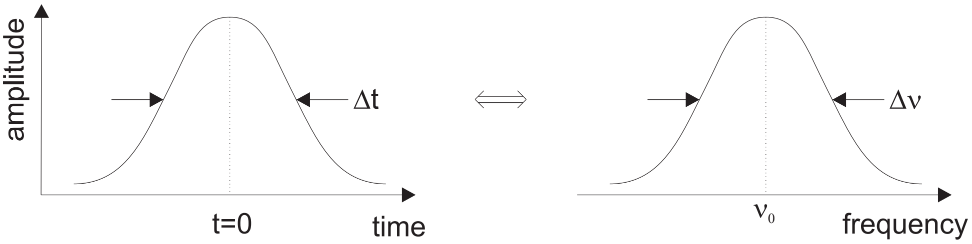

Figure 2.3: The temporal and spectral characteristics of a Gaussian-shaped seed pulse. The double arrow represents a Fourier transform.

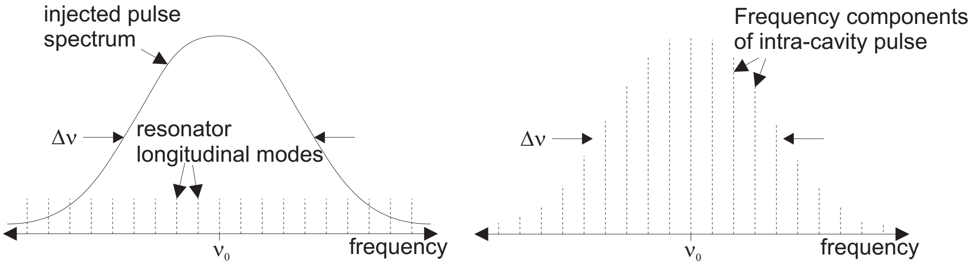

Figure 2.4: A diagram illustrating the changes in frequency spectrum which an optical pulse undergoes when it is trapped inside a Fabry-Perot laser cavity. The LHS shows the pulse spectrum before being injected into the cavity and also the allowed frequencies of the slave longitudinal modes (spaced by $\Delta\nu_m = \frac{c}{2L}$ where L is the cavity length). The RHS shows the resulting spectrum of the pulse when trapped inside the cavity. The only frequency components that can resonate are those which match the longitudinal modes. These frequencies will then be amplified by the gain medium inside the laser cavity.

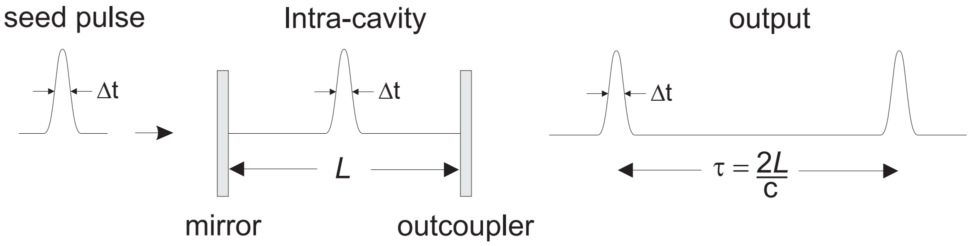

Figure 2.5: For injection mode-locking, a seed pulse is injected into a laser cavity then amplified over repeated round trips by the gain medium (not shown). For each round trip inside the cavity, part of the pulse is outcoupled producing a mode-locked waveform with a PRF of $\frac{c}{2L}$ as shown.

the cavity, ie those which have an integer number of wavelengths per round trip. Hence by trapping the seed pulse within the laser cavity, the frequency content of the pulse will change as illustrated in Figure 2.4. If the seed pulse has greater energy than the spontaneous emission of the laser, the seed pulse will be preferentially amplified and dominate the output of the laser. Murray and Lowdermilk [43] found that a seed pulse energy of as little as 1 fJ was required to overcome the spontaneous emission for their Nd:YAG laser system.

Since the seed pulse is sliced from a cw single frequency beam, all frequency components of the seed pulse will be in phase and when the seed is injected into the slave, the longitudinal modes will be excited in phase and the slave will be mode-locked. The laser will therefore produce the characteristic pulse burst of a mode-locked laser, shown in Figure 2.5. When used in conjunction with Q-switching, the short duration micro-pulses will be modulated by a macro-pulse set by the Q-switch, producing the ideal macro-micro pulse waveform as depicted in Figure 1.9.

A variant of the injection mode-locked lasers are the so-called cavity-dumped lasers [43] (not relevant to the current application). These lasers are different from injection mode-locked lasers in that they do not have an outcoupling mirror to produce a micro-pulse burst. Rather, these lasers employ an intra-cavity pockels cell to eject the entire intra-cavity pulse once it has been fully amplified, producing a single, short duration high energy pulse as the laser's output.

Bandwidth control

The spectral bandwidth of the seed pulse is inversely proportional to the pulse duration as shown, for example, by Equation 2.5. Hence by changing the pulse duration the bandwidth of the pulse can be controlled. This allows the spectrum of the injection mode-locked laser to be matched to the Doppler broadened linewidth of atmospheric sodium (Figure 1.8) to maximise the brightness of the guide star. The ideal bandwidth of the laser will be in the range of 1-3 GHz (Section 1.4.2) which will require a micro-pulse duration of approximately 0.3-1 ns (assuming a unity time-bandwidth product). A variable-duration seed pulse source that can produce pulses in this range is described in Section 3.4.

For the laser to be optimally injection mode-locked, multiple longitudinal modes need to contribute to the laser's spectrum. If too few modes are present, the laser's spectrum will not cover a broad frequency range but will contain only a few frequency spikes corresponding to the longitudinal modes. As a result, the brightness of the guide star will be diminished, as not all sodium atoms will be in resonance with the laser. Moreover, the laser will no longer produce a well defined pulse burst containing high-peak-power micro-pulses and low light levels between pulses, resulting in reduced SFG efficiency. To avoid these problems, the cavity length needs to be made significantly longer than the seed pulse duration to reduce the frequency spacing between modes ($\Delta\nu_m = \frac{c}{2L}$) and ensure that the seed spectral width ($\Delta\nu \approx \frac{1}{\Delta t}$) will overlap multiple longitudinal modes.

Wavelength control

An essential aspect of any laser guide star system design is the ability to tune the output accurately to the sodium absorption line. Wavelength tuning in injection mode-locked lasers can be simply and reliably achieved by tuning the wavelength of the master laser used to generate the seed pulse. For our case, the seed pulse is generated by gating the output of a cw NPRO laser using a Pockels cell (Section 3.4) so the centre frequency of the seed pulse (and hence the slave laser) will be set by the frequency of the cw NPRO laser[1]. This last statement can be proven using the convolution theorem: The seed pulse can be thought of as the multiplication of the amplitude of the cw NPRO beam, $a(t)$, with a transmission function, $f(t)$, representing the shape of the seed pulse, as shown in the left hand side of Figure 2.6. By the convolution theorem, the spectrum of the seed pulse is therefore given by the convolution of the Fourier transform of the cw beam, $A(\nu)$, and the Fourier transform of the transmission function, $F(\nu)$ (see the right hand side of Figure 2.6).

The centre frequency of the seed pulse (and hence the slave laser) will therefore be centred at the frequency of the cw master beam used to generate the seed pulse, given that the seed pulse spectrum is the convolution of a kronecker delta centred at the master frequency, ν_0, convolved with a Gaussian.

Section 2.8 presents experimental measurements showing that the SFG of 1064 nm and 1319 nm NPRO lasers can be accurately and reliably tuned to the sodium wavelength.

Timing jitter

The timing of the micro-pulses from an injection mode-locked laser is set by the timing of the injected seed pulse plus a delay equal to the number of round trips the pulse makes before being outcoupled from the laser cavity. Furthermore, the timing jitter of the output micro-pulses is equal to the timing jitter in the seed pulse, provided there is no intra-cavity element that introduces additional sources of jitter. For the SFG macro-micro pulsed guide star, low timing jitter is essential for efficient frequency conversion as short duration micro-pulses from the 1064 and 1319 nm slave lasers need to be closely

---

[1] The effects of frequency chirping will be negligible compared to the bandwidth of the injected seed pulse

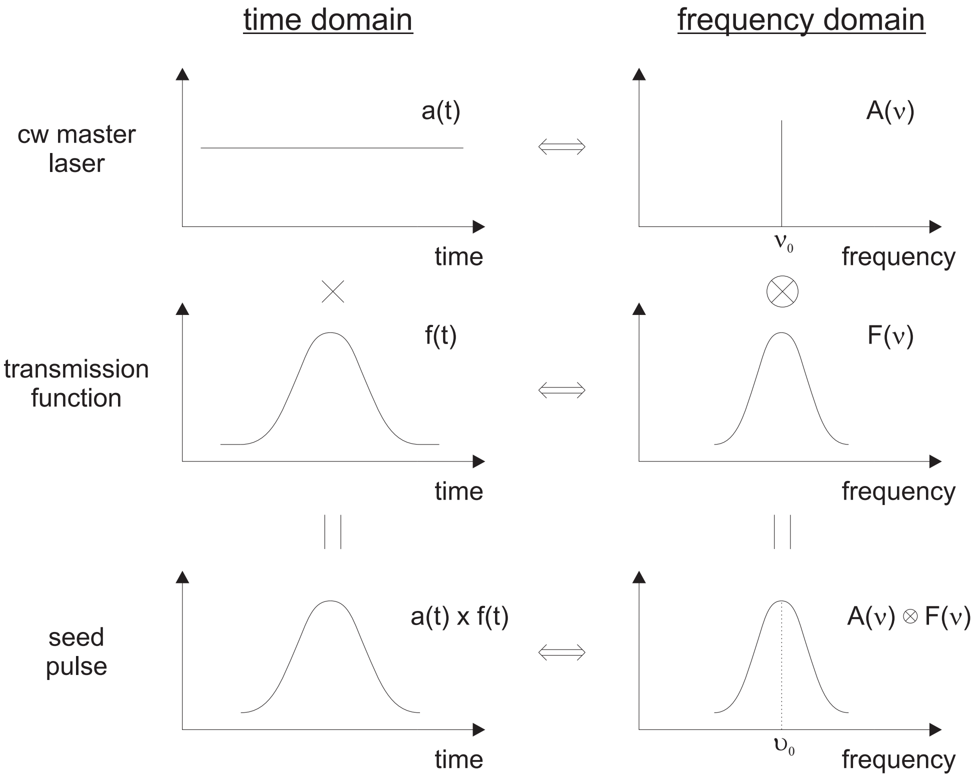

Figure 2.6: A graphical representation of the temporal and spectral content of the seed pulse. The LHS shows the time domain and the seed pulse created by the multiplication of the master laser amplitude $a(t)$ with a Gaussian transmission function used to generate the pulse, $f(t)$. The RHS shows the Fourier transform of the LHS. The double arrows represent Fourier transform pairs and the cross within the circle represents a convolution.

overlapped within the SFG crystal. If the seed pulse source can be made to have low timing jitter, as is later proven in Section 3.4, the process of injection mode-locking can be used to control the laser timing jitter, thus meeting an important system requirement.

2.3.4 Conclusion

This section presented details on the theory of injection mode-locking and showed that an injection mode-locked laser can in theory be used to generate a burst of high-peak-power micro-pulses having the combination of bandwidth control, wavelength control and low timing jitter as required for advanced SFG guide star sources. In the following chapter and in later parts of this thesis, the concept of injection mode-locking is demonstrated with Nd:YAG lasers and is proven to be successful in meeting the spectral and timing requirements of the guide star source.

2.4 Slave resonator design

2.4.1 Introduction

The specific requirements of the macro-micro pulse burst waveform place certain restrictions on the slave resonator design. Firstly, there must be some way of injecting the seed pulse for injection mode-locking. Secondly, the resonator must have a long length to reduce its free spectral range and ensure that the spectral width of the injected seed pulse will excite many longitudinal modes for effective injection mode-locking (Section 2.3). Thirdly, there must some means of stretching the Q-switched macro-pulse to avoid bleaching in the sodium layer. Finally, the resonator must be suitable for high peak and average intra-cavity laser powers. It must therefore be efficient, stable and insensitive to changes in the focusing power of the induced thermal lens. This section presents a description of a novel ring resonator design that can facilitate all of these properties [44].

2.4.2 Travelling wave ring resonator design

A travelling wave ring resonator design was selected as the architecture of choice for the injection mode-locked slave oscillator. A schematic of the ring design is shown in Figure 2.7. For comparison, a standing wave design that could also be used for injection mode-locking is described in Figure 2.8. The ring design offers several advantages over standing wave designs, primarily relating to Q-switched pulse stretching, which will be discussed later in this section. Other benefits include the fact that less optical isolation

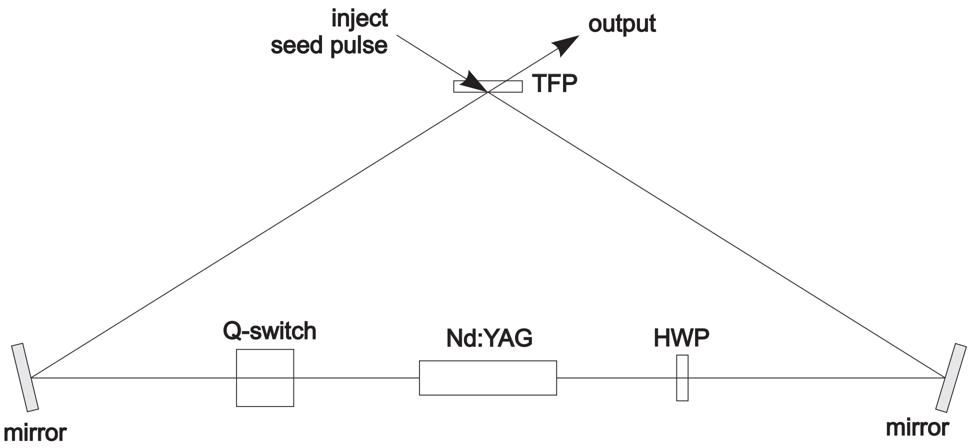

Figure 2.7: Slave laser configuration, showing pulse injection into a travelling ring oscillator via a polarizing beam splitter (TFP), and the arrangement of polarizing elements and Q-switch required to stretch the macro-pulse formed.

is required between the master and slave oscillators. For standing wave designs, the master and slave beams counter-propagate on the same axis, so high contrast isolators are required to prevent de-stabilization of the master oscillator by feedback from the slave. This often requires multiple isolators, with each introducing a loss of around 10 % [45], attenuating the input and output beams. Another advantage is that the ring architecture does not require an intra-cavity polariser to be used in transmission, further reducing the round trip loss by around 2 %[2].

For injection mode-locking, a π-polarized seed pulse is injected into the ring through the thin film polarizer (TFP). Its polarization is converted to σ by the half wave plate (HWP) before it passes through the gain medium and Q-switch. There is initially no voltage on the Q-switch, so the pulse will pass through without change in polarization and be fully reflected by the TFP. The half wave voltage is then applied to the Q-switch which traps the pulse within the resonator on second and subsequent round trips allowing a rapid amplification in pulse energy with low loss. Once the pulse has built up sufficiently, the voltage on the Q-switch is reduced slightly and the π-polarized component is outcoupled through the TFP. A key feature of this resonator is that the outcoupling fraction can be rapidly varied by controlling the voltage level applied to the Q-switch. If there is a low voltage, there will be a high outcoupling and if the voltage is near half-wave the outcoupling fraction will be small. If an appropriate Q-switch voltage waveform is chosen, consisting of a voltage pulse with appropriate amplitude modulation, the outcoupling fraction can be used to slow the development of the giant pulse and stretch its duration.

---

[2] Three 1064 nm TFP's were obtained from CVI Laser and were measured to have near 100 % reflectance for σ-polaraized light and 98 % transmission of π

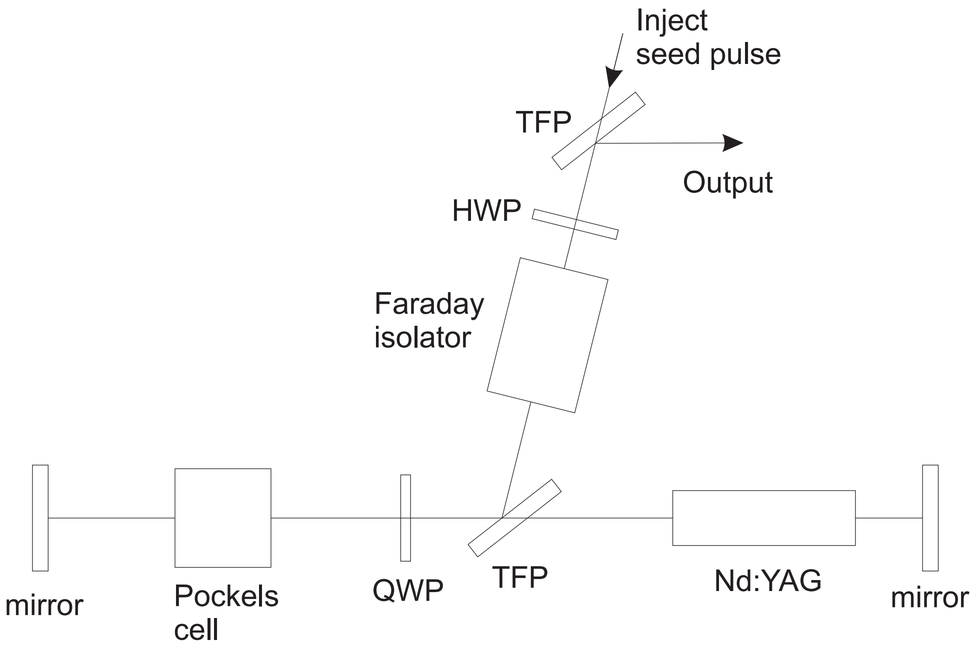

Figure 2.8: Example of a standing wave resonator that could be injection mode-locked. The output pulse is separated from the input seed pulse using high contrast isolators.

More details on this technique are presented in Chapter 4 and in the publication found in Appendix A. Unlike other pulse stretching schemes that introduce an intra-cavity loss to slow the development of the giant pulse [46] [47] [48], this resonator offers a unique advantage in that all losses are useful as the laser output, allowing much greater efficiency (see Chapter 4).

Another inherent advantage of ring resonators in this application is that the pulse makes only one traversal of the gain medium per round trip (as opposed to two for the standing wave design) thereby halving the round trip gain and increasing the giant pulse duration [49].

2.4.3 Conclusion

This section described a novel ring resonator design that facilitates both injection mode-locking and pulse stretching to produce the preferred macro-micro pulse burst waveform. The design contains few intra-cavity elements, enabling efficient operation, and the novel pulse stretching technique uses all modulated losses as the laser output, so as not to reduce the efficiency [50]. This resonator plays an integral role in the guide star laser system design and has been proven to be very successful in achieving the laser requirements, as detailed in later chapters of this thesis.

2.5 High power sum frequency generation

2.5.1 Introduction

High power SFG is required at the output of the guide star system to convert the two fundamental wavelengths of 1064 nm and 1319 nm to the sodium wavelength (589 nm). SFG of Nd:YAG lasers at these wavelengths was first reported by Jeys et al. [17]. High power SFG systems have been reported by Denman et al. [18] and Tracy et al. [19] who produced 50 W and 16 W of sodium light respectively. Denman et al. used two cw lasers: 100 W at 1064 nm and 60 W at 1319 nm, together with a lithium tri-borate (LBO) crystal to generate the sodium light. Due to the low peak power of the cw lasers, the two lasers were phase-locked to an external resonant cavity containing the LBO crystal using the Pound-Drever-Hall stabilization technique [18]. In Tracy et al., the SFG was accomplished using periodically-poled nearly stoichiometric lithium tantalate (PPnSLT), pumped by cw mode-locked lasers, which resulted in a maximum conversion efficiency of 40 % from a single pass through the PPnSLT crystal.

The injection mode-locked laser system proposed in Section 2.2 has a different pulse format to any other guide star system and the the short duration micro-pulses are expected to produce peak powers several orders of magnitude high than these cw and cw mode-locked systems. Thus it was necessary to develop a preliminary concept design of the SFG system best suited to this work and to estimate the expected conversion efficiency so as to determine the laser powers at 1064 nm and 1319 nm required to produce 50 W at the sodium wavelength. This section presents a summary of this investigation.

Section 2.5.2 gives a brief review of nonlinear optics and SFG. It is not intended to be a comprehensive description of the field as this information is available in textbooks [51] but it is hoped that this section is sufficient to provide an introduction to the topic and discuss the issues that are important when designing an efficient SFG system for this laser. Section 2.5.3 presents an evaluation of commonly available nonlinear crystals that may be useful for 589 nm SFG systems, then in Section 2.5.4 a calculation of the conversion efficiency for a likely candidate, LBO, is presented.

This thesis does not present experimental validation of the SFG system proposed in this section as the equipment and 1319 nm lasers were not available at the time of this work, but the results from this section are useful to validate the guide star system design and to provide an estimate of the power levels required at the fundament wavelengths, based on the estimated SFG conversion efficiency.

2.5.2 Theory of SFG

Optical processes are termed “nonlinear” when the response of a material to an applied optical field depends in a nonlinear manner upon the strength of the optical field. In conventional “linear” optics the material polarization, $P(t)$, varies linearly with the electric field:

$$P(t) = \chi^{(1)} E(t) \tag{2.7}$$

where the constant of proportionality, $\chi^{(1)}$, is termed the linear susceptibility and is a 2nd rank tensor. In non-linear optics, the polarization is expanded in the form

$$P(t) = \chi^{(1)} E(t) + \chi^{(2)} E(t)^2 + \chi^{(3)} E(t)^3 + \ldots \tag{2.8}$$

where $\chi^{(2)}$ is the second order susceptibility and is the parameter that relates to phenomena such as SHG and SFG.

If the polarization is time varying, as is the case when the applied electric field is a laser beam, charges are being accelerated, which implies that new EM radiation is generated. If the frequency and direction of the laser beam are tuned correctly, new frequencies can be created with, for example, twice the incident frequency (SHG). If two pump beams are used to excite the material then light with the sum of the frequencies can be emitted (SFG).

Some of the major factors that influence the conversion efficiency are:

Laser peak power The efficiency of SFG depends on the square of the electric field strength of the incident optical field.

Effective nonlinear coefficient The effective nonlinear coefficient, d_{eff}, is a parameter derived from the tensor $\chi^{(2)}$. A high value of d_{eff} generally implies efficient conversion, provided other material parameters are suitable. The value of d_{eff} depends on the type of nonlinear material and the polarization and angle of the incident fields.

Phase matching For a nonlinear birefringent crystal, it is possible to select a laser propagation angle that will result in a fixed phase relationship being maintained between the converted frequency and the nonlinear polarization, $P(t)$ [51]. This condition is known as the phase matched state and can result in dramatic improvements in extraction as it allows in-phase conversion along the whole crystal length instead of a periodic oscillation between conversion and back conversion due to the phase mismatch between fundamental and SFG beams.

Walk-off angle Walk-off occurs when the generated beam separates from the incident beam due to double re-fraction. If the walk-off angle is large, the efficiency will be significantly reduced as the pump and generated waves will no longer overlap. Walk-off occurs only when the incident field is at an angle to the optic axis of the crystal, as is sometimes required to ensure phase matching.

Damage threshold To achieve high-peak-power for efficient conversion, the incident beam should be focused to a small spot inside the crystal. The limitation on how small this spot can be made is determined by the damage thereshold of the material.

An estimation of the conversion efficiency, η, for SFG can be obtained from the solution to Maxwell's equations in a nonlinear dielectric medium. The solution can be obtained by reducing Maxwell's equations to a pair of coupled wave or amplitude equations for parametetric interactions that require that the gain in intensity at the summed wavelength (I_3) be counterbalanced by a reduction in power at the fundamental wavelengths (I_1 and I_2) [52] [53]. The stepwise integration of these coupled wave equations can then yield approximations to the conversion efficiency [54]. For the case in which plane waves with top-hat profiles are assumed and cw beams, zero walk-off and perfect phase matching are used, an analytical solution to the conversion efficiency can be written as [54]

$$\eta \approx \tanh^2(\sqrt{\eta_0}) \frac{\sin^2[L\,\delta\,kexp(\eta_0^{0.87}/6.7)/2]}{[L\,\delta\,kexp(\eta_0^{0.87}/6.7)/2]^2} \tag{2.9}$$

where

$$\eta_0 = C^2 \left(1 + \frac{\lambda_1}{\lambda_2}\right)^2 L^2 \frac{I_1 I_2}{I_1 + I_2} \tag{2.10}$$

and

$$C = 5.454(n_1 n_2 n_3)^{-1/2} d_{eff} \lambda_1 \tag{2.11}$$

for which the intensities I_i are given in GW/cm^2, wavelengths λ_i in μm, phase mismatch δk in cm^{-1} and d_{eff} is in pm/V.

For a more realistic treatment that includes Gaussian beam profiles, temporal variation in peak power for pulsed lasers and walk-off a computer program can be used which calculates the conversion efficiency of fields with time-varying amplitudes at a lattice of points within the crystal volume. This is the approach taken in Section 2.5.4, which presents example calculations of SFG conversion efficiency for macro-micro pulsed lasers.

2.5.3 Evaluation of common SFG materials

This section presents a discussion of which commonly available nonlinear crystals are suitable for use in the injection mode-locked guide star laser source. The desire is to realize a simple and efficient single-pass SFG stage to convert the infra-red power at the fundamental wavelengths (1064 nm and 1319 nm) into a sodium-wavelength beam (589 nm).

	KTP	PPLN	LBO	BBO
d_{eff} (pm/V)	3.3	4.8	0.84	2.0
Phase matching angle (°)	62.5	0	3.4	21.4
Walk-off angle (mrad)	43.2	0	2.1	52.7
Damage threshold (GW/cm^2)	0.5	0.1	2.5	1.5
Accept. angle (mrad-cm)	25	47	35	1.3
Max average power (W)	15	10	>100	>100

Table 2.1: Nonlinear material parameters for commonly available nonlinear crystals that may be suitable for use in the injection mode-locked guide star system [55] [51]. The values listed are for SFG of 1064 nm + 1319 nm lasers at 300°K. The acceptance angle is defined as the range for which the phase mismatch varies between $-\pi$ and $+\pi$.

To achieve high conversion efficiencies, the nonlinear material must be transparent at the wavelengths of 1064, 1319 and 589 nm, be of high optical quality and be able to handle high average powers and the consequent thermal gradients without spoiling the phase matching and beam quality. Table 2.1 presents a list of commonly available nonlinear materials that may be suitable. Other nonlinear materials such as KD*P have been excluded from this table due to their failure to meet one or more of the aforementioned requirements, making them unsuitable for use in the injection mode-locked guide star source. KD*P, for example, suffers substantial absorption at 1319 nm and hence has been excluded.

To produce 50 W of 589 nm average power, the required average power of the fundamental wavelengths will be of the order of 100 W, assuming a conversion efficiency of 50 % can be obtained. For this application LBO and BBO are the prime candidates as they have been proven to withstand average powers in excess of 100 W without degradation in efficiency or beam quality [18] [56] [57].

Another option is to split the main beam into a number of sub-beams and perform the SFG in several parallel stages. This technique may be acceptable as the guide star source must be split to produce multiple beacons anyway. For this approach, greater efficiency may be obtained with PPLN or the newly developed PPnSLT [19]. A single SFG stage does have advantages however, as it reduces the complexity and price of the system. Hence LBO and BBO are the preferred materials for the guide star system.

LBO has the advantage over BBO that it has a larger angular acceptance angle meaning a tighter focus can be used within the crystal to increase peak power. The birefringence in LBO can also be temperature tuned to provide zero walk-off at 39℃, which provides further benefits to efficiency as smaller spotsizes can be used within the crystal without decreasing the beam overlap region due to walk-off. So, despite BBO having a larger effective nonlinear coefficient, LBO should produce higher conversion efficiencies when used in the injection mode-locked guide star laser system. This choice is supported by other authors of high average power Na SFG laser systems who have also reported LBO as their preferred material [18] [41].

2.5.4 Estimation of SFG conversion efficiency for LBO

Objective

The aim of this section is to provide an estimation of the conversion efficiency expected for SFG of injection mode-locked macro-micro pulse waveforms in LBO. This value is important as it indicates the power levels at 1064 nm and 1319 nm required to produce 50 W at the sodium wavelength.

Approach

The computer program SNLO [55] was used to estimate the conversion efficiency of the SFG system. This program is freely available online and has become the industry standard for nonlinear optics calculations [58] [59]. It is able to compute the conversion efficiency at a lattice of points across the beam profiles and along the nonlinear crystal's length and then integrate the net conversion efficiency over time as a laser pulse passes through the crystal. This allows the program to take account of factors such as Gaussian beam profiles and the time varying peak power of micro-pulses for improved accuracy [58].

One of the required inputs to the program is the spot size of the fundamental beams within the LBO crystal. A small spot size is desirable as it gives increased peak power for greater efficiency, but the spot should not be so small that it causes damage. The damage threshold of LBO is quoted as 25 J/cm^2, 10ns pulse [55], which is higher than most anti-reflection (AR) coatings which have a damage threshold of up to 10 J/cm^2, 20 ns pulse [60]. To lower reflection losses it is preferable to have the LBO crystal AR-coated[3], so the damage threshold of the coating will be the limiting factor when considering the optimum focus for SFG.

The laser parameters used in the model were 1 ns micro-pulses separated by 12 ns and a macro-pulse width of 2 μs with 800 Hz PRF. The total power at the fundamental

---

[3] For simplicity, an AR coated bare crystal is desirable. If problems with coating damage do occur, it is possible to enclose an uncoated nonlinear crystal in a long-length cell containing index matching fluid, then to focus the high power fundamental beams into the crystal from a distance, keeping the spot size at the AR-coated entrance faces of the cell large to avoid peak power damage.

Spot size (mm)	Fluence (J/cm^2)
0.1	18.4
0.2	4.6
0.3	2.0
0.4	1.1
0.5	0.5

Table 2.2: The peak fluence of micro-pulses for a 100 W average power macro-micro-pulsed laser for different laser spot sizes.

wavelengths (1064 nm and 1319 nm) was 100 W. The peak fluence estimations for different spot sizes are found in Table 2.2. The damage thresholds of optical coatings are usually specified for pulse duration 10 or 20 ns and for peak power damage these values scale as the square root of the pulse width for pulses longer than 100 ps [60]. Hence a damage threshold of 10 J/cm^2, 20 ns pulse is equivalent to 2.2 J/cm^2 for one nanosecond pulses. Comparing this value with the data of Table 2.2 we see that the spot size should be kept above 0.3 mm to avoid damage.

To have equal numbers of photons at the two wavelengths, the average power at 1064 nm should be 55.5 W while at 1319 nm the power should be 45.5 W. This is beneficial to SFG guide star systems as Nd:YAG lases more efficiently at 1064 nm than 1319 nm [61].

Results

Table 2.3 shows the conversion efficiencies calculated using the SNLO computer program for single pass SFG of 55.5 W 1064 nm and 45.5 W 1319nm macro-micro pulsed beams in a 2 cm LBO crystal. The crystal length of 2 cm is the longest length found to be available from vendors of high quality LBO. The crystal temperature was set to 39 ℃ for non-critical phase matching and zero walk-off. The approximate, analytical expression for conversion efficiency (Equation 2.9) predicts conversion efficiencies slightly higher than Table 2.3. Using the same input parameters of pulse length, spotsize, crystal length etc as the SNLO program, Equation 2.9 predicts a conversion efficiency of 71 % for a spotsize of 0.5 mm and 90 % for a spotsize of 0.3 mm.

Table 2.3 shows that a theoretical conversion efficiency of 76 % can be obtained for a 0.3 mm spot size. In practice this is would be the upper limit to the single-pass efficiency as it assumes that there is zero jitter between micro-pulses, the 1064 nm and 1319 nm macro-pulse shapes are perfectly matched, the fundamentals have perfect beam quality and there is no loss or wavefront distortion in the LBO crystal. If any of these parameters are less

Spotsize (mm)	Efficiency (%)
0.2	86.8
0.3	76.0
0.4	64.5
0.5	54.0

Table 2.3: The calculated SFG conversion efficiency for 1064 nm and 1319 nm beams focused to different spot sizes within a LBO crystal.

than ideal in the final laser system the efficiency will be reduced from the theoretical value.

It may also be possible to use multiple LBO crystals in series and pass unused 1064 nm and 1319 nm power from the first SFG stage through a second stage and further improve the efficiency.

Conclusions

This section presented a theoretical analysis of the high power SFG stage proposed for the guide star system design. Several different nonlinear materials were investigated and it was concluded that Lithium Triborate (LBO) would be the preferred material for SFG as it has been proven to withstand high average powers, give good conversion efficiency and it can be temperature tuned for non-critical phase matching and zero walk-off. The conversion efficiency of a LBO crystal was calculated in Section 2.5.4 for macro-micro pulse laser waveforms similar to that expected from the 1064 nm and 1319 nm injection mode-locked lasers. It was found that the conversion efficiency could be as high as 76 % for a single pass through a 2 cm LBO crystal, with higher efficiencies possible if multiple crystals are used in series. Hence this section established that the high-peak-power of the injection mode-locked oscillators will allow a simple and efficient single pass SFG stage to be used for the guide star system, and that a combined average power of 100 W for the 1064 nm and 1319 nm beams should be sufficienct to generate 50 W of 589 nm power. This predicted value is similar to the efficiency recorded by Tracy et al. [19], who achieved 40 % conversion efficiency from lower peak power cw mode-locked Nd:YAG lasers.

Detailed experimental investigations are, of course, necessary to determine the exact conversion efficiency obtainable for the injection mode-locked lasers when non-ideal factors such as the specific pulse format and beam quality of the lasers are taken into account.

2.6 Power scaling

In this section, several design options are discussed for scaling the average power of the guide star system to 50 W, as required by Gemini. The approaches discussed in this section are:

1. Having a single high average power oscillator in each of the 1064 nm and 1319 nm lasers to achieve 50 W at the sodium wavelength in one step
2. having 5 identical, subscale, 10 W systems to achieve a total of 50 W
3. having a power amplifier to boost the power levels of 1064 nm and 1319 nm oscillators.

Final design details are not presented in this section as the power scaling of the Na system to 50 W is not a part of this thesis.

2.6.1 Design options

High average power Nd:YAG oscillators

The design that potentially requires the fewest optical components is one which uses a single high average power oscillator at 1064 nm, and a single high average power oscillator at 1319 nm to produce the required 50 W, Na. This would require around 55.5 W from the 1064 nm oscillator and 45.5 W at 1319 nm as discussed in Section 2.5.4.

To date, the highest average power reported from an electro-optically Q-switched, Nd:YAG oscillator operating in a stable, TEM_{00} cavity is around 10 - 20 W [62] [63] [64][4] at 1064 nm, so obtaining significantly high average powers than this may prove difficult. The thermal distortions such as thermal birefringence and thermal lensing usually limit the output power in high average power Nd:YAG laser heads, as is discussed in detail during Chapter 5.

5 x 10 W oscillators

A different design is to use 5 identical, lower average power oscillators (5 x 10 W) to achieve 50 W in total. Each laser system could then be used to produce one of the five beacons required for MCAO. This approach has the advantage that if a technical

---

[4] Researchers of high powered near infra-red lasers have primarily focused on Yb:YAG and $Nd:YVO_4$ when developing single oscillator systems due to the better quantum defect and thermal properties of these materials [65] [66] [67], but they cannot be used for SFG guide star systems due to their emission wavelength.

problem arises with one of the lasers at the observatory and requires repairs, the adaptive optics system could still be used to correct for turbulence using the 4 remaining beacons (although the performance of the system will be reduced), and would not require the shut down of the adaptive optics system.

This approach is also a safer research option to pursue as the Nd:YAG laser technology has already been demonstrated at these power levels [62] [63] [64].

A disadvantage with this approach is the increased system complexity as 10 medium power oscillators (five at 1064 nm and five at 1319 nm) will be required.

2.6.2 Master oscillator power amplifiers

Another approach to power scaling is to use a low average power master oscillator (approx. 2 W) to produce the desired macro-micro pulse waveform, and then use an amplification stage to boost the power to the required level. This technique is known as a master oscillator power amplifier (MOPA).

High average powers have been achieved with this technique, with several systems reporting in excess of 50 W with Nd:YAG (and Yb:YAG) [68] [69] [70] [71]. MOPAs have an advantage over high average power oscillators in that the major heat load (from pumping) is removed from the oscillator laser crystal, thereby limiting the number of times the laser beam must pass through a gain medium with high heat load and potential thermal distortions.

Potential issues with this approach are whether the wavelength and beam quality of the master beam can be preserved during amplification.

2.7 Comments 1319 nm lasers

The operation of Nd:YAG lasers at 1319 nm is more challenging than at 1064 nm primary due to the lower emission cross section at that wavelength: 0.95×10^{-19} cm^2 for 1319 vs. 2.8×10^{-19} cm^2 for 1064 nm. Hence Nd:YAG will preferentially lase at 1064 nm so this emission needs to be suppressed to allow the 1319 nm power to build up. 1319 nm operation can be achieved using narrow-band mirrors made from multi-layer dielectric coatings that are highly reflective at 1319 nm and transmissive at 1064 nm, but the lower gain at 1319 nm will still result in lower average powers at 1064 nm for a given pump power. Tracy et al [19] reported an output power of 16.8 W at 1064 nm and 9.8 W at 1319 nm using cw mode-locked lasers while Denman et al [18] reported 100 W at 1064 nm and 60 W at 1319 nm in a cw beam.

In Section 4.3 a model is presented for predicting the output of an injection mode-locked Q-switched Nd:YAG laser. This model accurately reproduces the 1064 nm output pulse energy and pulse width of the laser described in Chapter 3 for a range of pump energies (Figure 4.3). This model was used to provide an indication of the performance expected from an injection mode-locked, Q-switched laser at 1319 nm relative to an identical laser operating at 1064 nm. Full details of the model are presented in Chapter 4 and only the results are given here. At 1064 nm, for a small-signal gain coefficient $g_0 = 0.307$, the model predicts that the laser will output 10 mJ in an injection mode-locked, Q-switched pulse with a near-Gaussian-shaped pulse having width 0.4 μs. For 1319 nm, a small-signal gain coefficient $g_0 = 0.102$ was input, representing the one third stimulated emission cross section at this wavelength. With all other parameters identical, the model predicts output energy of 1 mJ and a pulse width of 1.9 μs, highlighting the difficulty expected at this wavelength.

To increase the power from a 1319 nm laser, the pump density within the laser crystal can be increased, either by reducing the dimensions of the Nd:YAG gain medium or by increasing the pump energy. This approach will only be effective if there are no performance limitations from thermal lensing or parasitic oscillations for example.

Another challenge will be overlaying the 1064 nm and 1319 nm macro-pulses in the SFG crystal for high-efficiency SFG. The different gains at the two wavelengths will result in different Q-switch build up times so to synchronize macro-pulses the 1064 nm macro-pulse will need to be delayed relative to 1319 nm. As was discussed in Section 2.2, to achieve low timing jitter between micro-pulses the Pockels cells in the seed pulse generator should be driven using the same drive pulse, so the 1064 nm and 1319 nm seed pulses will be generated at approximately the same time. It may be possible, however, to delay the injection of the 1064 nm seed pulse into the slave resonator to account for the difference in build up times by using an optical fibre delay line and adjust the length of the delay line to synchronize macro-pulses. Macro-pulse shapes should also be matched for high SFG efficiency, which may be possible using the Q-switch pulse modulation techniques described in Chapter 4.

A demonstration of high-average-power injection mode-locked laser power at 1319 nm laser is not a part of this thesis.

2.8 Frequency locking to the sodium line

A robust frequency lock is required to guarantee that the slave lasers are accurately tuned to generate sodium light by SFG. The Doppler broadened line width of the atmospheric

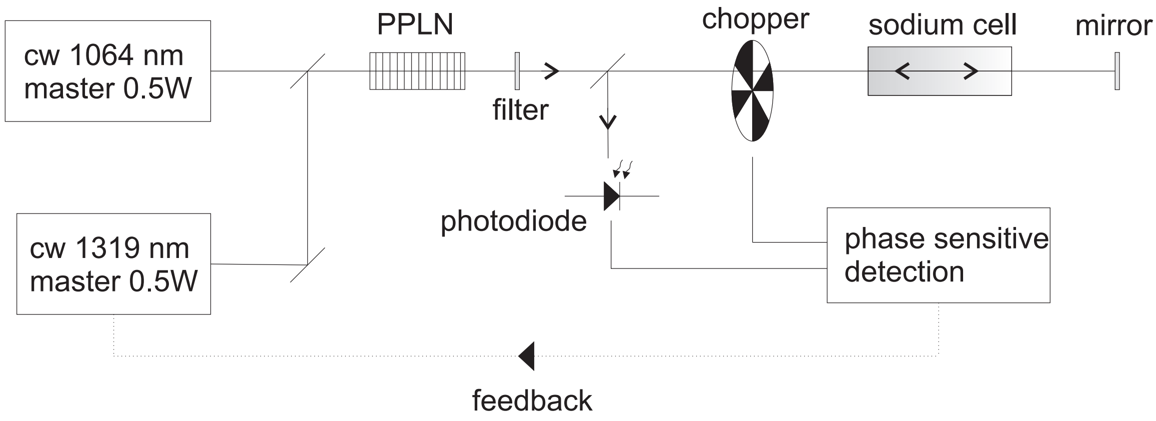

Figure 2.9: The master oscillators are locked to the sodium D2a line using low power SFG in PPLN and a double pass through a sodium cell to generate an error signal which is fed back to one of the master oscillators. Phase sensitive detection is used to reduce the noise of the system.

sodium D2a line is about 3 GHz [72] and thus the frequency drift of the slave oscillators should be kept well within this limit to maintain a high photon return from the guide star.

Frequency locking of the injection mode-locked guide star source can be achieved by using the NPRO master lasers to drive a secondary, low power SFG stage to illuminate a sodium cell and provide an absolute reference to the sodium absorption band. A simple feedback system can then be used to control the temperature of the NPRO crystal and accurately tune the wavelength to enable a robust independent lock to the sodium line. This technique has already been demonstrated by Moosmuller et al. [39] and also in-house by N. Simakov [33]. The work of the latter is discussed in this section to show the viability of the approach.

A schematic of the set up used by Simakov is shown in Figure 2.9. This system uses two 0.5 W NPRO's and periodically poled lithium niobate (PPLN) to generate 11 mW of Na light to illuminate a sodium cell. Phase sensitive detection is used to generate a low noise error signal which is fed back to the temperature control unit of the 1319 nm NPRO for frequency control. With this set-up the frequency was maintained to within 3 MHz of the sodium D2a line for long periods. This represents a drift of approximately one 1000^{th} of the Na absorption bandwidth showing that the output of the injection mode-locked guide star can be held at precisely the right wavelength for maximal guide star brightness.

2.9 Conclusions

This chapter presented a system design for an injection mode-locked guide star source that can potentially meet the Gemini performance requirements of Table 1.1. The design is based on SFG of injection mode locked Nd:YAG lasers to provide both power scalability and also the spectral, wavelength and timing properties required of the guide star.

Injection mode locking was discussed in Section 2.3 then a new resonator design was presented in Section 2.4 that facilitates both injection mode-locking and stretched Q-switching. This resonator design is used for the experimental investigations of injection mode-locking, pulse stretching and power scaling found in later chapters of this thesis and has been found to be very successful at achieving the required laser pulse format with high efficiency.

Section 2.5 presented an analysis of the high powered SFG system required to generate the Na light and concluded that the high-peak-power of the injection mode-locked macro-micro pulse waveform generated by the injection mode-locked slave lasers will enable efficient conversion to 589 nm with a simple single pass SFG system in LBO.

Section 2.6 presented a discussion of approaches to scaling the average power of the guide star laser, then in Section 2.8, the design of the frequency locking servo was described which can hold the frequency of the master lasers to within 3 MHz of the Na line.

The remainder of this thesis describes the experimental verification of injection mode-locking, Q-switched pulse stretching and power scaling in a 1064 nm Nd:YAG oscillator and includes experimental evidence justifying some parts of the guide star system design. Other sections from this chapter, such as the design of the high power SFG stage and MOPA remain as a design only and experimental validation of these aspects remains for future work.

Chapter 3

Design verification experiments using a subscale, 1064 nm Nd:YAG laser

3.1 Objective

To verify key concepts of the injection mode-locked laser guide star design a low power, a subscale 1064 nm laser was built and tested. While this laser was not designed to handle the high thermal loadings required for a 10 W average power laser, it was capable of reaching the same energy per macro-pulse required of the final laser, but at a repetition rate of 50 Hz, instead of the 800 Hz required of the final design. Nevertheless, a number of key design features such as injection mode-locking, timing jitter, bandwidth and wavelength control could all be verified with this low average power proof-of-principle laser.

Injection mode-locking has been previously used to produce short pulses in CO_2 [40] and Nd:YAG [43], but to the best of the author's knowledge at the time of this work, there has been no description of injection mode-locking being applied to Nd:YAG to produce long macro-pulses consisting of many micro-pulses with simultaneous control of the bandwidth.

This chapter presents the design and characterisation of an injection mode-locked Nd:YAG oscillator. It begins with a description of the Nd:YAG laser head in Section 3.2 with details of the Nd:YAG crystal geometry, pumping and cooling configuration and multi-mode power output. Then Section 3.3 describes the resonator design and the combination of intracavity telescopes and resonator length required to achieve dynamic stability. A Description of the seed pulse source is given in Section 3.4 for which measurements are presented that show variable duration sub-nanosecond seed pulses can be created. In

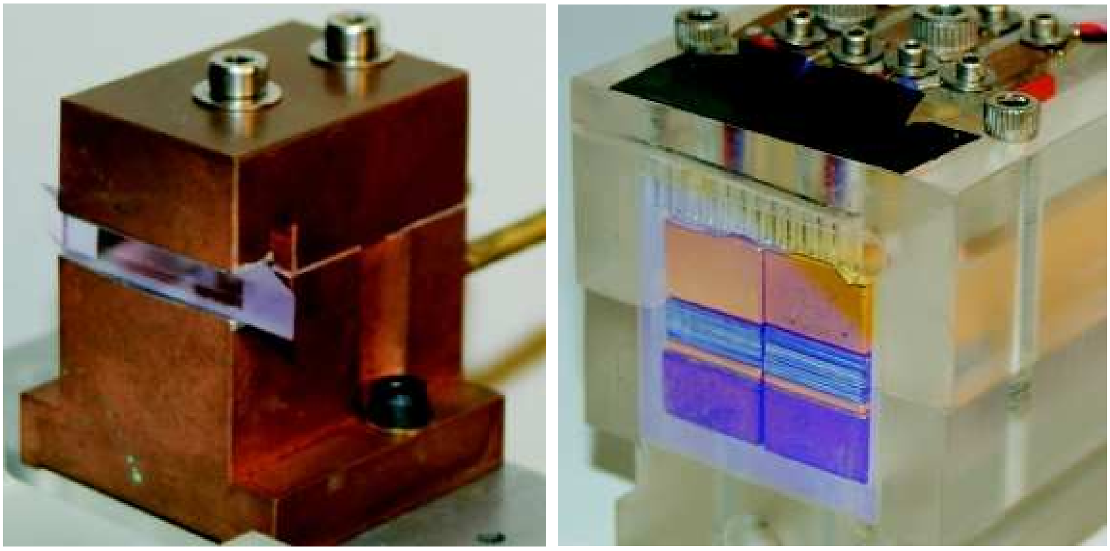

(a) (b)

Figure 3.1: The side-pumped, top and bottom cooled, Brewster-angled Nd:YAG slab, a), and laser diode arrays, b), used for the design verification experiments.

Section 3.6 injection mode locking in Nd:YAG is demonstrated. Results are presented that show the laser's spectral bandwidth can be controlled over a useful range and the timing jitter of the micro-pulses is sufficiently low.

3.2 Laser head

The proof-of-principle laser head, in part provided courtesy of TRW Inc., consists of a 1 at. % doped Nd:YAG zigzag slab with Brewster-angled entrance and exit faces and measures 4.32 mm in width, 4.00 mm in height and 36.14 mm in length [73]. The slab is side-pumped in the zigzag plane by two 808 nm quasi-cw laser diode arrays and is clamped between copper blocks to enable conduction cooling through the top and bottom surfaces. The copper blocks and the laser diode arrays were water cooled. Figure 3.1 shows pictures of the laser crystal, clamping arrangement and pump diodes.

Each laser diode array was driven by a quasi-cw laser diode driver capable of delivering 80 A, 200 μs pulse-width drive pulses at a maximum repetition rate of 50 Hz. The pulse energy from the laser diode arrays is shown plotted in Figure 3.2.

This laser head was tested by using a short standing-wave resonator with two flat mirrors; one maximum reflectivity 1064 nm mirror and the other a 1064 nm output coupler of 75 % reflectivity. This test resonator was assembled to assess the performance of the

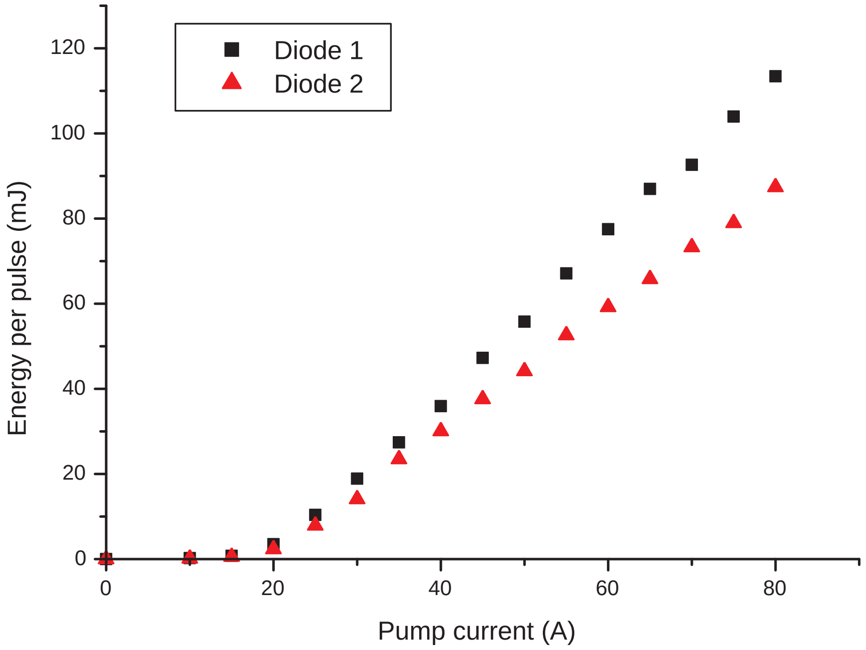

Figure 3.2: Laser pump energy produced by the laser diode arrays shown in figure 3.1(b).

laser head and to provide an estimate of the amount of 1064 nm laser power available for extraction. The output power from this resonator is plotted in Figure 3.3 showing that a maximum 1064 nm output energy of 60 mJ was obtained with a slope efficiency of 46 %.

The results from other zigzag slab lasers reported in the literature show a reduction in slope efficiency of around one half to two thirds when running in a single transverse mode as compared to muli-mode [74], and this reduction would correspond to a reduction in pulse energy from 60 mJ to 20-30 mJ for this laser system, which in excess of the 10-15 mJ required from this proof-of-principle laser. This is verified experimentally in Section 3.6.2.

3.3 Slave resonator design details

The slave laser head was included in a travelling wave ring resonator for injection mode-locking. The design of the resonator was discussed in Section 2.4 and a schematic of the design showing the zigzag slab and other intracavity elements is displayed in Figure 3.4. This set-up was used to obtain the experimental results presented in this chapter.

A π-polarized seed pulse is injected through the TFP for injection mode-locking and converted to σ by the half wave plate. The Brewster angled windows of the laser slab cause

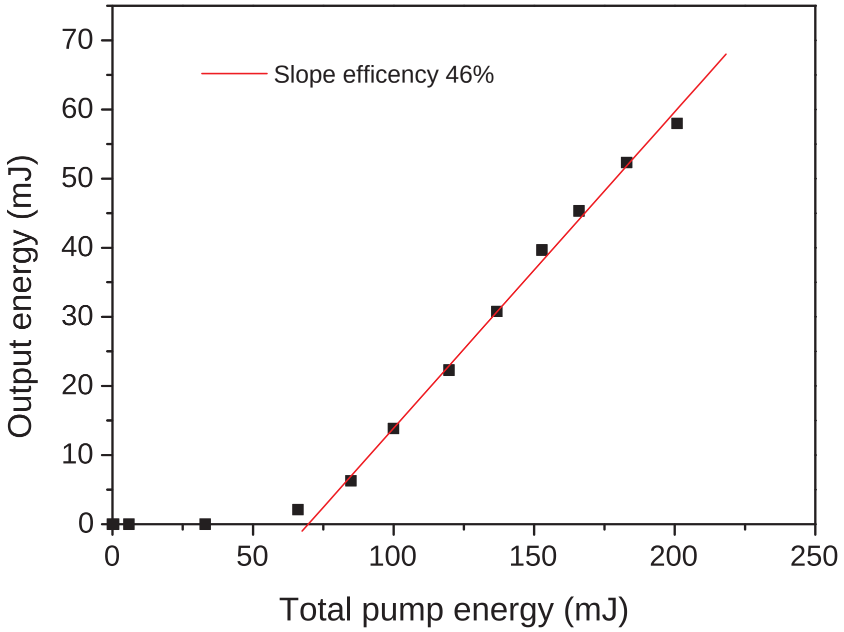

Figure 3.3: Output energy using a flat-flat standing-wave resonator with one max-R mirror and a R=75 % output coupler.

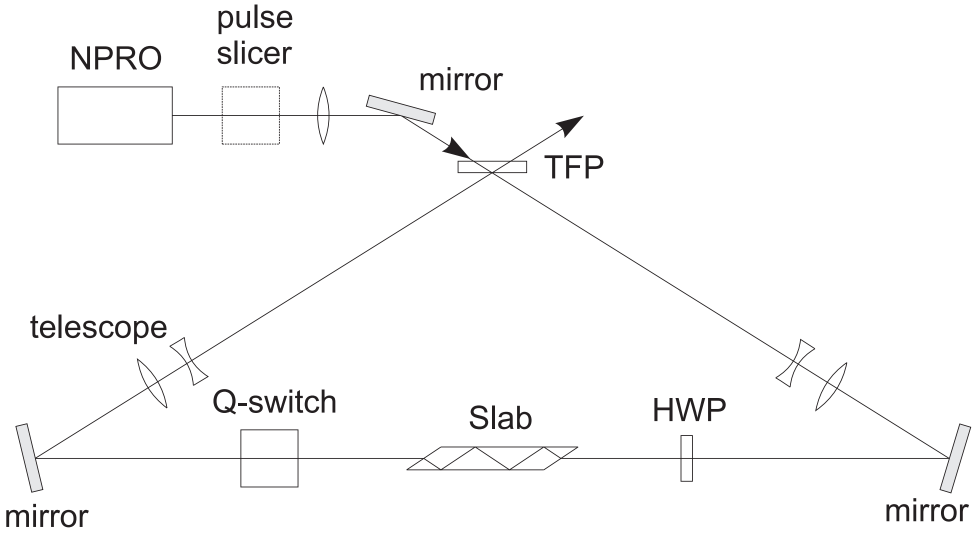

Figure 3.4: A schematic of the ring laser used for the proof-of-principle tests. The design uses a zigzag Nd:YAG slab, KD*P Q-switch and a combination of polarizer (TFP) and half wave plate (HWP) to facilitate injection mode-locking and pulse stretching. Telescopes are included to reduce the resonator length while maintaining dynamic stability.

a 30 % reflection loss on the first round trip, but before the second round trip, voltage is applied to the Q-switch and the now pi-polarized pulse builds up rapidly with low loss. The Q-switch is a dual crystal KD*P cell, with a half wave voltage of 3.4 kV for 1064 nm. This cell was used for these initial experiments as it was available from a previous project, but was replaced with a BBO cell for later work as discussed in section 4.2.

The resonator was configured for maximum dynamic stability by optimising the resonator length and incuding intra-cavity telescopes. These topics will be discussed in the following sections.

3.3.1 Resonator stability

With high power lasers, the large pump power and quantum defect can lead to significant amounts of heat deposited in the laser crystal. A well-designed laser head will minimize thermal wavefront distortion, but there will inevitably be some effects such as thermal lensing and thermal birefringence [75]. With careful design of the resonator architecture, however, the effect of this distortion can be reduced. Thermal birefringence, for example, can be compensated by using two laser heads with an intermediate quarter-wave plate to cancel out birefringence [76], but with a slab-type laser crystal, as was chosen for this work, the effects of thermal bi-refringence are already reduced by the zigzag optical path [77]. Thermal lensing however, is still a problem in slab lasers and if it is not accounted for in the design of the resonator the maximum TEM_{00} mode power obtainable will be reduced. Furthermore, lasers are often required to operate in conditions where the thermal lens changes with time. These changes could be caused by changes in pump power, if the laser is required to operate at different average powers, or could be due to aging effects such as the deterioration of laser diode output, or misalignments of the cavity optics resulting in different amounts of energy being extracted from the laser head. Hence it is often required that a laser has dynamic stability [78].

Dynamic stability is achieved if the spotsize of the laser mode inside the slab, ω_{slab}, is made insensitive to changes in the focal power of the induced thermal lens, f_{therm}. If the mode is too large, then losses can occur due to the beam clipping on the slab edges and conversely, if the beam is too small then it will not adequately overlap the pumped volume resulting in inefficient energy extraction. So for dynamic stability, the required condition is:

$$\frac{\partial \omega_{slab}}{\partial f_{therm}} = 0 \tag{3.1}$$

To see how this equation applies to the ring resonator of figure 3.4, we first consider the ring resonator without intra-cavity telescopes as shown in figure 3.5. The inclusion of the

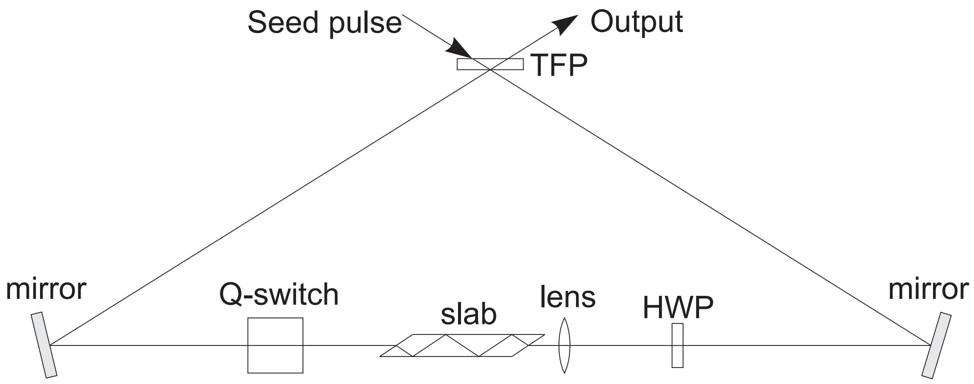

Figure 3.5: A traveling ring resonator similar to Figure 3.4 but with no intra-cavity telescopes and with a stabilizing lens.

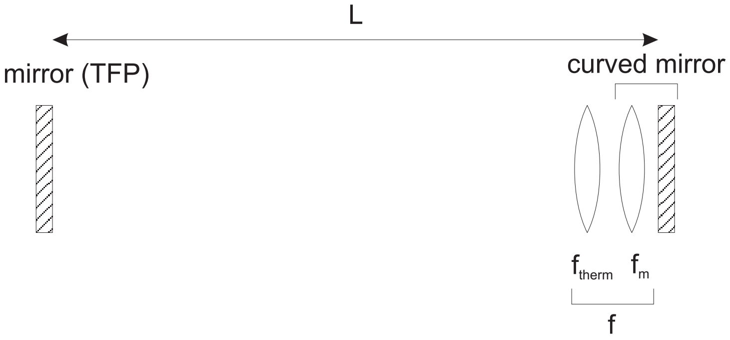

Figure 3.6: A standingwave hemispherical resonator with the same ABCD matrix as Figure 3.5.

telescopes is treated later, in Section 3.3.2.

To apply equation 3.1 to the resonator of Figure 3.5 it is necessary to have an analytic expression for ω_{slab}, written in terms of other resonator parameters. This can be obtained by treating the ring resonator as a standing wave hemispherical resonator, for which a simple equation for ω_{slab} already exists. This treatment is legitimate, provided the two resonators are equivalent, ie. they have identical round trip ABCD matricies. An example equivalent resonator is shown in Figure 3.6, for which the slab is represented by a lens of focal length f_{therm} and the curved mirror is represented by the combination of the lens, f_m, and flat mirror.

It can be shown that for a hemispherical resonator, the spotsize at the right hand side mirror, ω_{slab}, is given by [79]

$$\omega_{slab}^2 = \frac{\lambda f}{\pi}\sqrt{\frac{L}{f-L}} \tag{3.2}$$

with $f = f_{therm} + f_m$. Taking the derivative of equation 3.2 with respect to f_{therm} gives

$$\frac{\partial \omega_{slab}}{\partial f_{therm}} = \frac{1}{4}\left(\frac{f-2L}{f-L}\right)\left(1+\frac{f_{therm}}{f_m}\right)^{-1}\frac{\omega_{slab}}{f_{therm}} \tag{3.3}$$

from which we see that the condition for dynamic stability, equation 3.1, occurs when $f = 2L$, which requires that

$$L = \frac{\omega_{slab}^2 \pi}{2\lambda} \tag{3.4}$$

Equation 3.4 shows that the required cavity length, L, is dependent on the square of the spotsize ω_{slab}.

For the proof-of-principle laser head of a beam size ω_{slab} =1.2 mm is required to adequately fill the crystal aperture and efficiently extract the available pump energy. So, if operating at 1064 nm, equation 3.4 implies a cavity round trip length of 4.25 m is required to achieve dynamic stability, while if operating at 1319 nm, the length is 3.43 m. Both of these lengths are comfortably in excess of the minimum length required for robust injection mode-locking with seed pulse durations of 1 ns, as discussed in Section 2.3. A resonator length of 4.25 m will have a free spectral range (FSR) of 70 MHz[1], meaning that approximately 14 longitudinal modes will contribute to a mode-locked pulse of bandwidth 1 GHz.

3.3.2 Intra-cavity telescopes

Hanna [78] has shown that the introduction of intra-cavity telescopes allows the resonator length to be reduced while maintaining dynamic stability. With an intra-cavity telescope, the expression for the cavity length, equation 3.4 becomes [78]

$$L = \frac{\omega_{slab}^2 \pi}{2M^2\lambda} \tag{3.5}$$

where M is the telescope magnification. An intra-cavity telescope may be useful in the final guide star laser design, as it allows a spotsize larger than 1.2 mm to be used, reducing the risk of damage to optics from the high-peak-power micro-pulses, without requiring an impractically large resonator length to maintain dynamic stability. An intra-cavity telescope could also be used in the 1064 nm laser to reduce its length from 4.25 m to 3.43 m, making the length of the 1064 nm and 1319 nm slave lasers equal and thus ensuring proper overlap of 1064 nm and 1319 nm micro-pulses in the SFG crystal. For these reasons, the subscale, 1064 nm slave laser had intra-cavity telescopes incorporated in its resonator design, as shown in Figure 3.4, to test the viability of this concept.

---

[1] For a ring resonator FSR=c/L where c is the speed of light and L is the round trip length.

3.4 Seed pulse generator

To injection mode-lock the slave laser, a wavelength tuneable, transform limited seed pulse is required, with a pulse-width that can be adjusted to set the required bandwidth. Previous authors have reported the generation of seed pulses by gating a single pulse out of a cw mode-locked master laser [43] or by slicing the seed pulse from a single-frequency cw beam using a Pockels cell (PC) and fast driver [40]. We chose the latter technique for its simplicity and ease of wavelength control when using a cw NPRO as the master laser. To drive the PC, high voltage pulses of nanosecond or sub-nanosecond duration are required, which can be produced using avalanche transistor circuits [80]. These devices can produce pulses with amplitudes of over 4 kV and rise times of 100 ps, as well as having long lifetimes, of the order of 10^{10} shots, making them suitable for guide star applications. It is difficult to create a high voltage pulse source with a variable pulse duration using these devices, however. We thus employed a dual Pockels cell system, shown in Figure 3.7, that uses two fast, 50 ohm Pockels cells [81], each driven by an independent avalanche transistor driver [82]. In this system, the first Pockels cell (PC_1) receives a 100 ps rise time, 1 ns duration, 4 kV voltage pulse, creating the leading edge of the optical seed pulse, then after a short delay, a 100 ps rise time, 3 ns duration, 4 kV voltage pulse is applied to PC_2, producing the trailing edge of the seed pulse. The delay between firing the first and second PC sets the seed pulse width. The delay was introduced by controlling the arrival time of the trigger pulse to the 3 ns PC driver using an in-house built zero-jitter control box shown in Appendix B.1. This device can implement delays ranging between 0 and 3 ns in 100 ps steps by switching in different lengths of coaxial cable to delay the trigger pulse.

Traces of the high voltage PC drive pulses from the 1 ns and 3 ns pulsers are displayed in Figure 3.8(a) and Figure 3.8(b), which were taken using a fast sampling oscilloscope after a 78 dB attenuation, using the high voltage, high bandwidth attenuator described in Appendix C.

Using the dual Pockels cell pulse slicing technique, optical seed pulses with widths between 200 ps and 1 ns have been produced, with examples shown in Figure 3.9. The near-cw light rejected by the second polarizer in Figure 3.7 could be used to provide a cw reference to the sodium wavelength via a secondary SFG system, as discussed in Section 2.2.

As can be seen in Figure 3.8, the electrical pulses produced by the avalanche transistor pulsers have significant post-pulse noise, typical of these devices [80]. This noise would manifest itself as a tail to the seed pulses if a single PC system is used. By having a second

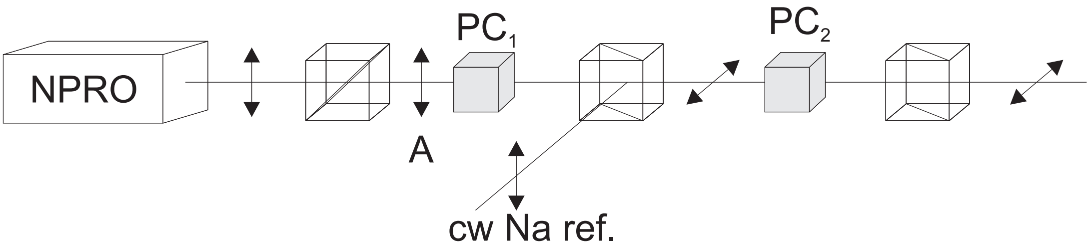

Figure 3.7: The dual Pockels cell pulse slicer used to create variable duration seed pulses for injection mode-locking. It consists of a single frequency cw master source (NPRO) two Pockels cells, PC$_1$ and PC$_2$, and three polarizers. The double-headed arrows indicate the polarization of the light. The near-cw light reflected off the second polarizer can be used to provide a cw reference to the sodium wavelength. If a half wave plate is inserted at point “A”, a cw beam is transmitted through the system that can be used for alignment purposes.

PC that is diven by a long duration electrical pulse, the noise tails will be extinguished as all light incident on the third polarizer in Figure 3.7 will be reflected while PC2 has half wave volts. The extinction of the post-pulse noise is demonstrated in Figure 3.9(d) which shows a clean seed pulse with little trailing noise. This represents another significant advantage of the dual PC seed pulse source over a single PC system.

With the fast 50 ohm PCs used in this system [81], the PC behaves like a section of a 50 ohm transmission line, so the high voltage drive pulse applied to the cell needs to be terminated once it has passed through, to avoid back-reflections. To do this, the exit port of the PC was connected to a 100 m length of RG 58 coaxial cable, which attenuates the high frequency components of the pulse (eg. by 36 dB/100 m at 400 MHz frequencies and greater for higher frequencies [83]) and terminated by a series-parallel combination of carbon film resistors. It was observed that the drive pulse exiting the PC appeared to be unchanged after passing through the cell and could possibly be used to drive either the second PC via an intermediate length of cable, or it could be used to drive PC$_1$ in the 1319 nm laser system, resulting in zero timing jitter between 1064 nm and 1319 nm micro-pulses, thereby improoving the SFG efficiency.

3.5 Q-switch driver

To trap the injected seed pulse inside the ring, the Q-switch is changed from no polarization rotation to half-wave rotation in approximately the time it takes the seed pulse to make one round trip of the ring resonator. If the Q-switch is driven slower than this then the resulting large out-coupling fraction for the π-polarized pulse could attenuate the seed

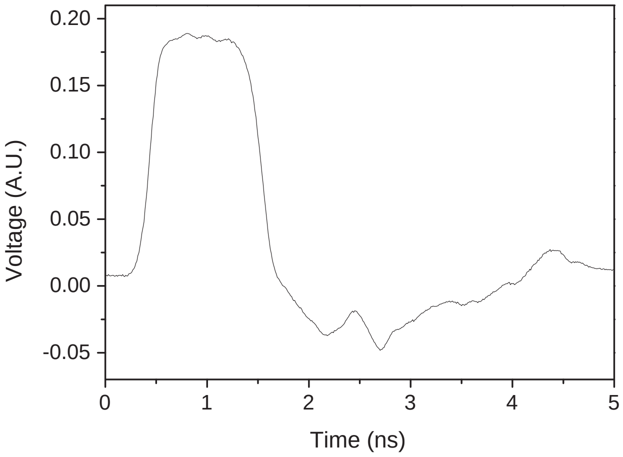

(a) 1ns

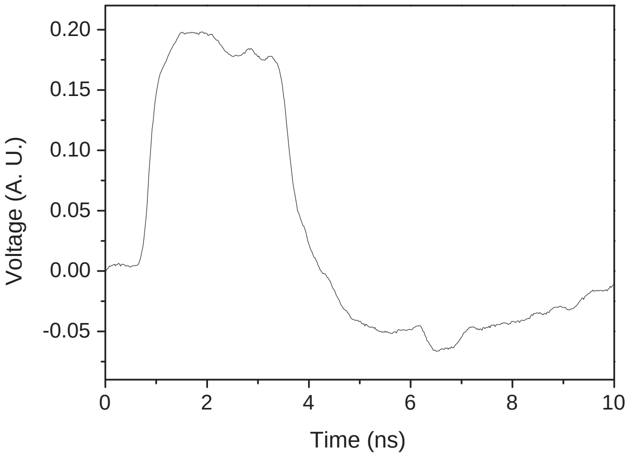

(b)

Figure 3.8: Measured high voltage electrical pulses from the (a 1 ns and (b) 3 ns avalanche transistor pulsers. The pulses were attenuated using the in-house built high voltage high bandwidth attenuator described in Appendix C. The measurement bandwidth is 2 GHz.

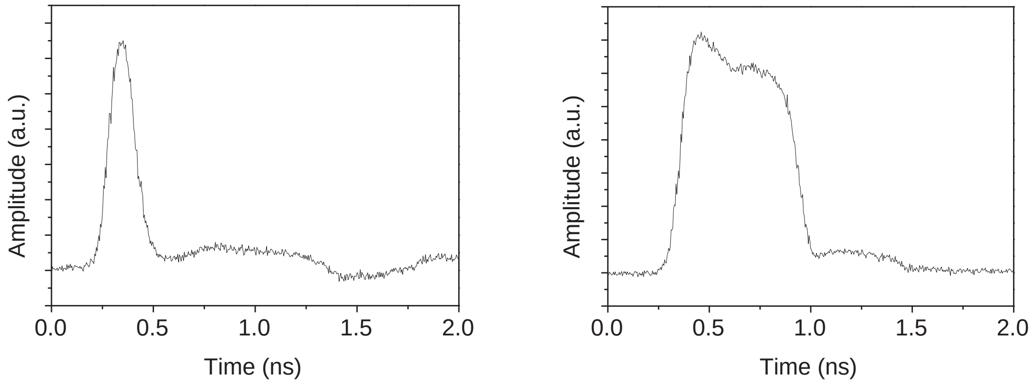

(a) FWHM = 0.2 ns

(b) FWHM = 0.6 ns

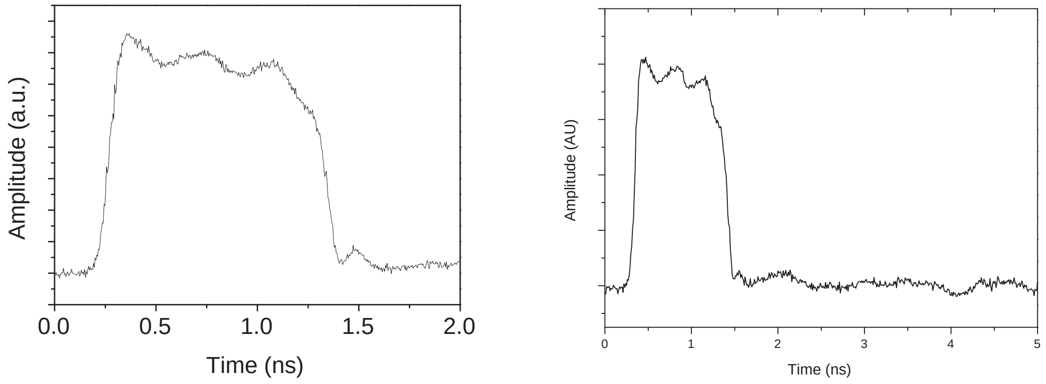

(c) FWHM = 1 ns

(d) FWHM = 1 ns

Figure 3.9: Example of variable duration optical pulses prduced by the pulse slicer of Figure 3.7. These measurements were taken using a 12 GHz photodiode and 20 GHz sampling oscilloscope

pulse below the noise level of amplified spontaneous emission and the slave would not be injection mode-locked. The Q-switch drive pulse, therefore, needs a rise time from 0 V to 3.4 kV of approximately 10 ns. In addition, the long duration of the output pulses from this laser require a drive pulse width in excess of 1 μs. Circuits that can deliver either fast rise times or long duration pulses exsist in the literature [84] [85] [86] as these circuits are commonly used for lasers that have high or low gain respectively. But for a low-gain injection mode-locked source, the Q-switch drive pulse needs a combination of the two. Circuit designs for this type of device have not previously been published. Work was therefore undertaken to produce a fast rise time, long pulse width Q-switch driver suitable for use in the injection mode-locked oscilator described in this chapter. Details of this work were published [87] and can be found in Appendix A.

3.6 Injection mode-locked slave laser performance

3.6.1 Aligning the ring oscillator

To align the slave resonator, the laser was first set in standing-wave configuration using two flat output couplers, specifically selected for low wedge angle. The beam emanating from each side was used to align the Q-switch, mirrors, telescopes, HWP and TFP of the ring resonator (Figure 3.4). Care was taken to set the TFP at the exact angle required to provide maximum reflection of σ-polarization while simultaneously transmitting maximum π. Several TFP's were examined and the one with highest reflection and lowest transmission was selected.

3.6.2 Pulse energy

To couple the seed pulse energy into the slave resonator efficiently, the seed pulse source (i.e. the NPRO) must be mode matched to the resonator. To do this, the mode size and divergence angle of the seed pulse beam must be the same as the mode size and divergence angle of the slave mode inside the resonator [88].

To mode-match the seed beam, a half wave plate was inserted between the first polarizer and first Pockels cell of the seed pulse generator (point “A” on Figure 3.7) to allow the cw NPRO beam to pass through the pulse slicer for alignment purposes. The mode size of this beam was measured using a CCD camera. Then, to mode-match the seed beam onto the slave mode, a single lens with focal length f =1.5 m was inserted between the NPRO and the outcoupler of the slave (shown on Figure 3.4). Afterwards, the half wave plate was removed, and the seed pulses produced by the pulse slicer were used to injection

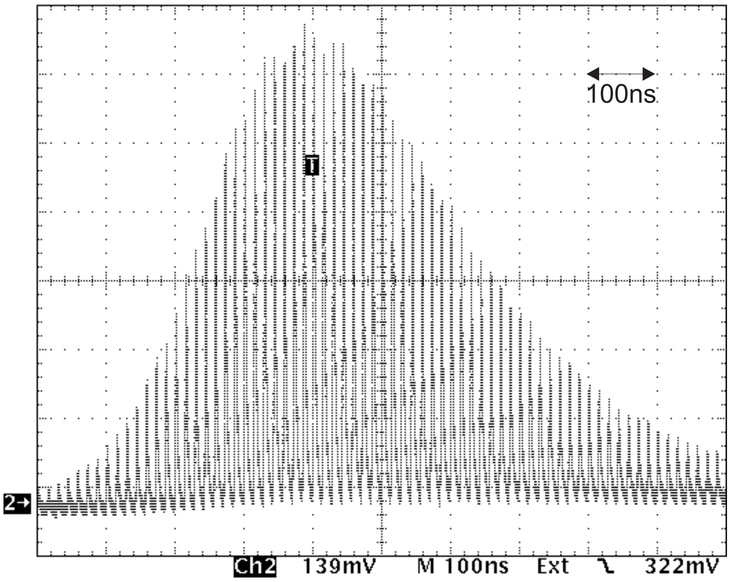

Figure 3.10: Injection mode-locked output from the slave laser showing a burst of short micro-pulses with the overall macro-pulse envelope of a Q-switched laser.

mode-lock the slave resonator to produce the macro-micro pulse burst waveform shown in Figure 3.10. This waveform consists of a series of short 1 ns micro-pulses, separated by the round trip time of the resonator (around 12 ns), as required for the guide star design. The laser produced pulse energies in excess of 15 mJ in a near-diffraction-limited beam (97 % fit to gaussian) at a repetition rate of 50 Hz. Figure 3.11 shows the output pulse energy of the laser. The slope efficiency is 16 %.

It was observed that the output micro-pulse shape closely resembled the input seed pulses. Traces of a seed pulse overlayed with an output micro pulse are displayed in Figure 3.12.

3.6.3 Micro-pulse jitter

For the injection mode-locked guide star design to be viable, it is critical that the timing jitter between 1064 nm and 1319 nm micro-pulses be small compared to the micro-pulse width to ensure good SFG efficiency using the high-peak-power macro-micro pulse burst waveform. To measure the timing jitter, the leading edge of an individual micro pulse was monitored over many macro-pulses using a 12 GHz photodiode and 20 GHz sampling oscilloscope. The oscilloscope was independently triggered by a commercial, low-jitter trigger generator at a fixed time after the trigger given to the first avalanche transistor pulser in the pulse slicer. The scatter in arival time of the micro-pulse edge is a measure of the combined jitter from the trigger generator, avalanche transistor pulser and any

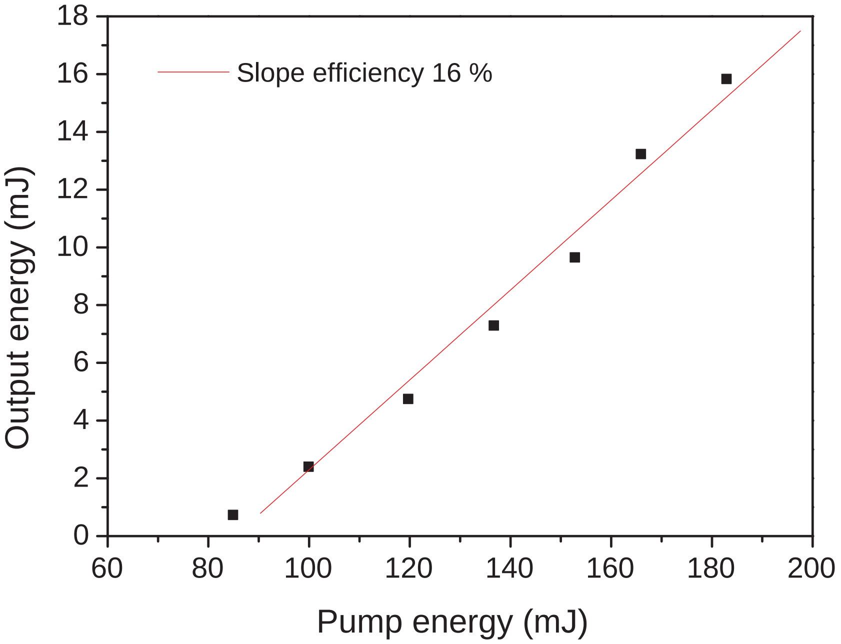

Figure 3.11: Output energy of the injection mode-locked slave laser.

jitter due to seed pulse amplification in the slave laser. The total jitter was measured to be less than 12 ps rms. An example screenshot of a jitter measurment, taken with the sampling oscilloscope, is shown in Figure 3.13 and a schematic diagram explaining the content of this screenshot is shown in Figure 3.14. The micro-pulse jitter did not vary for micro-pulses at the start, middle and end of the macro-pulse, indicating that the passage of the micro-pulse through the slave laser has a negligible effect on the timing jitter.

3.6.4 Bandwidth control

An important aspect of the guide star laser system design is the ability to control the laser's spectral width and to accurately match the spectral width to the Doppler-broadened linewidth of atmospheric sodium. This ensures that all the sodium atoms participate in the fluorescence for maximum brightness of the artificial star. To achieve this, it was proposed to control the micro-pulse width, so that the Fourier transform of the micro-pulse temporal shape gives the desired frequency bandwidth. Section 3.4 demonstrated that the seed pulse source can produce low energy seed pulses with an adjustable width ranging from 0.4 ns to 1.0 ns and in this section, it is shown that when the slave laser is injection-mode-locked with these seed pulses, the bandwidth of the high energy output of

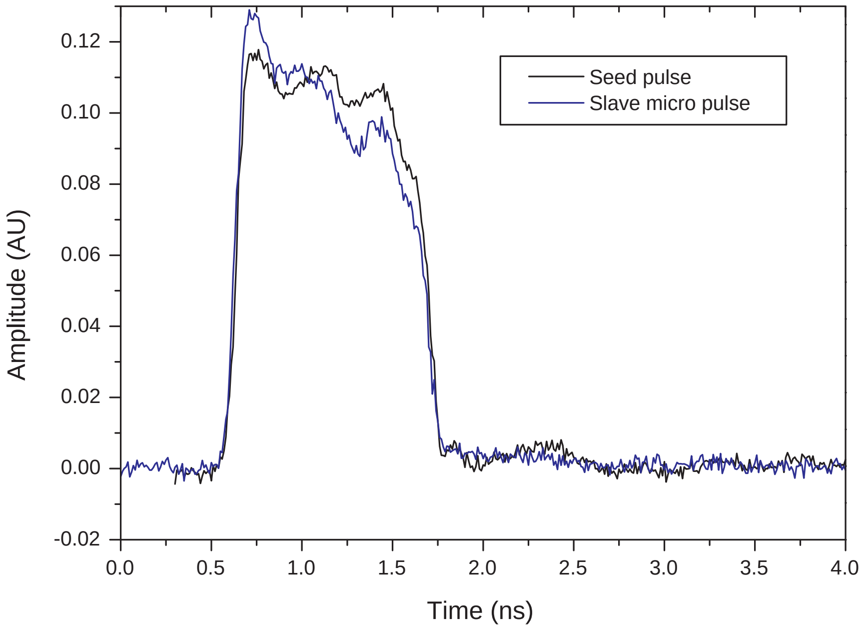

Figure 3.12: A comparison of an injected seed pulse and an output micro-pulse from the injection mode-locked slave laser. Both traces were taken with the same photodiode and sampling oscilloscope and are averaged over several seconds (the sampling oscilloscope cannot measure in real time).

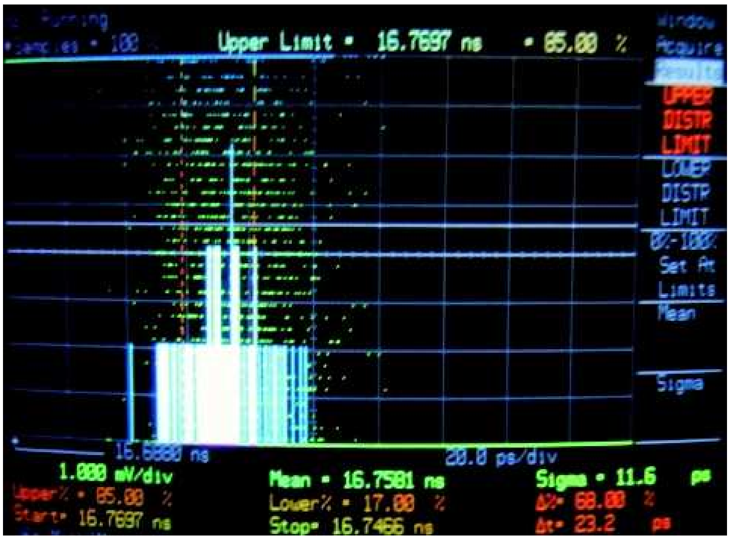

Upper Limit = 16.7697 ns = 65.00 %
16.6880 ns
20.0 ps/div
1.000 mV/div
Mean = 16.7581 ns
Sigma = 11.6 ps
Upper% = 65.00 %
Lower% = 17.00 %
Δ% = 68.00 %
Start= 16.7697 ns
Stop= 16.7466 ns
Δt= 23.2 ps

Figure 3.13: Measurement of timing jitter made with a 20 GHz sampling oscilloscope. The geen dots are sample points from the front edge of a micropulse (the fast photodiode used gives a negative output) and the white lines show a histogram of the sample point distribution. The rms jitter is 11.6 ps.

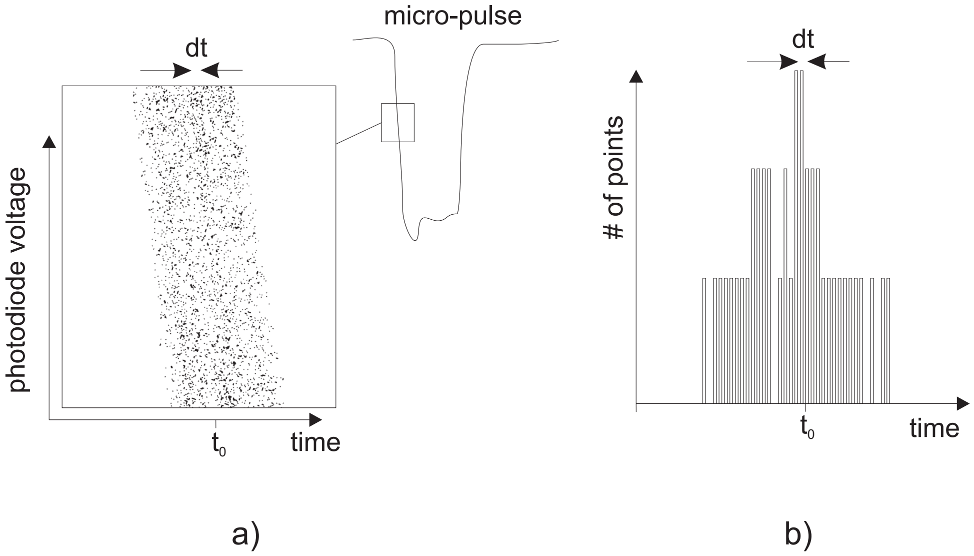

Figure 3.14: These sketches have been included to explain the information contained in Figure 3.13. Part a) shows a micro-pulse from the output of the slave laser and an expanded view of the sample points in the leading edge of this micro-pulse. These sample points are the green dots in Figure 3.13. The width of this line is representative of the timing jitter of micro-pulses. Part b) is a histogram showing the number of sample points that arive in each time interval *dt*. The histogram is shown as the white lines in Figure 3.13 and is used to calculate the rms jitter.

the slave laser can be controlled.

To measure the laser's bandwidth, the injection mode-locked pulse burst waveform from the slave laser was passed through a commercial spherical-mirror scanning Fabry-Perot interferometer (FP). The free spectral range (FSR) of this device was 10 GHz (mirror separation 7.5 mm, $FSR = \frac{C}{4d}$). The resolution was measured by recording the FWHM of the transmission peak from a cw, single frequency NPRO beam and was found to be 40 MHz. The 40 MHz transmission peak and the 10 GHz FSR are displayed schematically in Figure 3.15. One of the FP mirrors is mounted on a piezoelectric actuator which allows the FP mirror separation to be varied, thereby providing tunability of the FP transmission peak by adjusting the voltage on the piezo. For the bandwidth measurements, a saw-tooth voltage was applied to the piezo as shown in the upper part of Figure 3.15. This scanned the transmission peak over one FSR (10 GHz) every 93 ms. The slave laser output is pulsed with a repetition rate of 50 Hz (20 ms period). Whenever the FP transmission is tuned to coincide with part of the laser's spectrum, and a laser pulse is incident, a pulse of laser light will be transmitted through the FP with amplitude proportional to the fraction of laser power at the FP transmission frequency. The throughput of the FP was recorded with a photodiode and a digital oscilloscope set to integrate the throughput pulses. Over a period of a few seconds, the shape of the laser's spectrum became visible, providing the images of Figure 3.16. This figure shows the injection mode-locked laser spectrum for input seed pulse widths ranging from 0.57 - 1.02 ns. The laser bandwidth was taken as the FWHM of a Gaussian fit to the pictures.

Figure 3.17 summarizes the results of the measurements and shows the laser's bandwidth plotted against the seed pulse width. This result shows that the laser's bandwidth can be controlled by adjusting the seed pulse width and that the bandwidth was adjusted over the range of 0.8 GHz - 2.3 GHz. The bandwidth of the final SFG is expected to be approximately twice that of the fundamental wavelengths [17] and the results obtained thus essentially satisfy the system requirements. For bandwidths lower than 0.8 GHz, a longer seed pulse would be required, which can be generated by driving the first PC in the pulse slicer with the 3 ns pulser, as is demonstrated later, in Section 7.4.6.

A fit to the curve of Figure 3.17 shows that the time bandwidth product of the laser is 0.91 indicating that the laser is essentially transform limited. For a theoretical Gaussian-shaped transform limited pulse, the value for the time-bandwidth product is 0.44 while for a rectangular "top-hat" pulse shape the time-bandwidth product is 0.9. The complicated structure of the real laser pulses (Figure 3.9) makes it difficult to determine what the minimum time-bandwidth product for this pulse shape would be, especially as the pulse profile changes shape slightly as the pulse is shortened.

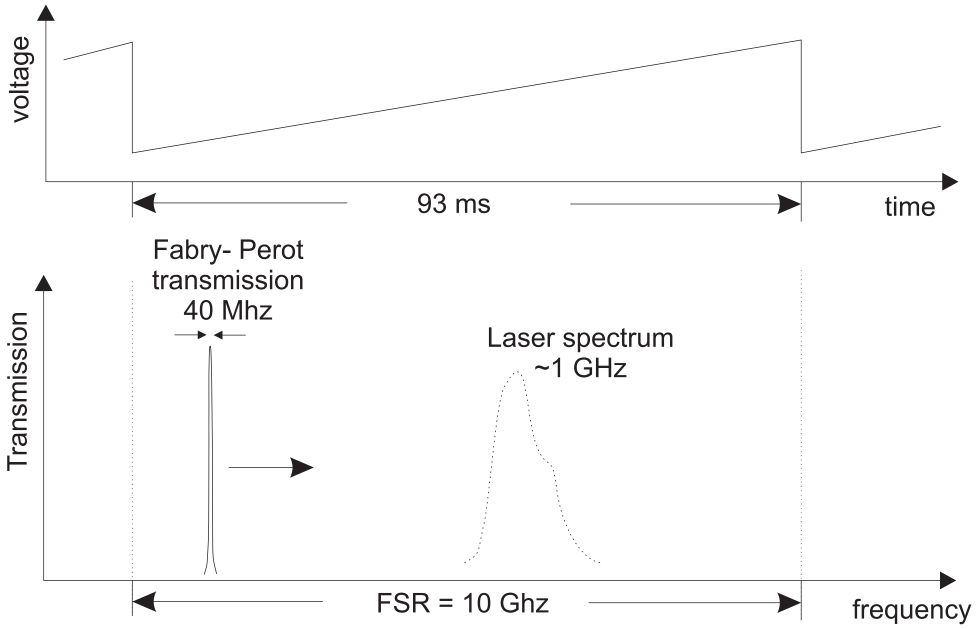

Figure 3.15: A schematic diagram showing the saw tooth voltage applied to the piezo on the Fabry Perot mirror (upper) and the FP transmission (lower). The transmission of the FP is scanned repeatedly over the free spectral range (FSR) to build up the outline of the laser spectrum.

With this spectrum measurement technique it was not possible to record the spectrum of individual pulses; the spectra shown in Figure 3.16 are made up from the integration of many macro-pulses. It is, however, expected that the measurements in Figure 3.16 are representative of the spectrum of each individual macro-pulse, as measurements of the temporal pulse shape, such as Figure 3.12, did not show evidence of pulse to pulse variations in the temporal shape of macro/micro pulses (Figure 3.12 shows a trace from a sampling oscilloscope which builds up from sample points taken from multiple macro-pulses. If there were pulse to pulse shape variations, the lines of this trace would show more scatter and the features would be blurred).

3.7 Discussion and conclusions

This chapter presented the design and performance of a proof of principle 1064 nm injection mode-locked laser. Many key concepts of the guide star design were demonstrated in this section, in particular, it was demonstrated for the first time, that injection mode-locking combined with Q-switching, can be successfully applied to Nd:YAG to produce a burst of of short duration micro-pulses in a Q-switched macro-pulse, while simultaneously maintaining control of the laser's bandwidth. The laser's bandwidth was controlled

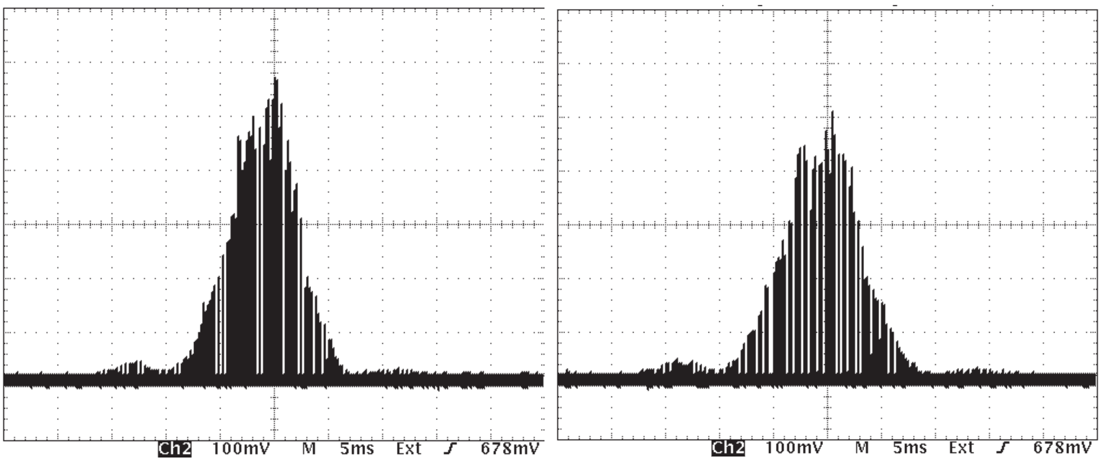

(a) 0.83 GHz

(b) 0.97 GHz

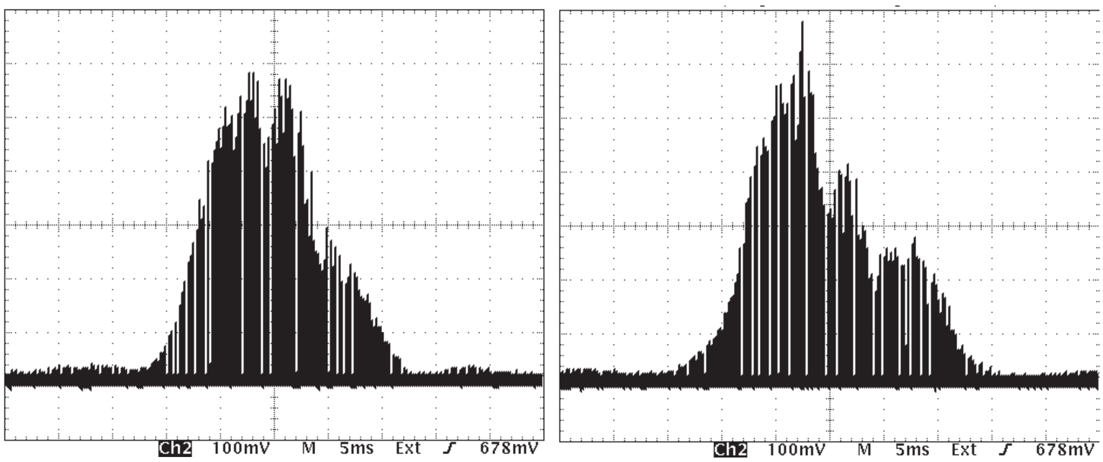

(c) 1.3 GHz

(d) 1.6 GHz

Figure 3.16: Macro-pulse spectra measured with a scanning Fabry-Perot interferometer with one horizontal division equal to 540 MHz. The micro-pulse widths for these pictures are (a) 1.02 ns, (b) 0.93 ns, (c) 0.76 ns and (d) 0.57 ns

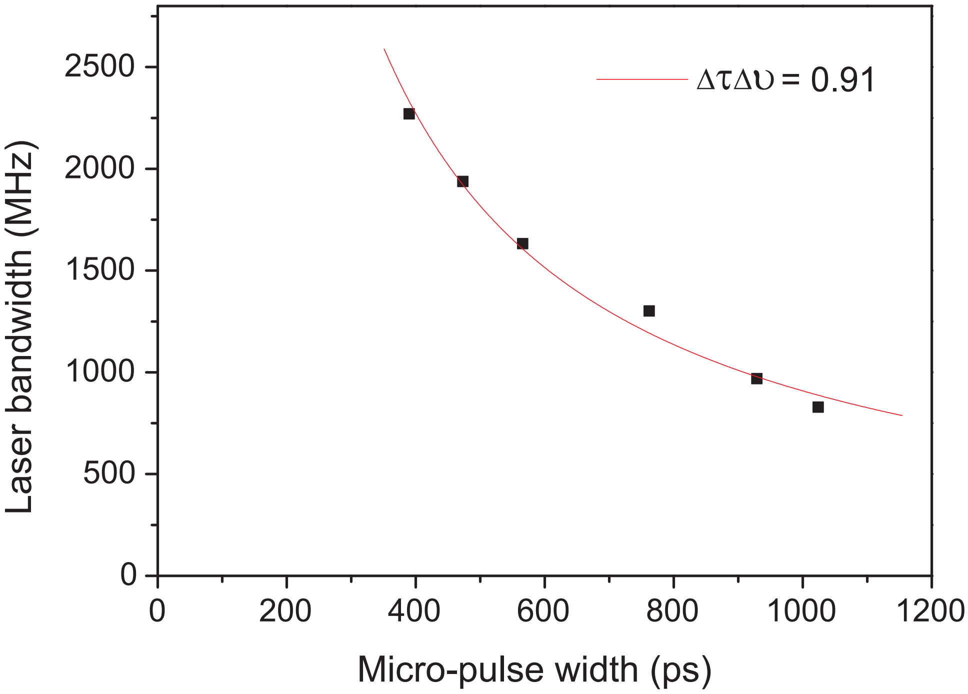

Figure 3.17: Plot of measurements of slave laser bandwidth versus the width of the seed pulse. The curve is a fit to the data with a time-bandwidth product of 0.91 as shown.

over a useful range of 0.8 - 2.3 GHz and the laser micro-pulses were shown to have very low timing jitter, an important requirement for efficient SFG. Furthermore, resonator design concepts such as dynamic stability and intracavity telescopes were trialed in this experiment and found to be practical and useful for a power-scaled version of this laser.

Chapter 4

Q-switched pulse stretching

4.1 Introduction

[1]Conventional Q-switched solid state lasers, that have a constant out-coupling fraction, produce pulses that have typical durations of 10-100 ns. For the guide star laser, it is necessary to have longer duration pulses (1-3 μs) to reduce the effects of bleaching in the sodium layer [89]. More generally, long pulses are also required for other applications including coherent laser radar systems to increase the single-shot velocity resolution.

The sum frequency macro-micro pulsed guide star laser would additionally benefit from long-duration pulse envelopes having near flat-tops. This would enable improved conversion efficiency by allowing a tighter focus within the nonlinear crystal, giving a higher peak power over the whole pulse duration and improved sum-frequency efficiency, while still remaining below damage threshold. A flat-topped pulse source will also allow more uniform bleaching and thus more efficient Na return.

One way to increase the duration of Q-switched pulses is to increase the resonator length [49], but this approach is not always practical, is limited by the mechanical stability of the resonator and the dynamic stability of the laser mode in high power lasers with varying thermal effects [78]. Other techniques for increasing or stretching the duration of Q-switched pulses have been reported, including using intra-cavity non-linear absorbers [90] [91] or second harmonic generation [92] to limit the intra-cavity peak power and thus slow the development of the giant pulse. Pulse stretching by discarding power from the resonator has also been demonstrated [46] [47] [93] [48]. While pulse durations of up to 1 μs have been achieved, the pulse energy decreased by as much as a factor of 4 when compared with an un-stretched Q-switched pulse at the same pump energy. In

---

[1] Much of the material contained in this chapter was also written up as a paper which can be found in Appendix A

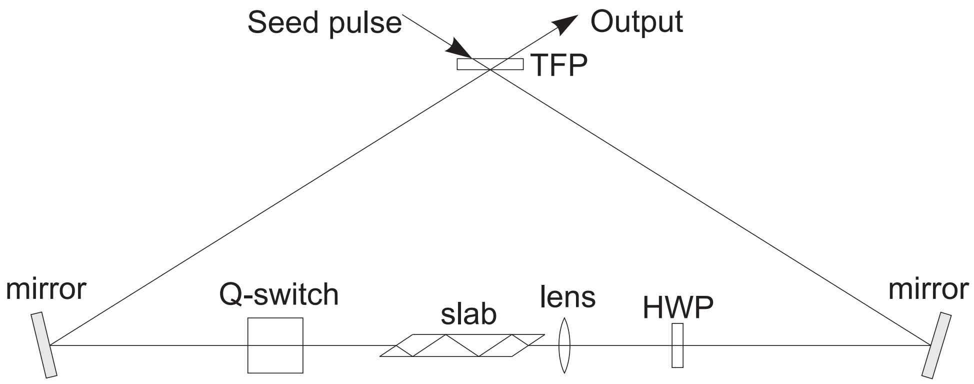

Figure 4.1: The ring resonator used for pulse stretching experiments. The round trip length is 4.2 m.

theory, more efficient pulse stretching can be achieved by using the modulated loss as the laser output [93]. Pulse stretching factors of 7-10 have been demonstrated [93], with a maximum duration of 650 ns and a flatness of 7 % for 500 ns pulses, but the difference in energy between stretched and unstretched pulses was not reported. Using the polarizer as the out coupler in a standing-wave laser significantly complicates injection seeding of the Q-switched laser, as the giant pulse travels back towards the master laser, requiring large amounts of optical isolation to prevent destabilization and potential damage of the master laser.

In this chapter, a new pulse stretching technique is described and demonstrated, which uses the novel ring resonator of Chapter 3 and a throttled Pockels cell Q-switch to produce flat-topped Q-switched pulses stretched by a factor of 4.5, without any reduction in pulse energy. The chapter is structured as follows: Firstly, a description of the experimental set-up is presented in Section 4.2, then a numerical model is described which predicts the shape and energy of laser pulses for different Q-switch drive waveforms. Section 4.4 describes the electrical circuit which produces the high voltage pulses used to drive the Q-switch then in Section 4.5, experimental measurements are presented which show the successful production of long duration, flat-topped Q-switched laser pulses.

4.2 Experimental set-up

For the pulse stretching experiments detailed in this chapter, a ring resonator without intra-cavity telescopes was used as shown in Figure 4.1. General telescope needs were satisfied with a single 2 m lens in this design.

For this resonator, the TFP acts as a polarization dependent output coupler as it transmits (outcouples) all π-polarized light and reflects all σ-polarized light incident upon it. The voltage on the Q-switch controls the amount of π-polarized light outcoupled on each round trip. With this configuration, the outcoupling fraction can be changed rapidly by adjusting the voltage on the Q-switch which in turn controls the round trip gain of the laser, G, according to[2]

$$G = (1 - l_{oc})e^{g_0 l} \tag{4.1}$$

where l_{oc} is the outcoupling fraction determined by the Q-switch and is given by

$$l_{oc} = \sin^2\left(\frac{\pi}{2}\frac{V}{V_{HW}}\right) \tag{4.2}$$

for which V is the voltage applied to the Q-switch, and V_{HW} is the Q-switch half-wave voltage.

If a suitable Q-switch drive waveform is applied, the round trip gain can be controlled to slowly release the energy stored in the gain medium and produce long-duration output pulses. Moreover, since there are no losses introduced using this technique, high efficiencies are possible. It is important to note that our technique does not involve the storage of large amounts of optical power within the resonator, then the subsequent slow release of this power using the outcoupler. Approaches using such methods tend to be inefficient due to the cumulative effect of the repeated round trips of large amounts of optical energy through the Q-switched resonator having typical round trip losses of 5-10 %. In contrast, with our technique, the pulse energy remains stored inside the laser gain medium and the Q-switch voltage waveform is used to control the round trip emission rate from the gain and thereby slowly releasing the stored energy from the gain medium.

A KD*P Q-switch was used for the initial experiments of Chapter 3 since it was available from a previous project, but for the pulse stretching experiments reported here a BBO cell was used to take advantage of the low piezo electric ringing in this material [80]. The presence of piezo-electric ringing makes the polarization rotation of the Q-switch harder to control and the pulse stretching more difficult, as the voltage applied to the Q-switch does not independently determine the out-coupling fraction. Measurements of the piezo-electric ringing in the KD*P cell is shown in Figure 4.2(a), which shows an optical pulse sliced out of a cw beam by the Q-switch placed between crossed polarizers. As can be seen, an oscillation is present in this waveform, even though the drive pulse applied to the Q-switch had a flat top. Figure 4.2(b) shows the response of the BBO cell, also driven by a flat-topped drive pulse, and shows little piezo-electric ringing.

Unfortunately, BBO has a large half wave voltage of around 8 kV for a dual-crystal cell at 1064 nm, which complicates the drive electronics, but this difficulty can be overcome,

---

[2] This formula ignores other sources of loss such as scatter, absorption etc. They can be included by adding a loss term to the multiplication factor $(1 - l_{oc})$ in Equation 4.1.

as is demonstrated later in the chapter.

4.3 Numerical modelling of pulse stretching

Lowdermilk and Murray [94] have presented a numerical model for calculating the build up of pulse fluence in a cavity-dumped regenerative amplifier that is seeded by a short optical pulse. The model assumes a uniform gain distribution and a top-hat pulse but has also been shown to accurately describe the performance of resonators with Gaussian beam profiles [43]. We have adapted this model to describe pulses stretching in an injection mode-locked Q-switched laser.

In their analysis, Lowdermilk and Murray begin with Maxwell's wave equation describing the optical electric field and a Schroedinger-like equation for the polarization and population inversion within the gain medium, then by applying the aforementioned approximations and other generalizations typical of solid state laser systems, they arrive at a pair of recurrence equations that describe the build up of pulse fluence in the laser cavity. In these equations, the intra-cavity pulse fluence, J_k, and small signal gain, g_k, after k passes of the seed pulse around the laser amplifier are related by [94]

$$J_{k+1} = T J_s \ln\{G_k[\exp(J_k)/J_s) - 1] + 1\} \tag{4.3}$$

$$g_{k+1} = g_k - \Delta J_k / 2J_s \tag{4.4}$$

where

$$G_k = \exp(g_k) \tag{4.5}$$

$$\Delta J_k = J_{k+1} T^{-1} - J_k \tag{4.6}$$

J_s is the saturation fluence and T is the energy transmission coefficient for one pass of the amplifier, including both loss and out-coupling. These equations have been used to model our pulse-stretched, injection mode-locked ring laser, by including a variable term in the round trip transmission:

$$T = 1 - l - l_{oc} \tag{4.7}$$

where l is the fixed round trip loss due to scatter, absorption, misalignment and beam clipping at apertures. l_{oc} is the out-coupling fraction:

$$l_{oc} = 1 - \sin^2\left(\frac{\pi}{2}\frac{V_k}{V_{HW}}\right) \tag{4.8}$$

where V_k is the voltage applied to the Q-switch for pass k, and V_{HW} is the Q-switch half-wave voltage.

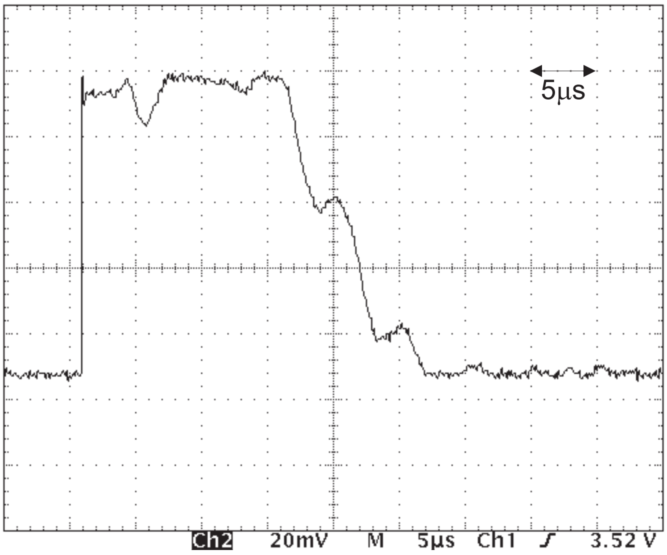

(a) KD*P

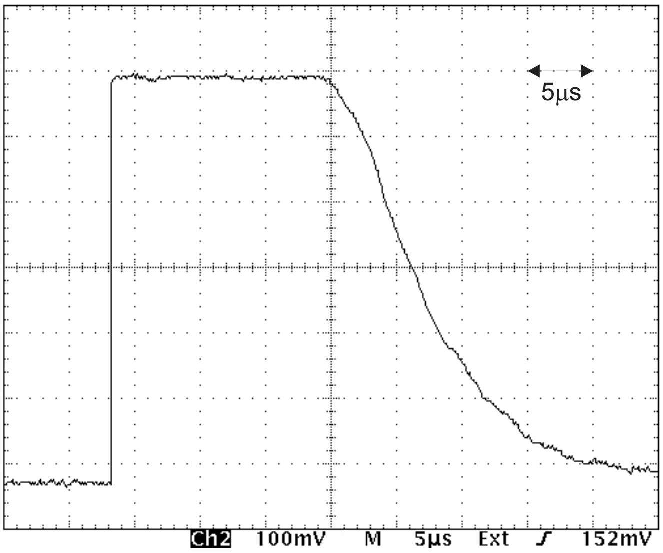

(b) BBO

Figure 4.2: Optical pulses sliced out of a cw beam by a (a) KD*P and (b) BBO Q-switch, placed between crossed polarizers, driven by a 10 ns rise-time, flat-topped drive pulse. The oscillation present in (a) shows evidence of piezo-electric ringing in the KD*P cell.

The output pulse energy is given by

$$E = \sum_k E_k = \sum_k J_k A l_{oc} \tag{4.9}$$

where E_k is the energy out-coupled after each pass and A is the cross-sectional area of the laser mode in the gain medium.

For our analysis, we used an injected pulse energy of 3×10^{-10} J and saturation fluence $J_s = 0.66$ J/cm^2 [61]. The values of l, A and g_0 were determined by measuring the energy and duration of the injection-mode-locked macro pulse for conventional Q-switching and adjusting the parameters to yield the best agreement. The measurements and model prediction for different pump levels are shown in Figure 4.3. For each pump level, the voltage was adjusted to provide the maximum pulse energy in both the simulated and measured data. This procedure resulted in $g_0 = 0.31$ for the pump energy used to produce the 10 mJ output pulse. Values of l and A were used that were consistent with values expected for the resonator (see Appendix D) and produced good agreement between theoretical and measured results (Figure 4.3). The values were $l = 5.0$ % for the round trip loss and $A = 5.5$ mm^2 for the beam area. These parameters were then used for all subsequent modelling of the effect of variable outcoupling on the macro-pulse envelope.

The model predicts that Q-switching the injection mode-locked laser using the optimum, constant out-coupling at the highest pulse energy in Figure 4.3 yields a macro pulse duration and energy of 0.41 μs and 10.0 mJ. By shaping the Q-switch voltage waveform, the outcoupling fraction is changed and can be used to modulate the optical pulse shape and stretch the duration. The model was used to investigate the effect of different waveforms and to determine a waveform that produces long duration flat-topped pulses. Another requirement is that the waveform must have a shape that can be produced experimentally using a reliable high voltage circuit. Hence waveforms having exponential shapes were preferentially modelled as these shapes can be easily produced with long lifetime transistor switches and capacitor-resistor networks, as we shall see in the following section.

The first Q-switch voltage waveform to be trialled was one having a single step-exponential fall as shown schematically in Figure 4.4. Initially, half wave voltage is applied to the Q-switch, allowing the giant pulse to build up rapidly with no outcoupling. Then the outcoupling is increased sharply by reducing the Q-switch voltage (point $t1$ in Figure 4.4) to arrest the build up of the giant pulse and output part of the pulse, then an exponential rise in Q-switch voltage reduces the outcoupling fraction of the resonator. Part of this voltage waveform is displayed in Figure 4.5 along with the model prediction of the laser output for this voltage pulse.

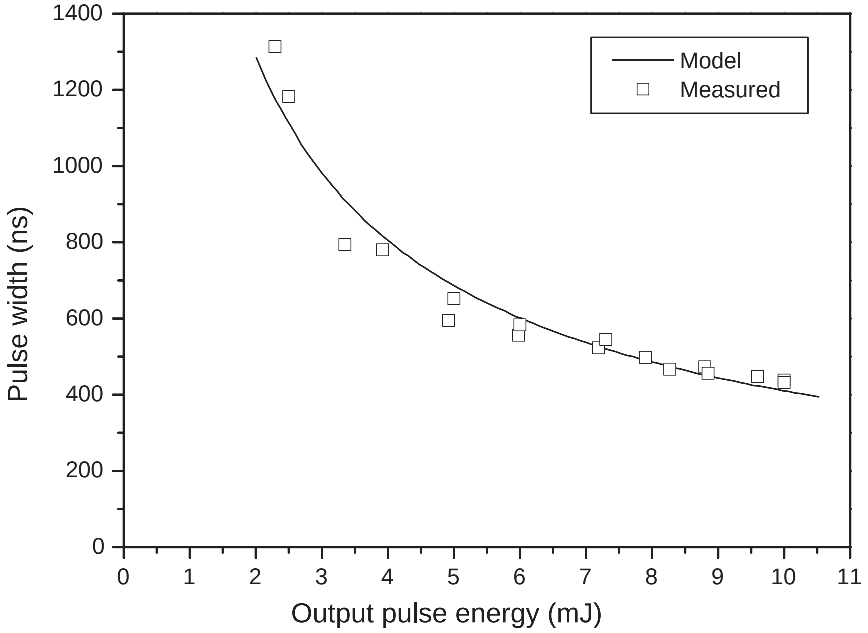

Figure 4.3: Measured FWHM macro pulse duration plotted against the slaves injection mode-locked output energy for various pump levels. At each pump level, the Q-switch voltage was adjusted to maximise the pulse energy. The solid line shows the prediction of the numerical model for the best fit parameters.

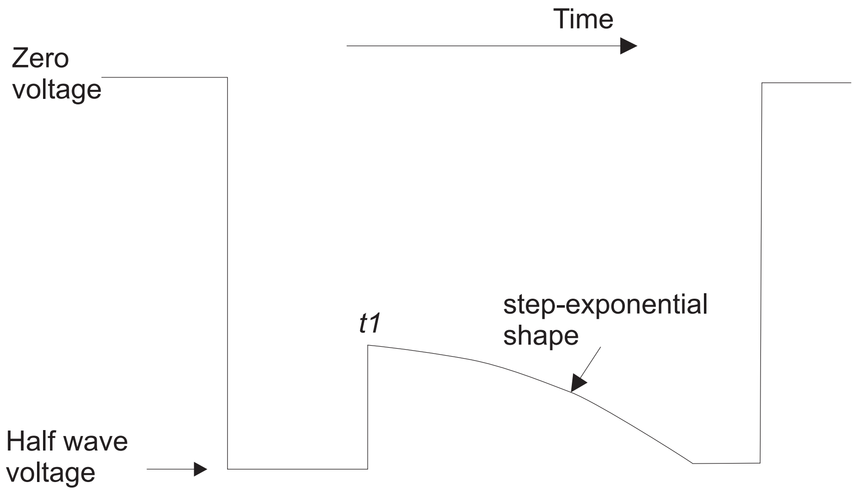

Figure 4.4: A sketch showing the overall shape of the Q-switch voltage waveform modelled in these experiments. This waveform has a single step exponential change in voltage for pulse stretching.

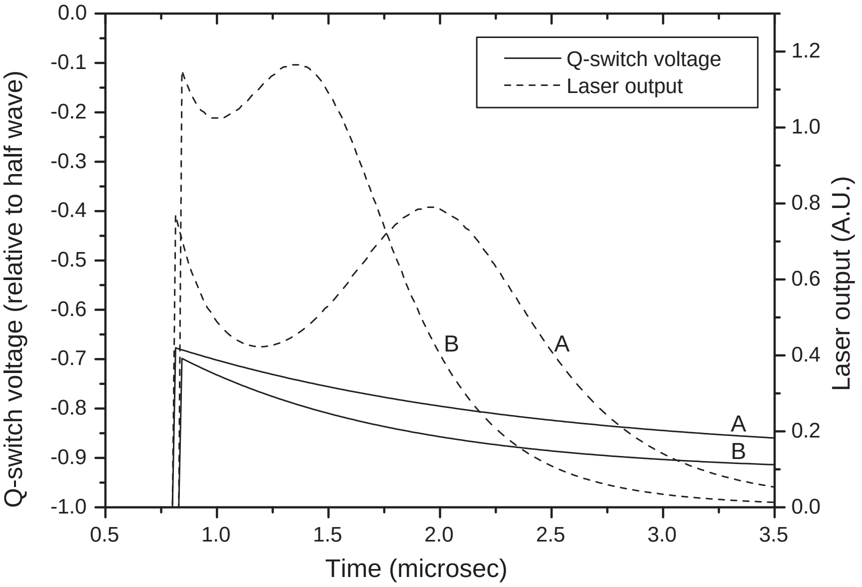

Figure 4.5: Two Q-switch voltage waveforms, A and B, with the macro pulse envelopes predicted by the numerical model using best-fit laser parameters determined using the measurements in figure 4.3. The Q-switch is switched from high loss (Q-switch voltage = 0) to low loss(Q-switch voltage = -1) at Time = 0.

In Figure 4.5 *A*), a slowly falling exponential waveform is modelled. With this waveform, the laser pulse width was increased to 1.71 μs, with an energy decrease of 8 % to 9.22 mJ and a pulse flatness of < ± 25 %. In Figure 4.5 *B*) the initial outcoupling fraction is reduced to prevent the excessive suppression of the giant pulse. This improves flatness to < ± 6 % and pulse energy to 9.71 mJ (a drop of only 3 %) but results in a pulse duration of 1.01 μs.

These examples illustrate the general behaviour of the macro-pulse for Q-switch voltage waveforms of this type, which have a single exponential increase in Q-switch voltage: using this approach it is not possible to stretch the duration by more than about twice that of a constant out-coupling pulse while maintaining a flat-top.

A double-exponential voltage waveform can better satisfy both requirements as shown in Figure 4.6. The predicted duration and energy of the stretched pulse is 1.73 μs and 9.65 mJ, a 420 % increase and a decrease of only 3.5 % respectively compared to the constant out-coupling pulse, which is also plotted in Figure 4.6. Adding a third exponential to decrease the out-coupling faster when the pulse intensity starts to decrease, at about Time = 2 μs in this example, would further stretch the pulse.

The recursive equations 4.3 and 4.4 that were used in this model to describe the

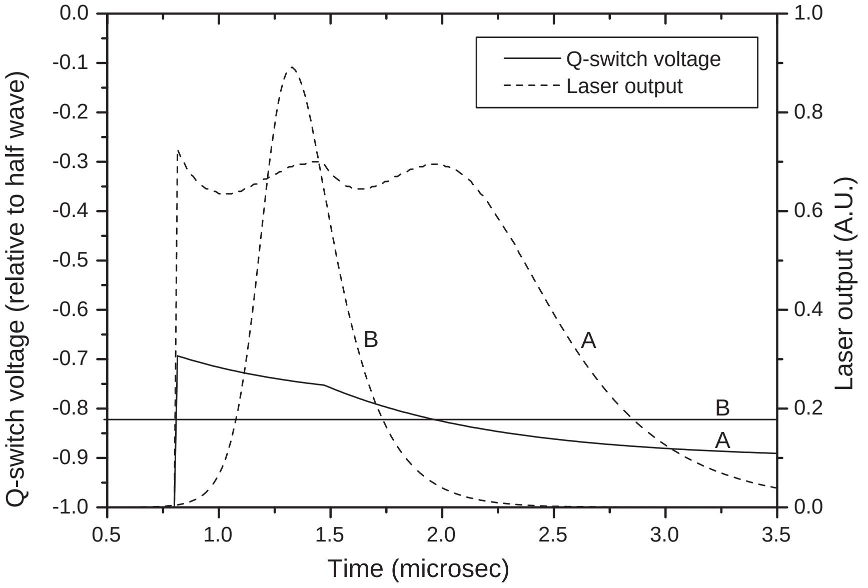

Figure 4.6: (A) Optimised Q-switch voltage waveform and predicted stretched macro pulse envelope. (B) Constant out-coupling Q-switch voltage and predicted envelope. Note that the B envelope has been divided by 3 to facilitate plotting. Both predictions use the best-fit laser parameters determined from the measurements in figure 4.3.

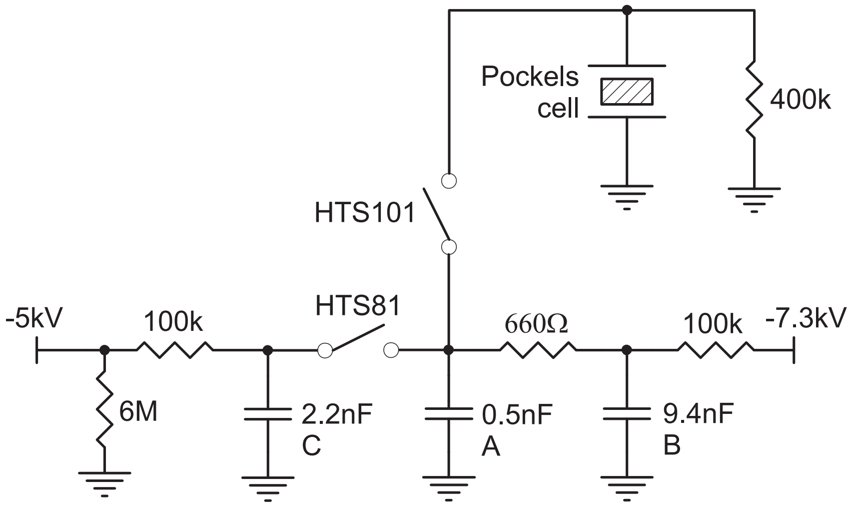

Figure 4.7: Electrical circuit used to drive the Q-switch. It uses two high voltage switches, HTS 101 and HTS81, two high voltage power supplies, and a combination of resistors and capacitors to produce the required waveform. The Pockels cell has a nominal capacitance of 4 pF.

pulse fluence and gain inside the resonator have been shown to reduce exactly to the rate equations describing the photon density and population inversion in a regular Q-switched oscillator (not injection mode-locked) for the case when changes in pulse fluence and gain on successive round trips is small [94]. This indicates that the pulse stretching model described in this section is not limited to injection mode-locked Q-switched systems, but is also applicable more generally to injection seeded Q-switched systems that have low gain.

4.4 Q-switch driver

The circuit used to produce the shaped Q-switch voltage is shown in Figure 4.7 and its output voltage as a function of time is shown in Figure 4.8. It uses two high voltage MOSFET switches that can switch voltages of 10 kV (Behlke HTS101) and 8 kV (Behlke HTS81) with a switching time of around 10 ns. We chose to use MOSFET switches rather than kryotrons or planar triodes, which were used in previous pulse stretching circuits [46] [47] [93], as we required a circuit that could operate at a pulse repetition frequency of 800 Hz for long periods, and contained modern all solid state switches.

Initially, both the switches are open, and two independent high voltage power supplies charge capacitors A, B and C. At the end of the laser pump pulse, the HTS101 switch is closed, applying the near half-wave voltage of -7.3 kV to the Q-switch. A voltage less

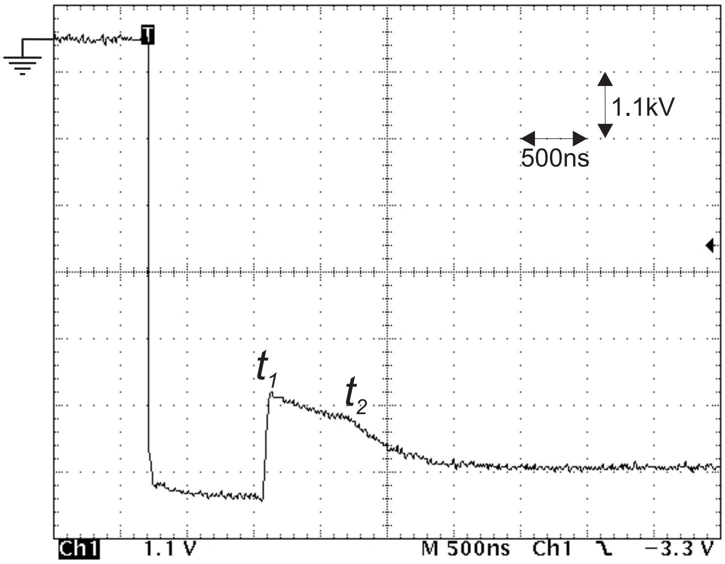

Figure 4.8: Q-switch drive pulse used for pulse stretching, produced by the circuit in Fig. 6. The symbols t_1 and t_2 denote the times at which (1) the fast decrease in Q-switch voltage, and (2) the change in the exponential time constant occur.

than the half-wave voltage (-7.8 kV) was used so that a small amount of the intra-cavity power was out-coupled, thereby limiting the intra-cavity power and thus reducing the risk of damage to optics. At time t_1, the laser pulse has built-up sufficiently and the HTS81 switch is closed, rapidly discharging capacitor A and producing a fast decrease in the voltage on the Q-switch. The charge on capacitor B then flows onto capacitors A and C, increasing the voltage with a time constant set by the 660 Ω resistor and the parallel combination of capacitors A and C. At time t_2, the HTS81 switch is re-opened, which increases the rate of charging of capacitor A.

4.5 Results

A typical measurement of the stretched macro-micro pulse and the Q-switch drive is shown in Figure 4.9. The laser pulse energy is 10 mJ and the FWHM pulse duration is 1.8 μs. The transition from low out-coupling to high out-coupling (t_1 in Figure 4.8) and the time at which the change of the exponential time constant occurs (t_2 in Figure 4.8) were both adjusted to optimize the flatness of the pulse. For the laser used in this measurement, the flatness of the pulse envelope varied by less than ±5 % over a period of 1 hour. Optimisation of the pulse flatness maximised the macro-pulse energy and yielded an energy that was the same, to within a 1 % measurement error, as that of the un-stretched pulse.

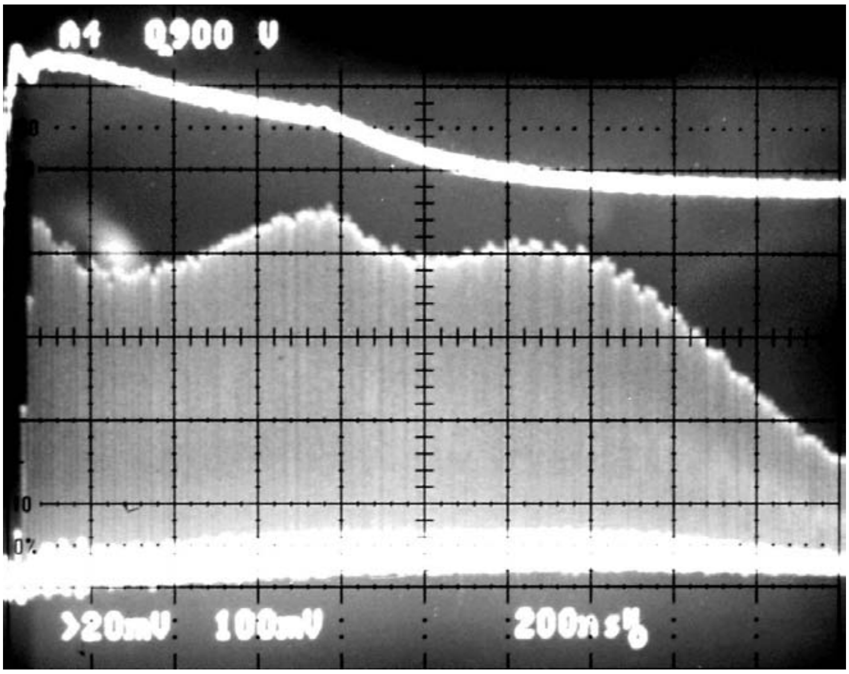

Figure 4.9: A 10 mJ, injection mode-locked, stretched laser pulse (lower trace), produced using a Q-switch drive pulse similar to that of figure 4.8. The upper trace (0.8 kV/division) shows part of the Q-switch drive pulse. The un-stretched laser pulse in this case was similar to figure 3.10, with a pulse width of 0.43 μs and pulse energy of 10 mJ.

The timing of transition t_1 was the most critical parameter for optimising the flatness of the pulses, requiring a timing resolution of about 5 ns, about 0.5 % of the pulse build-up time or 35 % of the round-trip time. If this parameter was not set within these limits, irregular shaped pulses were produced. Other circuit parameters were found to be much less critical; the voltages applied to the circuit needed to be adjusted to within only 0.1 kV, and standard tolerance resistors and capacitors could be used.

Fluctuations in pump energy could also degrade the flatness of the macro-pulse. The predicted dependence of the pulse envelope on small signal gain is plotted in Figure 4.10. A 1 % change in gain significantly degrades the pulse flatness but has approximately no effect on the laser efficiency. The change in pump energy could be compensated by moving transition t_1 earlier (for curve C) or later (for curve B) by one round trip (the minimum temporal resolution for the numerical model). The timing of this transition could be controlled by monitoring the onset of the giant pulse during the pre-lase and using a comparator circuit to set the time at which the transition t_1 occurs [93].

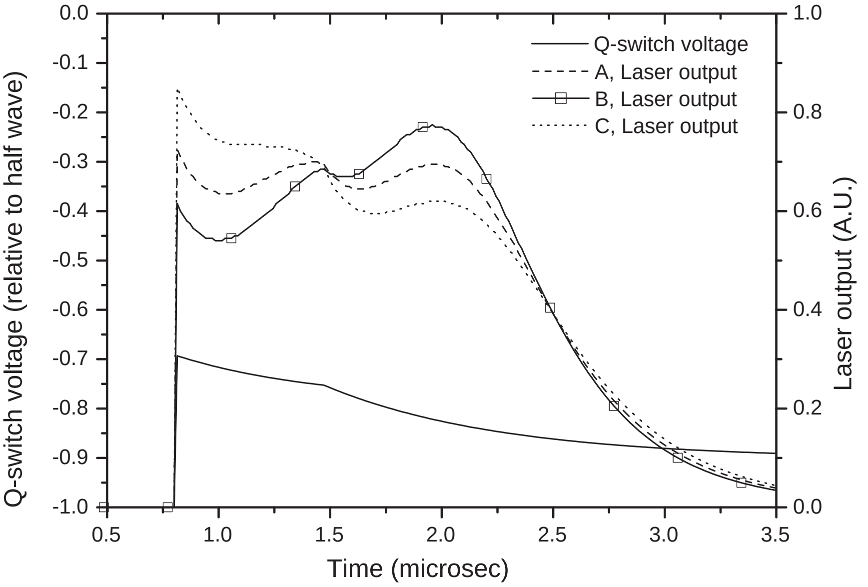

Figure 4.10: Plots of the modelled macro-pulse envelope for small signal gain that (A) is the value for which the Q-switch waveform was optimised, (B) is 1 % less than the optimum, and (C) is 1 % larger than the optimum. These results were confirmed qualitatively during experiments.

4.6 Discussion and conclusions

This chapter presented a new and simple technique for efficiently stretching the duration of Q-switched laser pulses. The work reported here was applied to an injection mode-locked Nd:YAG laser for guide star applications, but is also more generally applicable to other types of gain media and injection-seeded laser systems.

While the repetition rate used for these experiments was limited to 50 Hz by the laser head (Section 3.2), the high voltage switches, resistors and capacitors used in the drive circuit can run at repetition rates in excess of 800 Hz and are thus suitable for the final guide star design. It is not expected that the response of the laser to the Q-switch drive pulse is dependent on the repetition rate used.

Chapter 5

High power laser head design choice

5.1 Background

The Nd:YAG gain medium has been extensively researched and has received wide-spread use and popularity owing to its high emission cross section, good thermal conductivity, strong material properties and mature technology (crystals, coatings, diode lasers etc) [61]. Consequently, a multitude of Nd:YAG laser head designs have been reported in the literature. Designs range from the popular rod geometries [76] to thin disc [95], microchip [96] and slab lasers [97][74][98], with each of these designs being further subdivided by the different pumping and cooling geometries implemented. It is usually the thermal effects in the laser gain medium, such as thermal birefringence and thermal lensing, which limit the power scalability of each design, with the choice of laser crystal configuration, pumping and cooling geometry being crucial to the performance of the laser.

5.2 Objective

The aim of this chapter is to describe the fundamental principles of a high power laser head design and to use these principles to formulate a design that may be suitable for the high power injection mode-locked guide star source. The chapter begins by listing the requirements imposed on the laser head by the guide star application in Section 5.3, then goes on to describe the thermal effects that limit the power scalability of different designs in Section 5.4. Rod and slab type designs are explored as possible candidates for the guide star source in Sections 5.5 and 5.6, before it is concluded that an edge-pumped slab design would be suitable.

5.3 Laser head requirements

For an injection mode locked guide star source, the choice of laser head architecture is narrowed considerably by the following requirements:

- An average power of approximately 10 W (or greater) is required in a 1064 nm diffraction limited, polarized beam. The exact power required depends on the power scaling architecture adopted. For a system of five 10 W oscillators around 10 W at 1064 nm is required, depending on the conversion efficiency of the SFG stage. For a MOPA system, less power is required. In general, the more power the better.

- The amount of thermal lensing present should be controllable when using a long-length ring resonator (this is particularly important if the thermal lensing is astigmatic, such as in slab lasers, and the laser cannot be made stable in both the x and y-directions).

- The laser must have a stable resonator to allow polarization outcoupling for pulse stretching (Chapter 4). This eliminates designs such as the Innoslab design [98].

- The laser must be robust and able to operate for long periods without maintenance. At the observatory, the laser will be expected to operate at 800 Hz, 10 h/day, for approximately 150 day/year between maintenance intervals. This equates to around 1 G shot/year.

5.4 Thermal effects in high power lasers

The large pump powers required for high power lasers inevitably lead to significant heating of the laser gain medium. The transition from lamp pumped systems to laser diode based systems has significantly reduced the heat load due to direct pumping of the upper laser level. Heating of the crystal still occurs, however, primarily due to the energy difference between pump and laser photons (the quantum defect) which is transferred to heat through non-radiative transitions. For Nd:YAG, the quantum defect is

$$\frac{808nm}{1064nm} = 0.76 \tag{5.1}$$

and thus an absolute minimum of 25 % of the pump power is converted to heat.[1] Problems arise when there are temperature gradients in the gain medium caused by non-uniform

---

[1] Another source of heat is the non-radiative decay of excited electrons to the ground state. Nd:YAG has a 10 % branching ratio to non-radiative transitions, the other 90 % are for spontaneous emissions [61].

heating and surface cooling. This gives rise to phenomena such as thermal lensing and stress-induced thermal birefringence that limit the maximum power extractable from the gain medium. The challenge in designing a high power, diffraction limited laser is to implement pumping and cooling geometries to minimize the thermal gradients in the gain medium and to avoid the deleterious effects of thermal lensing and stress-induced thermal birefringence.

5.4.1 Thermal lensing

Thermal lensing occurs due to the temperature dependence of the refractive index of the gain material. For Nd:YAG [61],

$$\frac{\partial n}{\partial t} = 7.3 \times 10^{-6} K^{-1} \tag{5.2}$$

and a temperature gradient across the slab or rod aperture imposes a focal power to the passing wavefront. As an example, the end-pumped, dual rod, cw Nd:YAG laser system presented by Tidwell et al. [99] had a thermal lens of 12.9 cm for 235 W pump and 60 W output power.

In the case of a non-uniform thermal contact at the Nd:YAG/heatsink interface, or a non-uniform pump distribution, the non-uniform refractive index profile created will impose wavefront distortion on the laser mode, which will transfer power to higher order transverse modes of the resonator. This will degrade the beam quality and also introduce a loss mechanism for lasers designed for diffraction limited operation which use an intra-cavity aperture to allow only the TEM$_{00}$ mode to run with low loss. The higher order modes have a larger spatial extent and far-field divergence angle and so they will suffer large clipping losses at the intra-cavity aperture.

5.4.2 Thermal stress and thermal birefringence

Mechanical stresses arise in a laser crystal from the heated central region of the rod or slab being constrained from thermal expansion by the coolder outer surfaces in contact with a heat sink. While Nd:YAG has a low natural bi-refringence, the stresses that build up in a Nd:YAG crystal under a heat load result in stress-induced thermal birefringence, which can cause substantial polarization losses in polarized lasers. An example is presented by Uehara et al. [100] who described a cw 26.5 W linearly polarized, side pumped, rod laser for which the single pass de-polarization losses were 5.1 %. The amount of depolarization is dependent on the specific configuration of the laser head and resonator used.

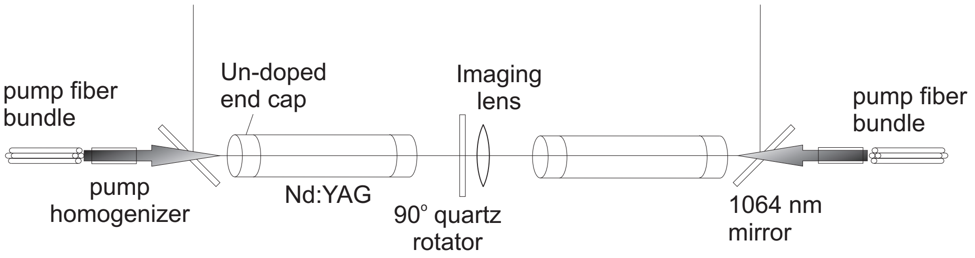

Figure 5.1: Schematic diagram of an end-pumped rod laser design [76]. This design uses two identical rods with an intermediate quartz rotator(QWP) to reverse the effects of thermal birefringence between each rod.

Care must also be taken to avoid temperature gradients and stresses at the ends and edges of the rod or slab, which are not in contact with a heat sink. Large gradients in these areas can cause surface bulging, introducing wavefront distortion on a passing mode, or even crystal fracture in the case of large pump densities. In some lasers, this can be avoided by bonding an un-doped end-cap, which does not absorb pump light and thus reduces the thermal stress at the end surface [76].

5.5 Rod lasers

Rod gain media are perhaps the most popular choice for commercial lasers as they are inexpensive to manufacture and can provide high laser powers with reasonably good beam quality. An advantage of rod-type lasers is their cylindrical symmetry, which allows thermal lensing to be easily compensated by using inexpensive spherical optics. Unfortunately, cooling the surface of the rod while heating the core leads to stress-induced thermal birefringence which usually limits the power in polarized rod lasers.

A good example of a rod laser is presented by Frede et al. [76] who have developed a 100 W cw diffraction limited Nd:YAG rod laser optimised for gravitational wave detectors. A schematic of this design is shown in Figure 5.1. The design uses two rods, with an intermediate quarter wave plate to reverse the thermal de-polarization effects when passing from one rod to the next. Each rod is end-pumped by fiber-coupled lasers diodes and uses a pump-homogenizer to provide an even pump distribution for improved beam quality. A composite rod with un-doped end-caps was used to reduce the surface stress caused by the high pump flux at these faces.

Fibre-couple laser diodes are, unfortunately, an expensive form of pump light and retail for at least double the price of similar-power laser diode arrays.

A successful variation of the rod architecture is the thin disc designs that have a disc

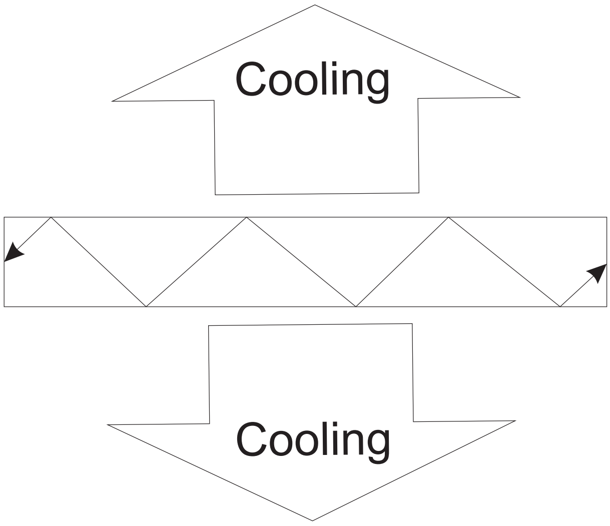

Figure 5.2: A schematic diagram of a laser slab with the plane of the zigzag path in the direction of the cooling. With this configuration, the thermal distortions caused by the cooling will be averaged out by the zigzag path.

of gain material bonded to a heat sink on one face [95]. The surface of the disc in contact with the heat sink is mirror coated to double-pass the laser beam through the gain on each round trip. These designs have achieved high average powers and good beam quality but require complex pumping geometries to focus the pump light through the narrow edge of the disc. Both rod and thin disc designs represent a major divergence from the proven research capabilities of our institution which has primarily focused it knowledge and skills base on the design of zigzag slab lasers, which will be discussed in the following section.

5.6 Slab lasers

The primary advantage of slab lasers is that they enable a zigzag path to be used inside the gain medium, which averages out the effects of thermal lensing and birefringence in the plane of the zigzag [61].

Ideally, the plane of the zigzag path should be in the direction of cooling, as this is usually the direction with maximal thermal gradient. Then, if the pumping arrangement is chosen to have minimal gradients in the orthogonal plane, low thermal distortions and high laser powers are possible. A zigzag slab design, with this cooling geometry is shown in Figure 5.2.

End-pumping is often cited as an effective way of providing a uniform pump distribution, as the long absorption length combined with multiple bounces of the pump light along the slab length provides an even pump profile [101]. This often requires complicated

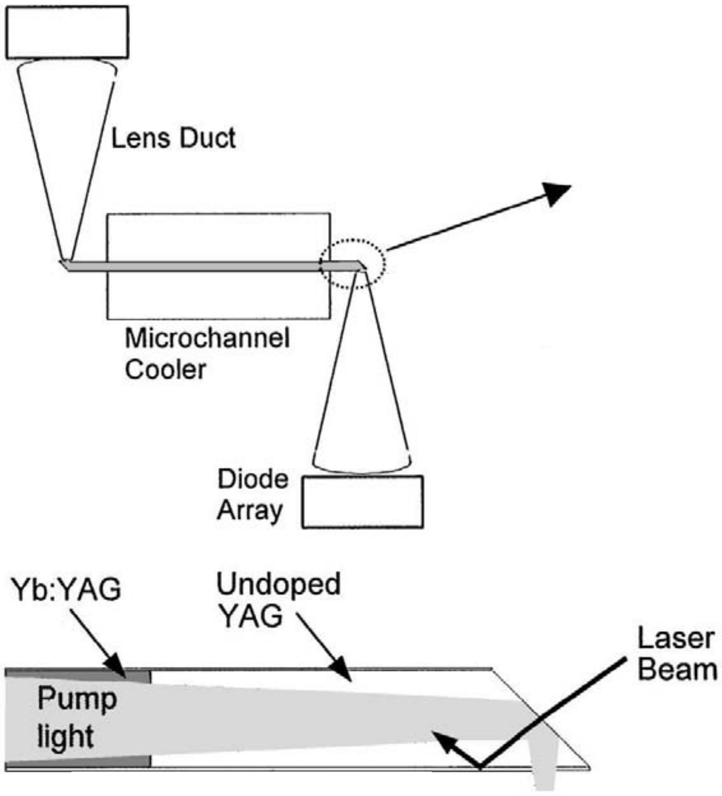

Figure 5.3: The end-pumped slab design described by Goodno et al. [97]. For this design, the pump light is reflected off the end faces of the slab. The laser mode takes a zigzag path in the direction of cooling, with the TIR at the cooled faces maintained by a thin layer of silicon dioxide.

transfer optics to condense the pump light from the pump source and focus it into the small aperture of the slab end face, however. An example of an end-pumped slab laser is presented by Goodno et al. [97] and is shown in Figure 5.3. This design uses a waveguide to focus and transfer the pump light from collimated laser diode arrays into the slab.

If the large-aperture faces on the sides of the slab are used as the pump windows, the pump transfer optics can be simplified, but the pump uniformity is decreased. An example of this slab design is the so-called "edge-pumped" laser described by Rutherford et al. [74], and is shown in Figure 5.4. For this design, a horizontal thermal gradient exists due to the exponential absorption of pump light from each side, but the measured thermal lens was found to be relatively weak, with f =420 mm at 300 W pump power. This laser produced 28 W of cw light with $M^2 = 1.5$ from 175 W pump [74].

Both of the designs illustrated in Figures 5.3 and 5.4 have de-coupled pump and cooling

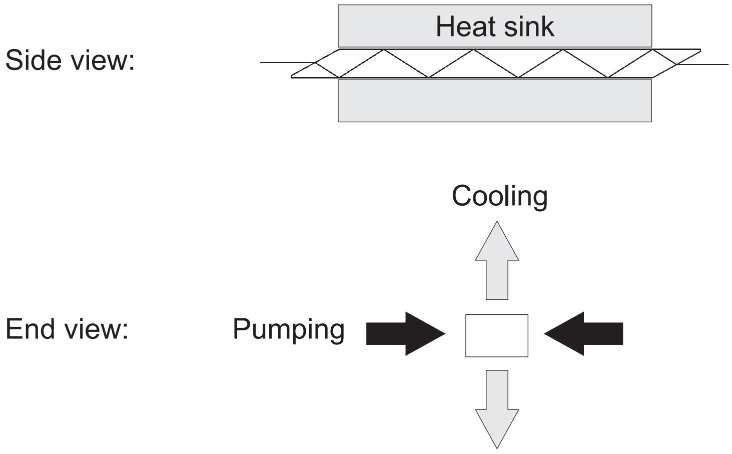

Figure 5.4: The edge-pumped laser head design of Rutherford et al. [74], showing a zigzag slab conduction cooled through top and bottom surfaces and pumped through the large aperture side faces.

faces which allows the slab to be conduction cooled. This provides increased reliability and simplified engineering when compared to designs that are water cooled and use the same surface for pumping and cooling [77][102]. Unfortunately, both the edge-pumped and end-pumped slab designs can suffer from parasitic oscillations, which arise from closed TIR mode paths being formed between the polished sides of the slab. To avoid this, both designs need to have one side wedged to destroy the TIR paths of the parasitic mode. This topic is treated in more detail in Section 6.3.4.

An additional advantage of the slab gain medium is that Brewster-angled entrance and exit faces can be used, removing the need for AR-coatings on these surfaces.

5.7 Design choice

To summarize, Table 5.1 presents a comparison of the advantages and disadvantage of the three laser head designs discussed.

A laser head design based on the edge-pumped architecture was selected for the high power guide star laser. This design has been shown to be scaleable to medium average powers and it offers significant simplifications in the pumping and cooling requirements over other slab and rod designs. In particular, the large pump windows, consisting of the whole side faces of the slab, enable a large pump flux to be easily directed into the slab without the need for complicated waveguides or focusing optics. Even though the original design presented by Rutherford et al. [74] used fibre-couple laser diodes to pump the slab, un-collimated diode arrays could also be used, given that the pump windows

	Laser head architecture		
	Rod [76]	TRW slab [97]	Edge-pumped slab [74]
Relatively inexpensive	✗	✗	✓
Simple waveguide	✓	✗	✓
Symmetric thermal lens	✓	✗	✗
No parasitic ocillations	✓	✗	✗
Low thermal bi-refringence	✗	✓	✓

Table 5.1: Advantages and disadvantages of three laser head designs that can potentially be used in the guide star system design.

are so large. This offers a significant cost saving as fast- and slow-axis collimated arrays are around 50 % more expensive than un-collimated arrays of the same power, and fibre coupled diode lasers are more than double the price [103].

The specifics of the edge-pumped slab design used for the high power slave laser are discussed in detail in the following chapter.

5.8 Conclusions

This chapter presented the design requirements for the high power guide star laser head. The dominant factor in the choice of laser head architecture is the management of thermal effects such as thermal lensing and thermal birefringence, with the pumping and cooling geometries selected to avoid uncontrolled thermal gradients being formed in the gain medium. This chapter presented a few of the schemes implemented by previous authors to manage the thermal effects in both rod and slab lasers, before it was decided to use a design based on the edge-pumped architecture [74], because of its performance, simplicity and potential cost savings over other designs.

Chapter 6

Design and construction of the high power laser head

6.1 Introduction

A slab-type design based on the edge-pumped architecture was chosen for the high power guide star source, as discussed in Chapter 5. This design was selected primarily for its large pump windows, which simplify the pumping arrangement and allow the use of inexpensive, large aperture laser diode arrays.

In this Chapter, design and construction details of the high power laser head are presented. Characterization of this laser is then described in Chapter 7. The design is not intended to be the final version of the laser head for the guide star source but is aimed to demonstrate power scaling concepts and to trial design options for the final field deployable system.

Section 6.2 contains a design summary, then Section 6.3 presents details on the slab dimensions. The slab height (in the cooling direction) is discussed in Section 6.3.1. This parameter sets the mode size in the resonator, which impacts the damage susceptibility of resonator optics and also influences the pump volume and pump density which determine the small signal gain of the laser. The slab width (in the pumping direction) is discussed in Section 6.3.2. This parameter, in combination with the doping concentration, determines both the pump absorption percentage and the pumping uniformity. An analysis is presented of the trade-off that exists between the desire to have high pump absorption and also a high pump uniformity to minimize thermal lensing in the width direction. The slab length is discussed in Section 6.3.3, then Section 6.3.4 a method for controlling parasitic oscillations by tilting one side to destroy the TIR mode paths within the slab. Finally, technical details of the laser head construction are presented in Section 6.4, showing the

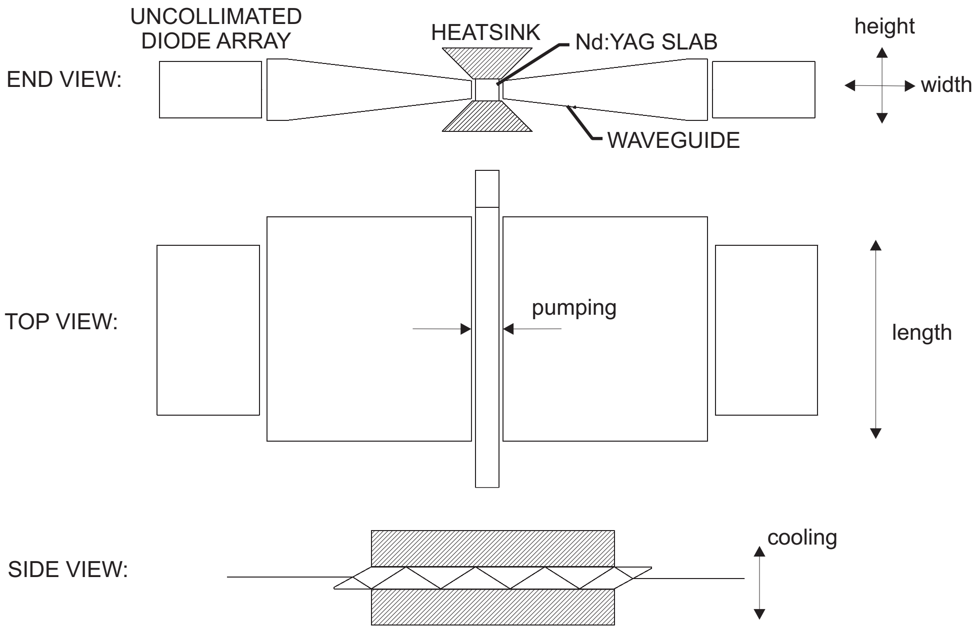

Figure 6.1: Diagram of the high power laser head. It consists of a Nd:YAG slab clamped between copper cooling blocks and pumped from each side by laser diode arrays. The laser mode takes a zigzag path through the slab to average out the major thermal distortions in the vertical direction.

pumping assembly, slab mount and cooling configuration.

6.2 Design summary

A schematic of the laser head design is shown in Figure 6.1. It consists of a side pumped, conduction cooled zigzag slab with Brewster angled windows [33]. With the whole sides of the slab available for pumping, the pump light from the laser diode arrays has only to be condensed by a factor of 2.5 to enter the slab which greatly simplifies the waveguide design. Un-collimated laser diode arrays, which are the most inexpensive form of pump light, can then be used as the pump source and their large fast- and slow-axis divergence is beneficial in this case as it helps to mix up the pump light in the waveguide and provide uniform illumination of the whole slab aperture providing uniform heating. The top and bottom surfaces of the slab are coated with a thin, 2.5 μm, layer of silicon dioxide to maintain TIR when in contact with the heat sink,

6.3 Laser slab design

The dimensions of the final Nd:YAG laser slab are shown in Figure 6.2 and a detailed technical drawing that includes tolerances and surface finishes can be found in Appendix E. The slab was cut from high purity, low wavefront distortion Nd:YAG material from Scientific Materials Corp. The Nd:YAG was taken from the boule with a crystallographic direction that minimizes the effect of thermal birefringence and growth striations [104], as specified in Appendix E.

The dimensions and doping concentration were carefully chosen to optimise the performance of the laser. This section describes how these values were selected.

6.3.1 Slab height

The slab height determines the size of the laser mode in the slab since a circular mode profile will be used, and the slab width will be made larger than the height to improve the thermal properties of the laser head (Section 6.3.2). The slab height will therefore be the limiting aperture inside the resonator and the mode size should be made to fit the slab height. By determining the mode size, the slab height will also determine the lasers small signal gain, Q-switched energy extraction efficiency and Q-switched pulse-width for a given pump energy, as explained below.

For a 4-level laser such as Nd:YAG, the logarithmic small-signal gain, g_0l, is given by [61]

$$g_0l = \left(\frac{\sigma_{21}}{h\nu V}\right)\eta E_p \tag{6.1}$$

Where σ_{21} is the stimulated emission cross section, $h\nu$ is the photon energy, V is the pumped volume, E_p is the pump energy and η is an efficiency term which is the product of the quantum defect, beam overlap efficiency, absorption efficiency, energy storage efficiency and quantum efficiency.

The small-signal gain is related to the slab height through the volume term in Equation 6.1. Generally, a high small signal gain is desirable as this leads to high laser efficiencies [49], but for guide star lasers requiring long macro-pulse widths to avoid sodium bleaching, a high gain is not desired as it also decreases the Q-switched pulse-width of the laser [49].

The relationship between pulse width and small signal gain of a Q-switched laser can be obtained from a solution to the laser rate equations [105]. These equations have been solved by Degnan [49] for the case where the laser outcoupling fraction has been optimized and top-hat beam profiles and uniform pump densities are assumed. He showed that the pulse width, output energy and extraction efficiency can all be expressed in terms of the

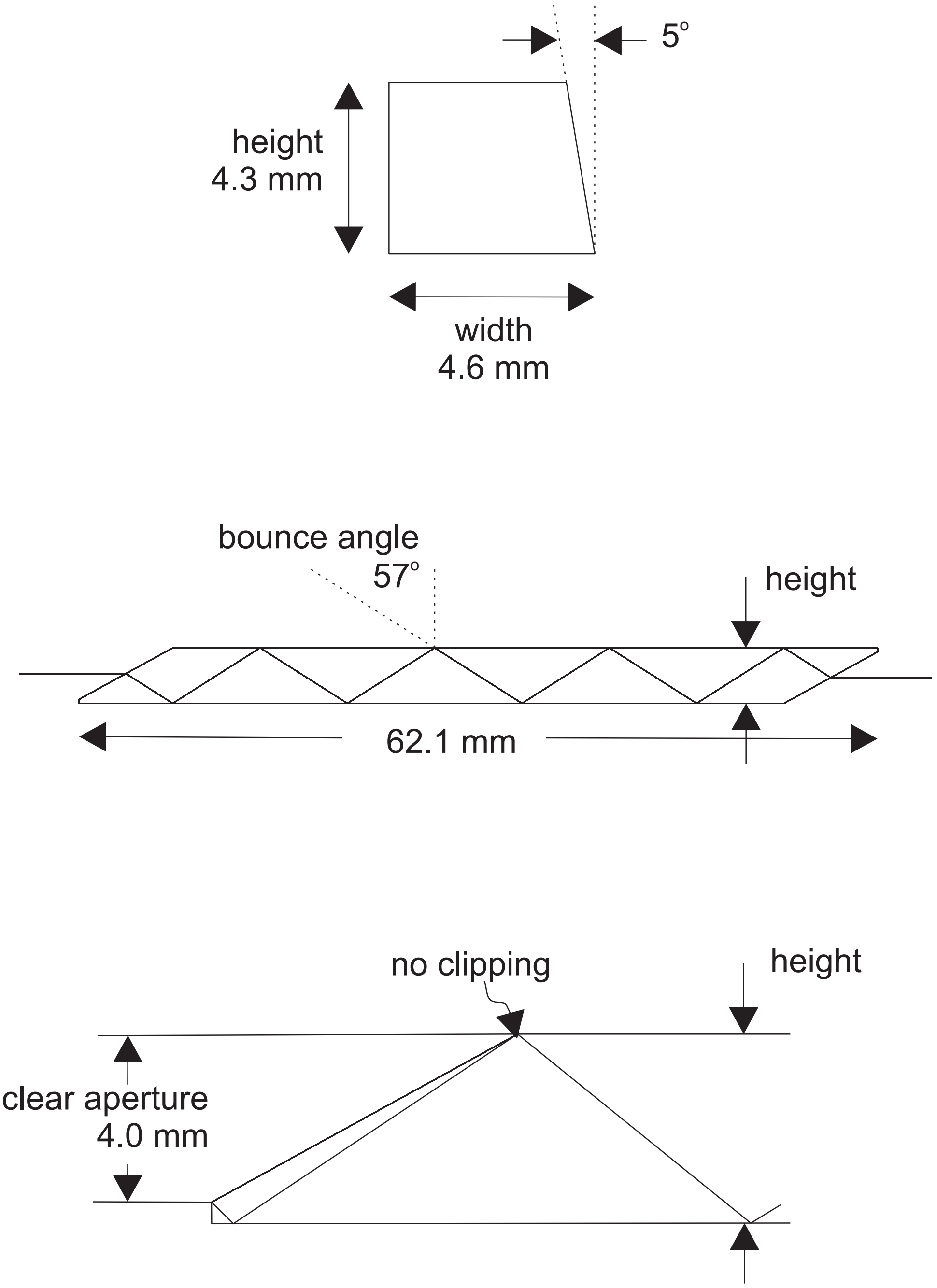

Figure 6.2: Dimensions of the Nd:YAG laser slab. One side of the slab is wedged to prevent parasitic oscillations as is discussed in Section 6.3.4. Note that the slab height is slightly larger than the clear aperture to prevent the clear aperture being reduced inside the slab due to clipping at the Brewster window after its first TIR bounce inside the slab. See Appendix E for a detailed technical drawing.

dimensionless variable Z defined as

$$Z = \frac{2g_0 l}{L} \tag{6.2}$$

with $g_0 l$ being the logarithmic small signal gain and L being the round trip loss, not including the outcoupling fraction. An expression for the Q-switched pulse width, t_p, can the be written as [49]

$$t_p = \frac{t_R}{L}\left(\frac{\ln Z}{Z[1 - a\,(1 - \ln a)]}\right), \tag{6.3}$$

where

$$a = \frac{Z-1}{Z \ln Z} \tag{6.4}$$

and t_R is the resonator round trip time. Equation 6.3 shows that the Q-switched pulse width gets shorter for increasing small signal gain. Hence to produce long pulses, which is desired for the guide star laser, the small signal gain should be small.

A negative consequence of reducing the small signal gain is that the laser extraction efficiency, η_e, which represents the fraction of useful energy stored in the upper laseing state, reduces with lower small signal gains according to [49]

$$\eta_e = 1 - \left(\frac{1 + \ln Z}{Z}\right) \tag{6.5}$$

A plot of the Q-switch extraction efficiency is shown in Figure 6.3.

Hence the small signal gain of the laser should be optimised so that long Q-switched pulse lengths are obtained without a significant drop in pulse energy occuring.

In Chapter 4 it was observed that for a small signal gain value of 0.31, 10 mJ output pulses were produced. Using equation 6.5, this results in a Q-switched extraction efficiency of approximately 71 %. This value is situated at the “knee” of Figure 6.3. This is an ideal place to operate as the small signal gain is low, giving long Q-switched pulse widths (Equation 6.3), but any further reduction in small signal gain is undesirable as it will lead to a significant drop in extraction efficiency, as can be observed in Figure 6.3.

Hence it was decided to operate the high power laser with the same mode size, ($\omega =$ 1.2 mm), as the low power laser.

For a beam size of $\omega = 1.2$ mm the vertical clear aperture of the slab was chosen to be 4.0 mm so that the mode diameter fills 60 % of the clear aperture for efficient opperation as recommended by Siegman [106]. The slab was chosen slightly larger (4.3 mm) to preserve the clear aperture by preventing clipping on the Brewster window as illustrated in Figure 6.2.

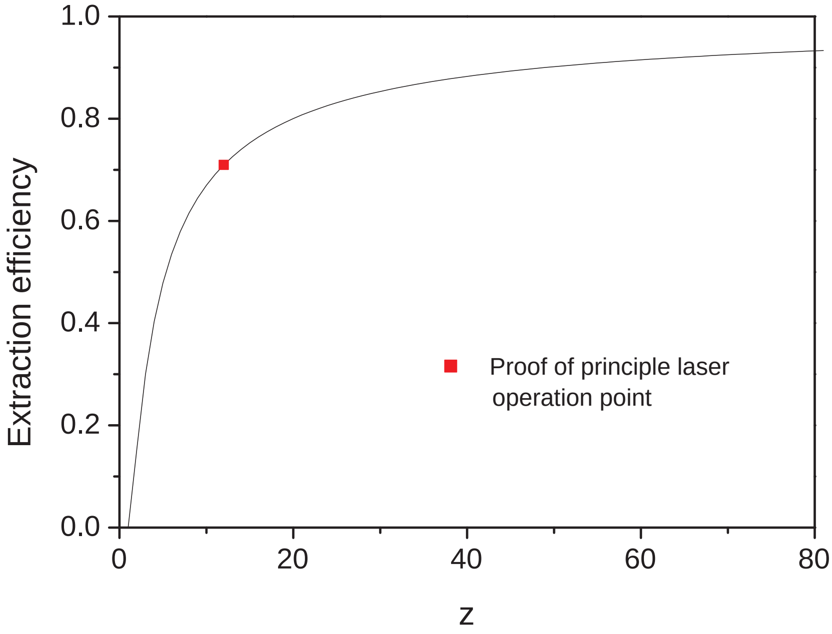

Figure 6.3: The Q-switched energy extraction efficiency plotted against the parameter Z. The Z-value at which the proof of principle laser operates is highlighted.

6.3.2 Slab width

The width of the slab, combined with the Nd doping concentration, determine the fraction of the pump light absorbed in the slab and also the thermal lensing in the width direction, as the pump light is absorbed exponentially from the edge of the slab resulting in non-uniform heating. This section presents an analysis of the pump absorption fraction and pump uniformity in an edge-pumped slab laser pumped with a broad-band (2-5 nm) pump source and uses the results to determine the width and doping concentration for the slave laser crystal.

Rutherford et al. [74] presented an edge-pumped laser design using narrow-band ($<$ 1 nm) fibre-coupled lasers as the pump source (Figure 5.4). This design has a height of 1.45 mm and width of 4.57 mm to increase the single-pass pump absorption, increase the area of the cooling surfaces, and reduce the slab temperature. An astigmatic mode size in the laser slab must be used for this design to sweep out all available gain in the width direction. This requires intra-cavity cylindrical optics.

For our case, the large slab height of 4.3 mm enables the slabs aspect ratio to be made approximately 1:1 enabling a circular beam, while still having reasonable pump absorption efficiency and good gain sweep out. This simplifies the resonator design by requiring fewer intra-cavity lenses and allows the use of spherical lenses which can be manufactured with greater precision than cylindrical lenses, thereby reducing the round trip losses of the cavity.

To calculate the amount of pump absorption in our slab, an equation must be used which can account for the broad spectral width and angular distribution of the un-collimated laser diode arrays. Barnes et al. [107] have shown that the fractional absorption, η_A, of a pump source with spectral width, $\Delta\lambda$, and angular intensity distribution, $F(\theta,\phi)$, in a slab of width l can be calculated by integrating the absorption fraction of pump rays over all angles (θ,ϕ) and wavelengths λ. They arrive at the equation

$$\eta_A = \frac{\int_{\lambda_1}^{\lambda_2}\int_0^{\frac{\pi}{2}}\int_0^{\frac{\pi}{2}} P(\lambda)F(\theta,\phi)[1-\exp(-\beta(\lambda)l(\theta,\phi))]\sin\theta d\theta d\phi d\lambda}{\int_{\lambda_1}^{\lambda_2}\int_0^{\frac{\pi}{2}}\int_0^{\frac{\pi}{2}} P(\lambda)F(\theta,\phi)\sin\theta d\theta d\phi d\lambda} \tag{6.6}$$

where $P(\lambda)$ is a function defining the spectral distribution of the laser diode array and $\beta(\lambda)$ is the absorption coefficient as a function of wavelength.

This equation can be solved if the absorption coefficient, $\beta(\lambda)$, for the broad-bandwidth pump source is approximated by the absorption coefficient for a single frequency source, β that produces similar absorption as the broad spectrum source. For a 2 nm 808 nm pump source $\beta = 0.52$, while for a 5 nm pump source $\beta = 0.39$ [107]. The bandwidths 2 nm and 5 nm are typical of commercially available 808 nm laser diode arrays. Using these

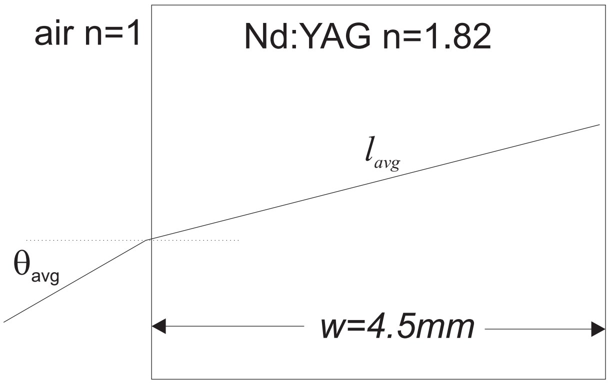

Figure 6.4: An average pump ray is incident on the slab at an angle θ_{avg} and experiences an absorption pathlength l_{avg} given by Equation 6.7

numbers, the pump absorption is shown plotted in Figure 6.5 for 1 % doped Nd:YAG and 808 nm pump beams of bandwidth 2 nm and 5 nm. For this figure, a uniform top-hat angular distribution ($F(\theta, \phi) = 1$) of pump light is assumed. To account for the real angular distribution of the pump light entering the slab, a mean absorption pathlength, l_{avg}, can be used, which represents the pathlength of an average ray in the slab, having an angle of θ_{avg} with respect to the input pump face. This can be derived using Snell's law and some simple trigonometry using the parameters in Figure 6.4. The value of l_{avg} can be calculated using the following trigonometric relationship

$$l_{avg} = \frac{w}{\cos[\arcsin\left(\frac{1}{n}\sin(\theta_{avg})\right)]} \tag{6.7}$$

where w is the width of the slab, n is the refractive index of Nd:YAG and θ_{avg} is approximately 30° for the pump light exiting the waveguides of Figure 6.1[1] using un-collimated laser diode arrays having typical fast axis divergence of 30° (FWHM) and slow axis divergence 10°.

For a slab width of 4.5 mm, Equation 6.7 gives $l_{avg} = 4.7$ mm. From Figure 6.5, it can be seen that this width will result in substantial pump absorption, of approximately 84 % for a 5 nm bandwidth pump source and 91 % for a 2 nm source. A slab width of 4.5 mm would be ideal for the high power laser crystal, as it enables a close-to-square aspect ratio to be used[2], allowing a circular beam in the slab and alleviating the need for lossy cylindrical resonator optics. Hence this value was chosen as the slab width.

For the edge-pumped laser design, the slab is pumped from each side (Figure 6.1), which introduces a thermal gradient in the horizontal direction, as the pump density is

---

[1] More details of the waveguides can be found in Section 6.4.1

[2] the width should be made slightly wider than the height to enable one side to be wedged to destroy parasitic mode paths, as discussed in Section 6.3.4

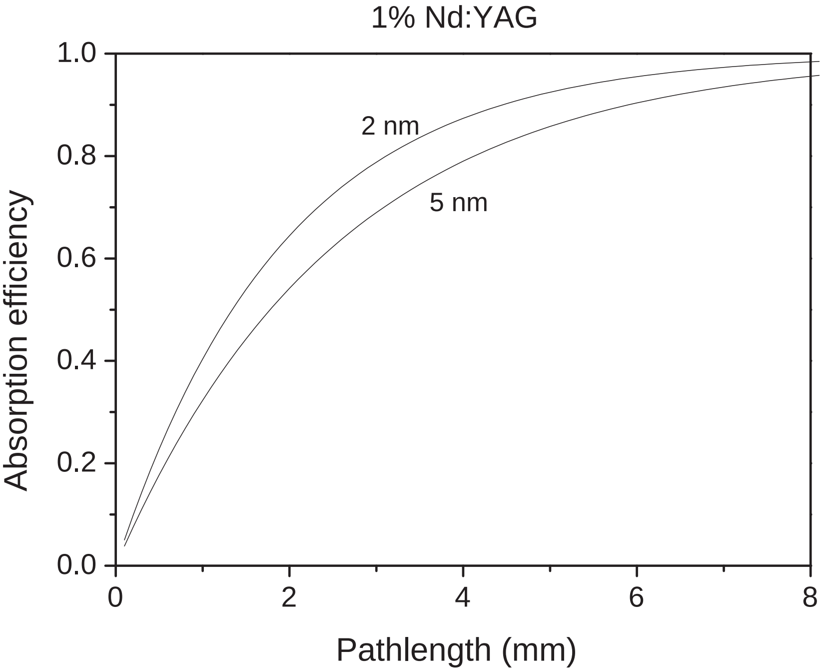

Figure 6.5: Absorption percentage of 1 % doped Nd:YAG when pumped with a broad bandwidth pump source with spectral bandwidths 2 nm and 5 nm, centred at 808 nm.

highest at the edge face and lowest at the centre. This gradient is transverse to the direction of zigzag and hence will not be averaged by the zigzag beam path. A thermal lens will therefore exist in the horizontal direction. The extent of lensing is determined by the pump uniformity across the width, which for a given pump energy and slab width, is determined by the doping concentration of the crystal.

The amount of lensing can be quantified by examining the pump absorption profile across the slab width. The absorption profile will have a hyperbolic shape, $\cosh(\beta_{\Delta\lambda}x)$, since the slab is pumped from opposing sides and the pump light is absorbed exponentially from the edge[3]. In this formula, $\beta_{\Delta\lambda}$ is the absorption coefficient for a pump source of spectral width $\Delta\lambda$ and x is the position across the width (zero is defined to be the centre of the slab). With the appropriate constant of proportionality, the pump absorption, normalized to the absorbtion at the slab edge, $\rho_{norm}(x)$, can then be written as [108]

$$\rho_{norm}(x) = \frac{1}{\rho(w/2)} \frac{\exp\left(-\beta_{\Delta\lambda}\frac{w}{2}\right)}{1 - R_p e^{-\beta_{\Delta\lambda} w}} \cosh(\beta_{\Delta\lambda}x) \tag{6.8}$$

where the factor R_p represents the reflectivity of the side faces of the slab and takes account of the fact that some fraction of the pump light will bounce back a forth between the side faces of the slab.

Equation 6.8 can be plotted to show the pump uniformity in the slab and an example is shown in Figure 6.6, for $-w/2 \leq x \geq w/2$, 1 % doped Nd:YAG and 5 nm pump source.

Table 6.1 uses Equations 6.8 and 6.6 to display the relationship between pump uniformity and total pump absorption for various Nd doping concentrations.[4] It shows that a trade-off exists between the two, that is, to achieve a uniform pump absorption and hence low thermal lensing in the horizontal direction, a low doping concentration should be selected, but this is at the expense of pump absorption percentage.

Given the data of Table 6.1, it was decided to select a doping concentration of 1.0 % Nd. This gives a balance between good pump absorbtion (84 %) and reasonable pump uniformity ($\rho_{norm}(0) = 0.71$. If in practice it is found that the horizontal thermal lensing is too strong, the laser diodes can be detuned from the peak absorption band to increase the pump uniformity and reduce the lensing.

---

[3] $\cosh(x) \equiv \frac{1}{2}(e^x + e^{-x})$

[4] The doping concentration of Nd:YAG is limited to approximately 1.1 %. Higher doping levels can quench the upper state lifetime due to up-conversion and introduce strain in the crystal, reducing the optical quality.

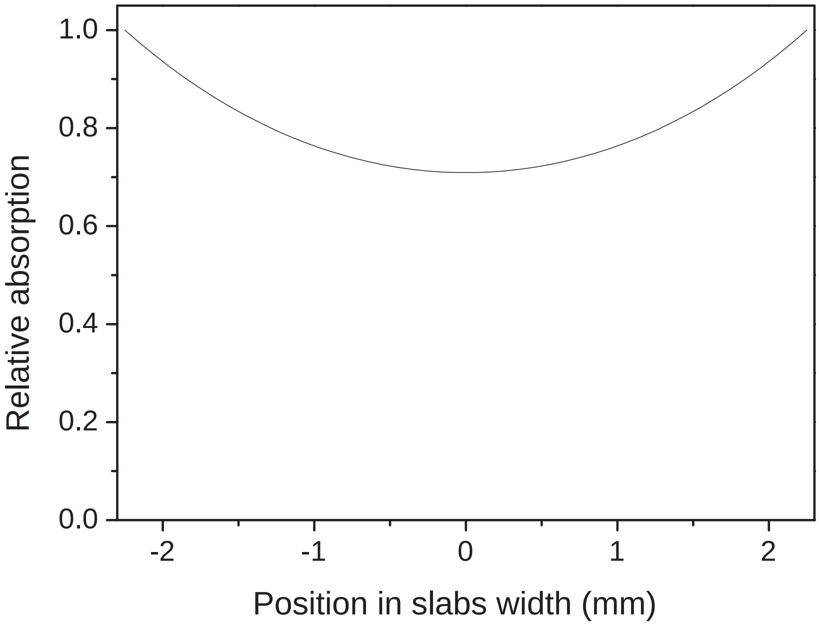

Figure 6.6: The calculated pump absorption profile across the slabs width when pumping from opposing sides by a 5 nm bandwidth, 808 nm pump source. A 1 % doped Nd:YAG slab is used for this example and the pump absorption at the centre is approximately 71 % that of the edges.

Nd (%)	$\rho_{norm}(0), 5\ nm$	$\eta(A), 5\ nm$
0.6	0.88	66.7
0.7	0.84	72.3
0.8	0.80	76.9
0.9	0.75	80.8
1.0	0.71	84.0
1.1	0.67	86.7

Table 6.1: Calculated values of the pump absorption at the centre of the slab relative to the edge, $\rho_{norm}(0)$, and the pump absorption percentage, $\eta(A)$, for a 5 nm spectral bandwidth pump source and various Nd doping concentrations. The slab width in this case is 4.5 mm.

6.3.3 Slab length

An even-bounce slab design was chosen as this configuration is less sensitive to mirror pointing errors than odd-bounce designs [109], and reduces the slab manufacturing costs by having parallel entrance and exit faces. An 8-bounce geometry was used to provide enough bounces for effective averaging of thermal distortions and to provide a large pump window. Having more bounces increases the mode loss from scatter and absorption arising from each TIR bounce inside the slab. The 8-bounce geometry also makes the slab long enough to allow pumping by 4 cm laser diode arrays on each side as will be described later.

6.3.4 Parasitic oscillation control

Parasitic oscillations occur when low loss, closed TIR paths can be formed within the laser crystal, allowing an internal mode to develop and drain the energy stored in the crystal. A couple of possible parasitic-mode paths are shown for a Brewster angled zigzag slab in Figure 6.7. The top and bottom of the slab have SiO_2 coatings of refractive index 1.45 and the Nd:YAG has a refractive index of 1.82, making the critical angle for TIR at this interface 52.9°. For the air-Nd:YAG interface the angle is 33.4°. So if one of the slab sides is not wedged, the parasitic modes in Figure 6.7 have low-loss TIR paths within the slab, clamping the lasers gain at a very low level. Tilting one of the sides of the slab by a small angle, as in Figure 6.2, causes the path of parasitic modes to pick up twice the wedge angle on each round trip, quickly destroying TIR and introducing significant Fresnel losses to the mode. It was estimated that for the slab of Figure 6.2, a wedge angle of 2.5° is sufficient to cause round trip losses and kill the parasitic modes shown in Figure 6.7. It was decided to use a wedge angle slightly larger than this (5°), to be safe from these modes and any other modes that were not predicted. It may be necessary to run a finite element simulation with the predicted small signal gain to fully examine the different parasitic modes paths that are possible.

6.4 Laser head construction

6.4.1 Laser pump modules

The slab is pumped from each side by the laser pump modules shown in Figure 6.8. Each module consists of a pair of laser diode arrays and a glass wave-guide to channel the pump light into the slab.

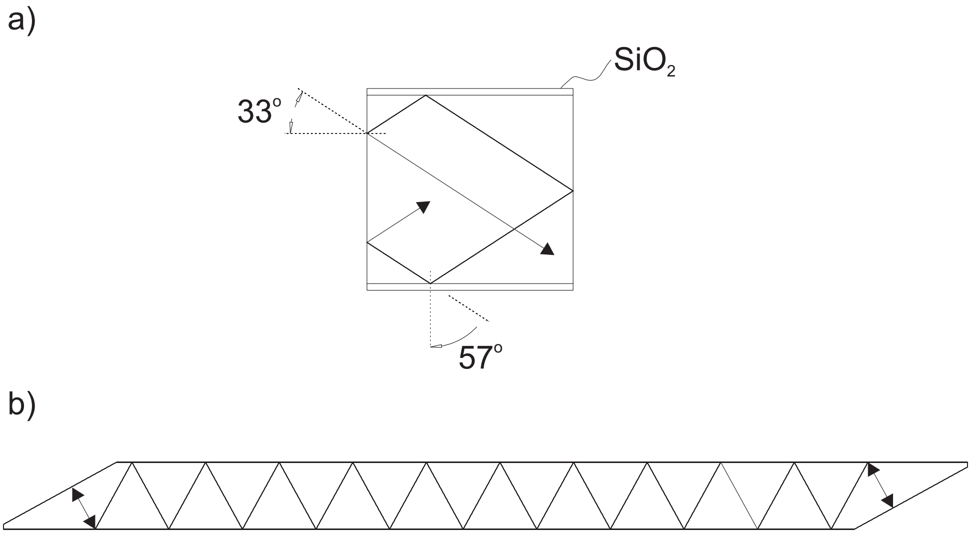

Figure 6.7: Two possible paths for parasitic oscillations in a Brewster-angled zigzag slab. Part a) shows a mode running in the slabs cross-section while part b) shows a mode taking a cork-screw path down the slabs length and reflecting off the Brewster angled windows. Both of these modes undergo TIR bounces making them low loss.

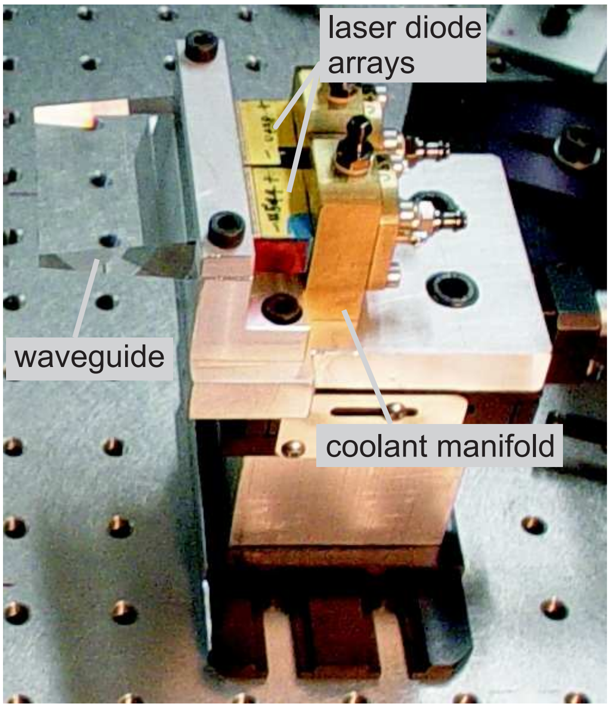

Figure 6.8: Photograph of a laser pump module. The light from two laser diode arrays is condensed and transferred to the slab using a glass waveguide. The assembly is mounted on a linear translation stage to enable the waveguide to be brought close to the slab.

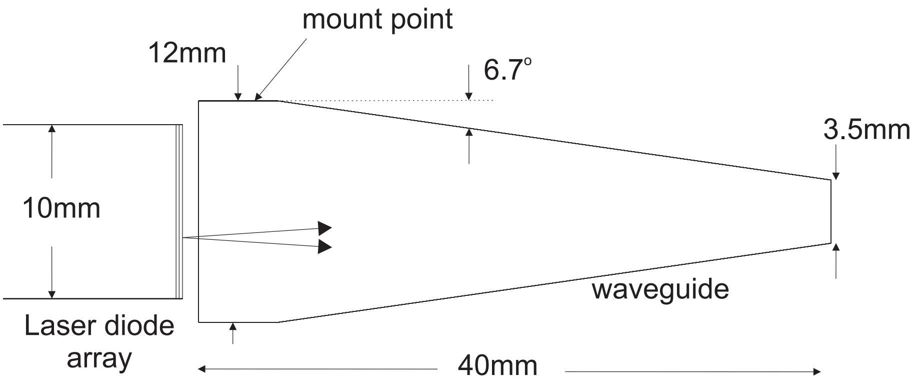

Figure 6.9: Cross section of the laser diode array and waveguide used to pump the slab. The slow-axis of the array runs in the vertical direction (divergance angle shown) and the fast axis is into the page.

A schematic of the waveguide and laser diodes is shown in Figure 6.9, and detailed technical drawings can be found in Appendix E. The un-collimated light from the laser diode arrays has a FWHM divergence angle of 30° in the fast axis and 10° in the slow axis. This large divergence angle enables the striped output from the individual bars in the array to be mixed in the waveguide to produce a close to uniform pump distribution in the slab. The entrance and exit faces of the waveguide are coated with a broad-angle AR layer to reduce pump losses and the edges were kept sharp (without chamfer) to minimize transmission losses. The total loss from the diode output to the output of the waveguide was measured to be 3 %.

The height of the waveguide at the end near the diode array was made 12 mm, slightly taller than the array height (10 mm) to allow all pump rays to enter the waveguide. There is a horizontal ledge on the top and bottom for mounting as shown in Figure 6.9. The height tapers down to 3.5 mm at the end nearest the slab to allow the exit rays to enter the slab (the slab height is 4.3 mm). The length of the waveguide was made 40 mm to give space between the pump diodes and the slab heatsinks. This resulted in a taper angle of 6.6° as shown.

The laser diodes are 50-bar, high peak power, water-cooled arrays manufactured by SDL diode laboratories[5].The performance of the laser diodes will be described in Chapter 7.

The majority of rays emitted from the pump source will undergo one TIR bounce within the waveguide but some rays will have no bounces and some will have two as shown in Figure 6.10. For each TIR bounce, the ray will pick up twice the slant angle of the waveguide (13.2°) causing a striped pattern observed in the output of the waveguide.

---

[5] The author gratefully acknowledges Northrop Grumman (NGST) for the loan of the laser diodes

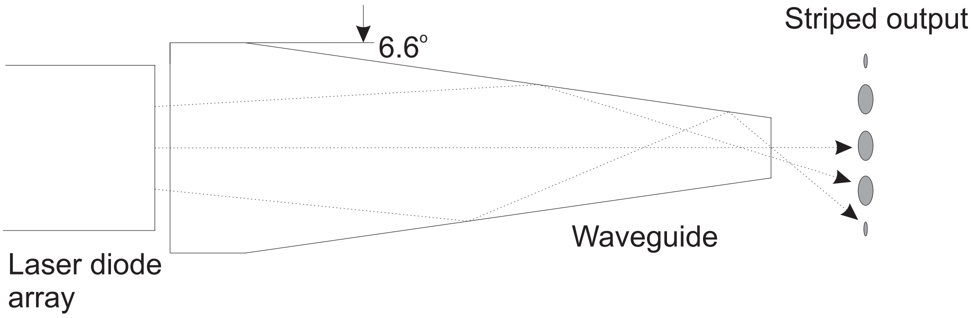

Figure 6.10: The divergent light emitted by the laser diode array can make zero, one or two TIR bounces within the waveguide. Each bounce adds 13.2° to the rays angle resulting in the striped output shown (stripes into page).

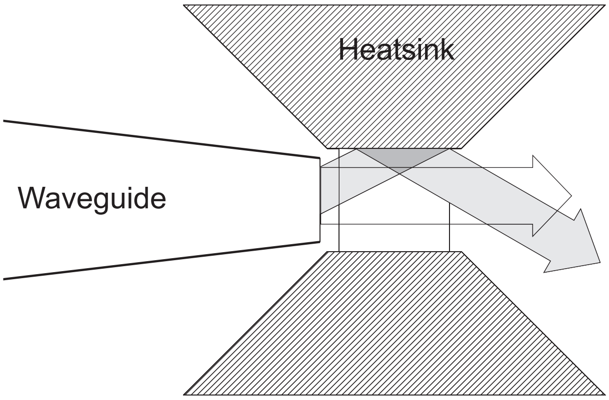

Figure 6.11: The striped output from the waveguides undergoes a TIR bounce within the slab resulting in improved pump uniformity.

Each stripe has an angular separation of 13.2°, corresponding to groups of rays that have undergone 0, 1 or 2 TIR bounces. This pattern was observed using a hand held infra-red viewer and has been reproduced schematically in Figure 6.10.

For the efficient operation of a high power solid state laser, it is usually desirable to have a uniform pump distribution to ensure uniform heating of the gain region, so a striped output from the waveguides is not ideal, but with the slab butted up close to the exit port of the waveguide as in Figure 6.11, the extra TIR bounce inside the slab will help improve pump uniformity.

Slab mounting and cooling configuration

The Nd:YAG laser slab was clamped between two, water cooled copper blocks as shown in the photograph of Figure 6.12. To reduce the thermal impedance of the Nd:YAG-copper interface a thin, 0.125 mm, layer of indium foil was inserted between the slab and copper. Indium is a soft malleable material that can fill the surface irregularities of the machined copper surface and improve the thermal contact between the Nd:YAG crystal and heat sink. The assembly of the heatsink-indium-Nd:YAG-indium-heatsink sandwich is no trivial task as it is difficult to achieve an intimate, even, thermal contact without applying excessive clamping stress on the crystal. A lot of time was spent refining the assembly procedure to achieve maximal performance from the laser (performance details in Chapter 7). The best technique was found to be the following: Firstly, the pieces of indium foil were lightly rolled onto the Nd:YAG crystal to reduce the Nd:YAG-indium thermal resistance. This is the most important interface as the Nd:YAG has the least thermal conductance of the sandwich.[6] The Nd:YAG and indium layers are then placed on the lower copper block of figure 6.12, and the upper copper block is brought down square using the stainless steel guiding pins, seen in figure 6.12. Pressure is then applied to the centre of the upper cooling block with a single screw, before the four screws at the corners of the upper cooling block are tightened to hold the pressure.

The source of cooling water for the copper heat sinks is a recirculating chiller [110], which was used to cool both the laser diodes and the laser slab. A corrosion inhibitor and algaecide [111] was added to the cooling water to protect the micro-channels of the laser diodes from decay.

The complete laser head assembly, including the slab mount and pump modules is shown in Figure 6.13.

6.4.2 Teflon coating

Unfortunately, some of the laser slabs were damaged on arrival from the manufacturer, with some areas of the silicon dioxide layers lifting off. An example is shown in the photograph of Figure 6.14. To fix this problem and to restore the TIR interface between the Nd:YAG and heatsink, a thin film of low refractive index Teflon AF, (n=1.29) was applied to the damaged areas of the slab [112]. Like SiO_2, Teflon is a relatively poor thermal conductor, so it is necessary to apply only a thin film to minimize thermal resistance. Hence the Teflon was first dissolved in a solvent (FC-75) with a 4 % Teflon, 96 % solvent solution. This solution was then applied to the damaged area of the slab with a fine paint brush. After application the solvent quickly evaporates leaving only a thin layer of Teflon. Unlike SiO_2, the Teflon coating is very soft and can be easily rubbed off so the slab had to be cleaned and recoated for each rebuild of the laser head. With the Teflon coating applied and the slab mounted it was observed that the single pass loss of the slab was not diminished by this procedure.

---

[6] the thermal conductivity of Nd:YAG is around 6-times lower than indium and more than a thousand times lower than copper.

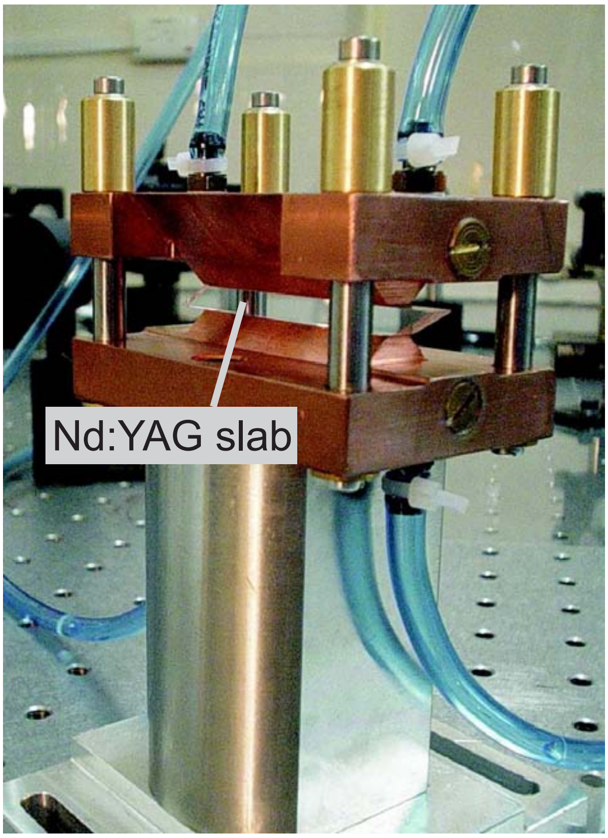

Figure 6.12: The mounting and cooling arrangement for the laser slab. The slab is clamped between water-cooled copper heatsinks, with an intermediate layer of indium foil to improve the thermal contact. During assembly, the top heatsink is guided down on the stainless steel pins seen at the corners of the mount.

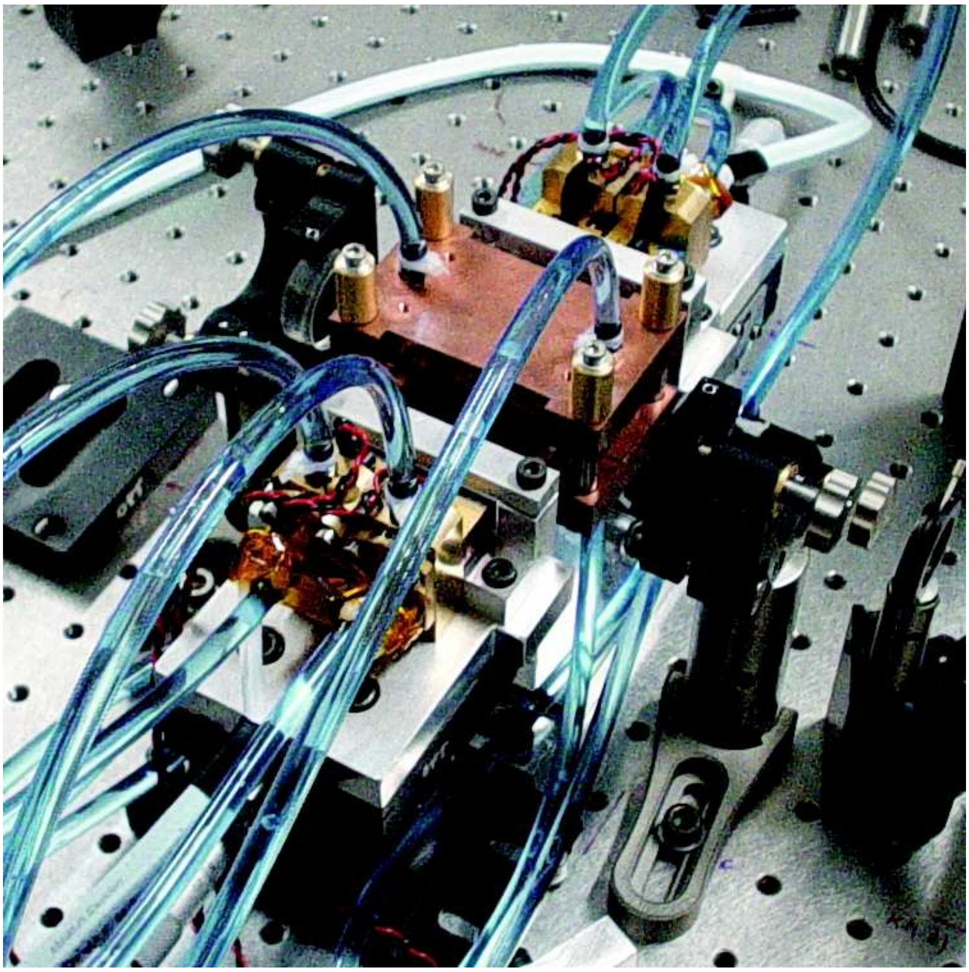

Figure 6.13: Picture of the completed laser head showing the slab mount, pumping modules and cooling lines.

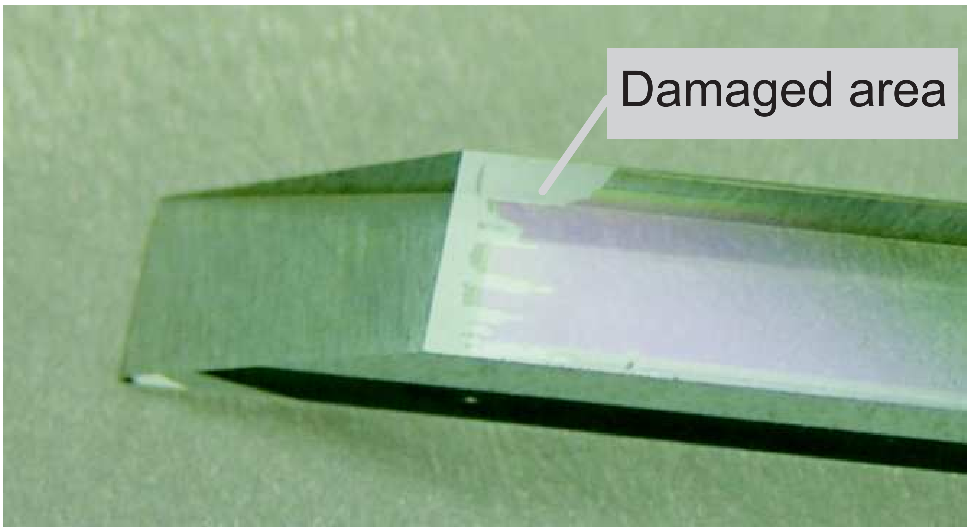

Figure 6.14: The Nd:YAG laser slab with damage to the SiO_2 coating.

6.5 Conclusions

This chapter presented the design and construction details of the high power laser head. It was shown that the choice of crystal dimensions can have a significant impact on the performance of the laser and aspects such as the slabs height, width and length were all chosen to optimize the performance for an injection mode-locked slave laser. The height was chosen to be 4.3 mm, fixing the mode size in the slab to be $\omega = 1.2$ mm, and setting the lasers small signal gain to provide long duration Q-switched pulses while maintaining a substantial Q-switch energy extraction efficiency and placing a limit on the maximum intra-cavity pulse energy before the onset of damage to optics. The slab width was chosen to be 4.5 mm to provide a close-to-square slab ratio to enable the use of high quality spherical optics, and also to provide a reasonable pump absorption efficiency and good pump uniformity. Section 6.3.4 presented an analysis of possible parasitic mode paths that exist in slabs with polished sides, and concluded that one side of the slab should be wedged at 5° to destroy the TIR paths. Finally, some construction details were presented in Section 6.4.1, including the slab mounting configuration and procedures to establish a uniform thermal contact between the slab and heatsink.

Chapter 7

Performance of the high power 1064 nm laser

7.1 Introduction

A low average power 50 Hz repetition rate 1064 nm laser was presented in Chapter 3 and used to demonstrate that the approach of injection mode-locking and stretched Q-switching can simultaneously satisfy the requirements of wavelength, bandwidth and pulse width for advanced SFG guide-star systems. The outstanding requirements that could not be demonstrated with that laser was the need for high average powers (10 W) and a high repetition rate (800 Hz) to provide adequate sampling of the time varying effects of atmospheric turbulence.

The primary issue in scaling the average power is the management of thermal effects such as thermal lensing and thermal birefringence, associated with the high heat loads deposited in the gain medium by a high power pump source. Chapter 6 presented design and construction details of a new laser head design, which aims to minimize thermal gradients within the laser crystal, thus enabling power scaling of the injection mode-locked laser.

This chapter presents the characterization and performance testing of this new laser. It begins with a description of the laser pump modules, including the power output and spectral properties of the laser diode arrays, then goes on to present the performance results of the completed Nd:YAG laser head assembly. Initially the laser was run in a short, standing-wave test resonator to asess the total output power available and to analyse the thermal properties within the Nd:YAG slab. Measurements of the thermal lens focal length were taken and the results are presented. The thermal lens value is used to design a stable single mode ring resonator, into which the laser head was incorporated.

Performance results from this high power injection mode-locked slave laser are then presented, showing the combination of high power levels, good beam-quality and excellent bandwidth control when operating at 800 Hz PRF [33].

7.2 Pump laser performance

This section describes the performance of the laser diodes and outlines the measurements of wavelength, output power and spectral width that were undertaken to optimise the efficiency of the Nd:YAG laser. The diode driver and the cooling system used to control the temperature of the arrays, and the safety interlock system are also discussed.

7.2.1 QCW laser diode arrays

Quasi-cw (QCW) laser diode arrays were selected for use in the high power laser head as this mode of operation will give greater laser efficiency compared to cw laser diodes for the PRF required. The difference in efficiency can be accounted for by noting that the laser is required to operate at 800 Hz PRF (1.25 ms period) while the upper-state fluorescence lifetime of Nd:YAG is only 230 μs, and so the efficiency of a laser using a cw-pump source is expected to be approximately $\frac{230}{1.25}\frac{\mu s}{ms} \approx 0.2$ that of a QCW source.

One advantage that cw diodes do have is the longer operating lifetime of these devices, which could be as much as a 2-4 times [113] [61] longer than a QCW diode. This would help to reduce the cost of maintaining the guide star source. The maintenance interval for the replacement of laser diodes can, however, be substantially increased for both QCW and cw arrays by purchasing higher power arrays (at an increased initial cost) then running at a power level less than the maximum rated output.

The laser diodes used for the high power experiments of this chapter are un-collimated, water cooled QCW arrays manufactured by Spectra Diode Laboratories (SDL-3251-HK)[1]. These diodes were obtained from a previous application, but their specifications, shown in Table 7.1, are suitable for use in the injection mode-locked guide star laser head.

7.2.2 Laser diode drivers

The duty cycle of the laser diodes is 2 % (Table 7.1) which is unusually low for 808 nm diode arrays (the duty cycle is commonly 10-20 %). This means that the pump pulse width is restricted to 25 μs for a pulse repetition rate of 800 Hz, duty cycle 2 % (compared to $\approx 200\mu$s for a 20 % duty cycle array). This poses no problems optically, but does place

---

[1] Thank you to Northrop Grumman Corporation for the loan of the diodes.

Wavelength	808 nm ±4 nm
Spectral width	<4 nm FWHM
No. bars	50, 0.2 mm pitch
Peak power	5000 W
Duty cycle	2 %
Voltage	96 V (min)
Current	125 A (max)
Beam divergence	30° x 10° FWHM

Table 7.1: Manufacturers specifications and performance ratings for the SDL-3251-HK laser diode arrays

demands on the hardware used to drive the arrays, as the current drive pulse edges must have fast rise and fall times to get up and down within 25 μs. The required voltage of $\geq$ 96 V is also un-commonly high for laser diodes, limiting the choice of suitable, commercially available laser diode drivers further.

A Northrop Grumman e-Drive cw-QCW diode driver was selected for its reasonably fast rise time (5 μs) and high maximum voltage (350 V) as well as its high average power rating. The high compliance voltage enabled two laser diodes to be run from the one driver by connecting the arrays in series.

Given the high slew rate of the current pulse (up to 120 A in 5 μs), low inductance cable must be used to deliver the drive pulse to reduce back emf's and prevent overshoot and ringing on the rising and falling edges of the drive pulse. Any reverse bias on a laser diode array can be extremely hazardous and damage can be caused by as few as two volts of reverse bias. The high average power load on the cable prevents the use of coaxial cable, so Supra Ply loud speaker low inductance (0.2 μH/m) cable was chosen to deliver the current pulse to the laser diodes. When testing the cables with 100 A current pulses it was observed that the shape of the pulse was the same when using a cable length of 40 cm and 4 m, indicating that the inductance of the cable does not substantially affect the drive pulse.

7.2.3 Water cooling system

The SDL laser diode arrays require direct water cooling. The copper heatsinks used to cool the Nd:YAG slab were also designed for liquid cooling. To supply the coolant a Polyscience 6506T recirculating chiller was purchased. This unit can control the water temperature between -10℃ and 40℃ with a stability of ± 0.1℃, enabling the laser diodes

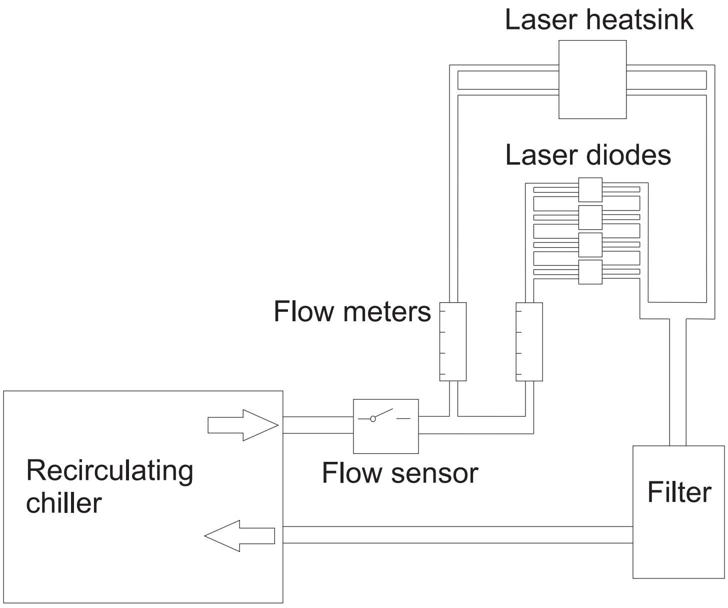

Figure 7.1: Block diagram of the water cooling system. The one chiller provides the temperature controlled coolant for the four laser diodes and heatsinks in the laser head.

to be temperature tuned to the 808 nm absorption band of Nd:YAG with an accuracy of ± 0.03nm. Ideally, the coolant to each laser diode should be individually temperature controlled to account for the slight wavelength differences between arrays (arising from manufacturing variations), and the laser slab heatsinks should be made as cold as possible to exploit the improved thermal properties of YAG at low temperatures [61]. For simplicity, however, the four laser diodes and the slab heatsinks were all cooled using the same chiller unit using an optimised water temperature. Section 7.2.5 contains further details on temperature tuning. To prevent blockage of the coolant micro-channels within the laser diode assembly, a 5 micron particle filter was fitted to reduce particulate matter. Figure 7.1 shows a block diagram of the cooling system.

Corrosion is a common problem in cooling systems having a low, un-monitored pH and in systems where different metals are in contact with the same cooling fluid, leading to degradation from galvanic processes. The above cooling system contains brass, copper and steel in the plumbing manifolds and laser diode arrays as well as other metals inside the chiller pump and plumbing. All of these metals are in contact with the coolant flow. To avoid corrosion, a corrosion inhibitor and algicide (Optishield Plus) was added to distilled water and used as the coolant.

7.2.4 Interlock system

Interlock systems are an essential feature of field deployable laser systems and also for lab based systems where the high optical powers generate safety issues and the high heat loads present a danger of catastrophic failure of the laser diodes and slab. An automated interlock shutdown system was therefore installed. The system consists of an electronic control box[2] and sensors to monitor the temperature of the laser diode arrays, a flow of coolant flow and door opening. The unit is designed to trip the laser diode power supplies if the laser diodes get too hot, if the coolant flow stops or if the laboratory door is opened.

The laser diode temperature was monitored using LM35 temperature sensors. These devices output a voltage that is directly proportional to their temperature. To provide an accurate reading, the LM35's were glued onto each array near the emitting aperture. The interlock unit was set to trip when the diode temperature exceeded 40℃.

7.2.5 Performance of individual laser diode arrays

It is important to have diodes with matching power and bandwidth on opposite sides of the laser slab to minimize thermal gradients in the width direction. If the diodes on one side have a slightly higher power output, that side of the laser crystal will be hotter resulting in a net thermal wedge created within the slab. Variation in spectral width and centre wavelength will also result in an asymmetric pump distribution and thermal wedging.

General specifications for the SDL laser diode arrays are shown in Table 7.1, but individual arrays can have markedly different properties, even when purchased from the same manufacturer and the same fabrication batch. These differences arise from the variation in semi-conductor material and from the mechanical tolerances present during assembly. Individual arrays can have different wavelengths, powers and bandwidths.

Table 7.2 summarizes the performance of each laser diode array, and shows that the centre wavelengths are within 1 nm, the spectral widths are between 2.4 nm and 4.9 nm and the average powers are within 7 % for 50 A, 25 μs current pulses at 800 Hz.

The data of Table 7.2 indicates that diodes U443 and U438 are well matched in power, spectral width and wavelength and so these two arrays were set opposite each other in the laser head, as were diodes U444 and U544, to give the most even pump distribution across the slab. Figure 7.2 shows the configuration of arrays within the laser head. Measurements of the thermal gradients within the slab (presented in Section 7.3.1) show that the thermal

---

[2] Credit for the design of the electronic control box goes to N. Wild, D. Mudge, D. Hosken, M. Heintze, B. Nation and other members of the optics group

Serial No.	Wavelength (25℃)	Spectral width (FWHM)	Power (avg at 50 A,)
U438	810 nm	2.4 nm	19.7 W
U443	810 nm	2.6 nm	19.8 W
U444	811 nm	2.4 nm	21.1 W
U544	811 nm	4.9 nm	20.4 W

Table 7.2: Measured performance of the four SDL-3251-HK laser diode arrays used in the laser head.

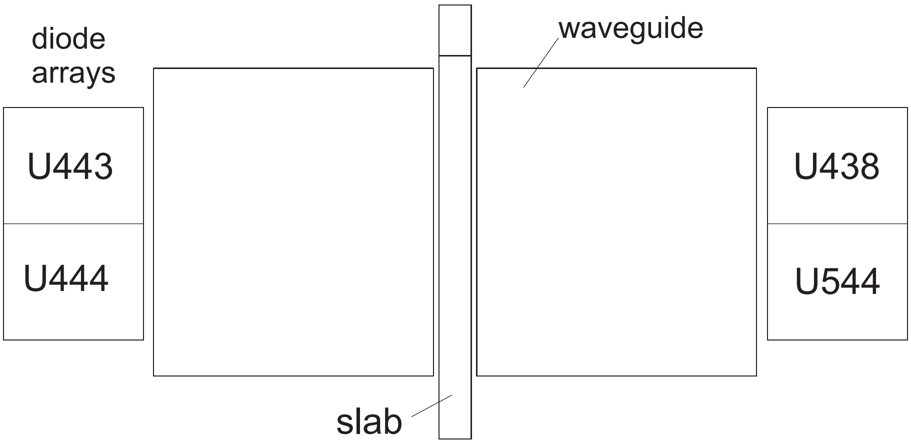

Figure 7.2: Optimized array configuration within the laser head showing arrays matched in power, wavelength and spectral width situated opposite each other

lensing is symmetric in the pump direction indicating that similar pump power is being delivered from each side of the slab.

7.2.6 Total pump power and absorbed pump power

The total pump power exiting the waveguides was measured for each pump module. The results are plotted in Figure 7.3. To determine the fraction of pump power absorbed in the slab, the power transmitted through the slab was measured. It was found that at least 17 % was transmitted indicating that the absorption in the slab is 83 %, or slightly lower, due to the difficulty in collecting the entire pump light transmitted through the slab. Some losses may of occurred during the transmission measurement due to the pump light impinging on the slab heat sink after passing through the slab.

The measured value of absorption (83 %) is similar to the theoretical prediction of 77 %, which includes an 8.5 % reflection loss from the un-coated Nd:YAG surface and approximately 84 % absorption in the 4.5 mm thick 1 at. % Nd:YAG crystal, as calculated in Section 6.3.2.

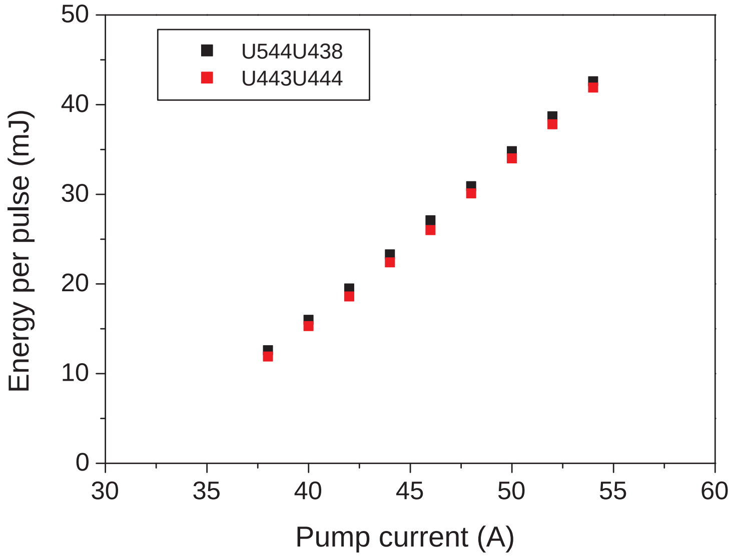

(a)

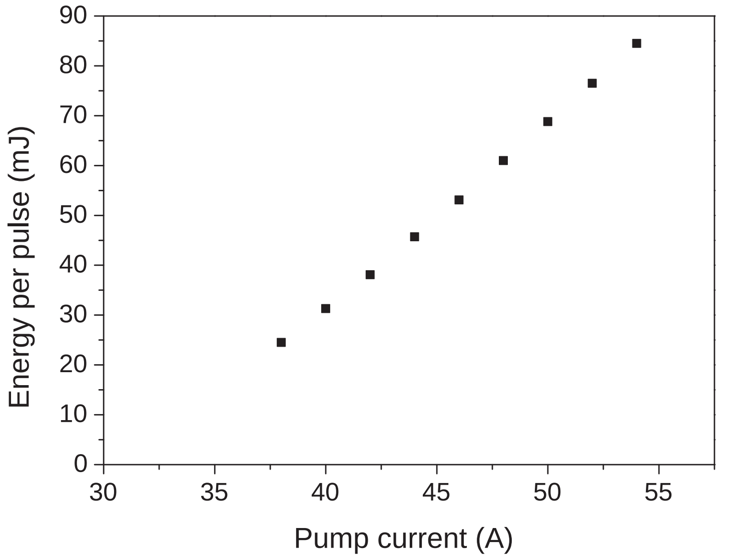

(b)

Figure 7.3: Plot of the total pump energy exiting the waveguides and incident on the slab. Part a) shows the energy from individual pump modules and part b) shows the sum of energy from both pump modules. The pulse repetition rate is 800 Hz for each case and the pulse width is 25 μs.

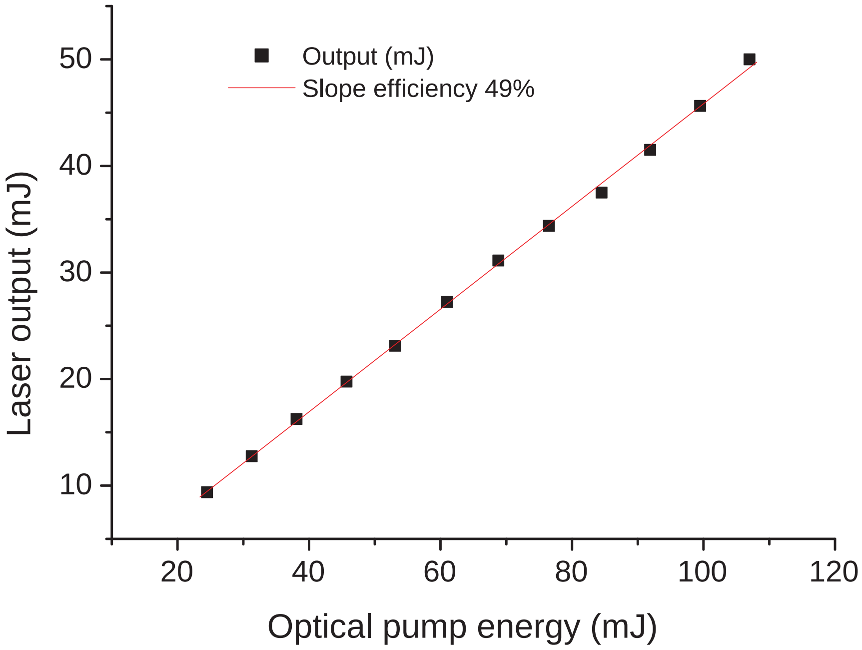

Figure 7.4: The multi-mode power output from the laser head when operated in standing wave configuration. The results shown are for a PRF of 800 Hz.

Most of the pump light that is not absorbed by the slab is incident on the opposing diode arrays, changing the temperature and hence wavelength of the pump light. For this reason, the temperature tuning of the laser diodes was optimised when the laser head was fully assembled, so as to maximise the 1064 nm output power of the laser.

7.3 Multi-mode performance of the high power laser head

To assess the performance of the laser head and to determine the maximum amount of laser power available for extraction, the laser was run in standing wave configuration with two mirrors placed close to the laser slab. One of the mirrors was a flat, max R and the other 2 m radius of curvature and a transmission of 90 %.

The output energy from the slave laser is shown plotted in Figure 7.4. As can be seen in this figure, a total of 50 mJ per pulse at 800 Hz was obtained from a pump energy of 107 mJ. The pump energy was not increased beyond the value shown in Figure 7.4 for fear of damaging the laser diode arrays.

7.3.1 The Mach-Zender interferometer

An accurate measurement of the thermal lens focal power within the laser crystal is essential for the design of a stable, efficient resonator. While the laser head was designed with the objective of minimizing thermal gradients, some thermal lensing is to be expected due to the non-uniform horizontal pump distribution within the slab. Measurements of the thermal lens were thus undertaken to asses the extent of the gradients.

Thermal lensing can be measured by shining a probe beam through the slab and detecting the shift in waist position [114], or by using interferometry [115]. A Mach-Zender interferometer was used because it gives an accurate measurement of thermal lens focal power and also provides a useful diagnostic for other thermal effects such as thermal wedging and non-uniform thermal contact between the slab and heatsinks and near field variations in heat, not seen in the far field.

A schematic of the measurment set-up is shown in Figure 7.5. It uses a helium-neon beam that is split into a reference and object beam; the latter passes through the laser slab and the former passes through a similar optical path length in air. The object beam accumulates phase changes from any differences in optical path length caused by inhomogeneities in refractive index which, when recombined with the reference beam, show up as a series of light and dark fringes from constructive and destructive interference. Hence temperature gradients within the slab can be directly measured by analysis of the fringe pattern recorded using a CCD. A lens was used to image the slab onto the CCD, thereby eliminating diffraction fringes from the slab aperture and providing magnification to make use of the full CCD array, which improves the resolution of images.

The measurement technique was tested using a lens of known focal length placed in front of the slab. In absence of these lenses no fringes were observed in the interferogram. Figure 7.6 shows interferograms for lenses of nominal focal lengths f = 100 cm and f = 50 cm.

The focal power of the thermal lens can be estimated by counting the number of fringes in the images in Figure 7.6. The focal length of the lens f is given by

$$f^2 \equiv R^2 = d^2 + (R - \Delta S)^2 \Rightarrow R = \frac{d^2}{2\Delta S} \tag{7.1}$$

where d is the aperture size as in Figure 7.7, R is the radius of curvature of the wavefront after the lens and ΔS, the sag, is measured by the interferometer by counting the number of fringes, with each fringe equivalent to a $\Delta S = 633 \times 10^{-9}$ m, the wavelength of the HeNe probe laser. The slab aperture in the horizontal direction is $d = 2.2 \times 10^{-3}$ m so, using Equation 7.1, if there were one fringe across the slab aperture, the focal length would be 3.8 m, for two fringes $f = 1.9$ m and so on. Using this analysis, the focal lengths

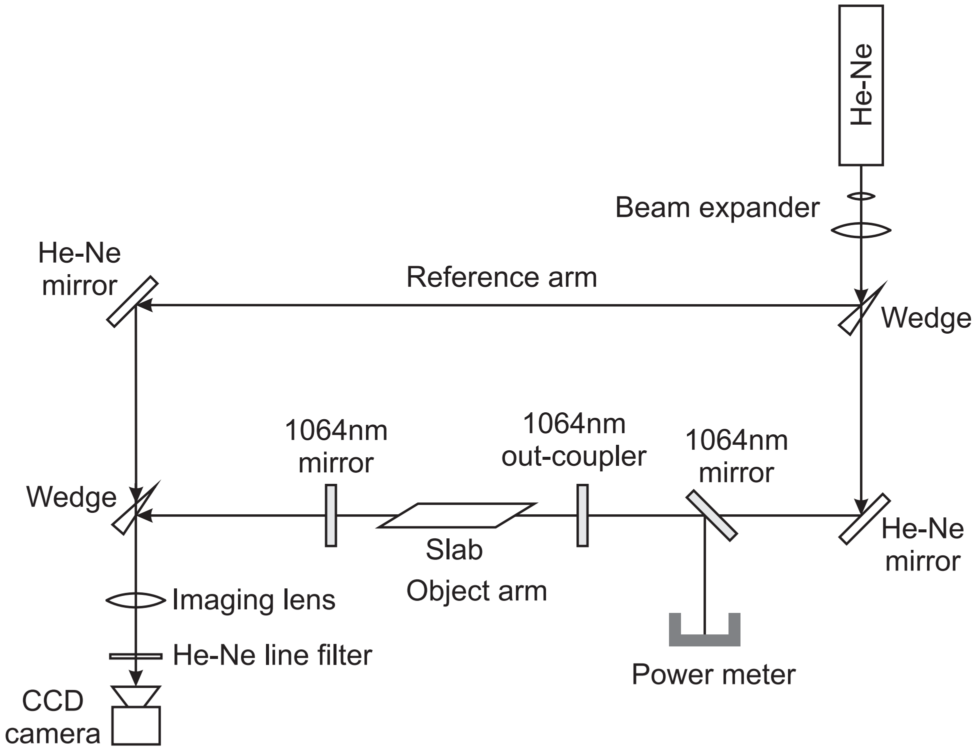

Figure 7.5: Schematic of the Mach-Zender interferometer used to measure thermal lensing and thermal distortion within the laser slab. The He-Ne beam is split into an object and reference arm, with object beam passing through the slab and the other passing through the same path length in air. When the beams are recombined, phase differences between the two wavefronts are detected as light and dark interference fringes on the CCD.

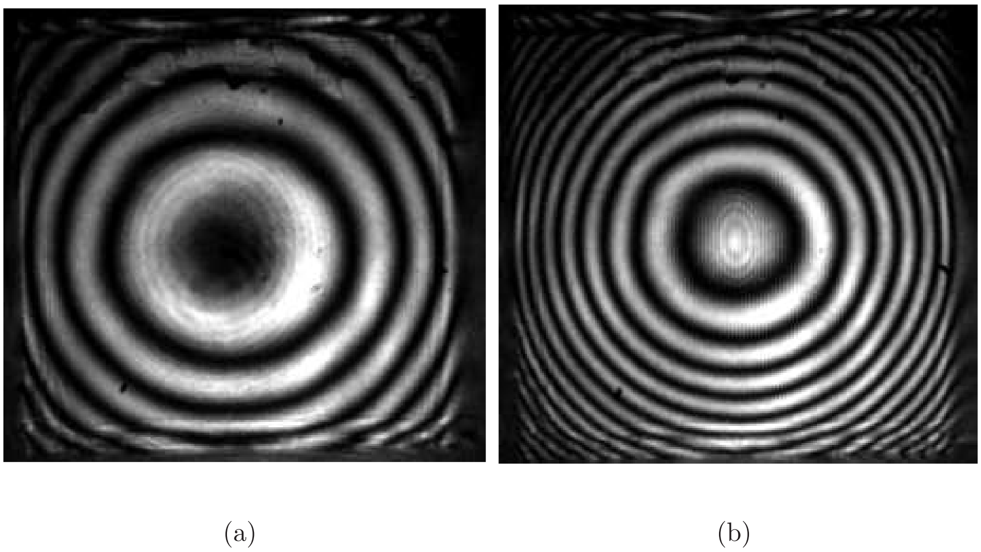

(a) (b)

Figure 7.6: Pictures showing the interference patern produced by placing a lens of focal length 100 cm (a) and 50 cm (b) in the object arm of the Mach-Zender interferometer.

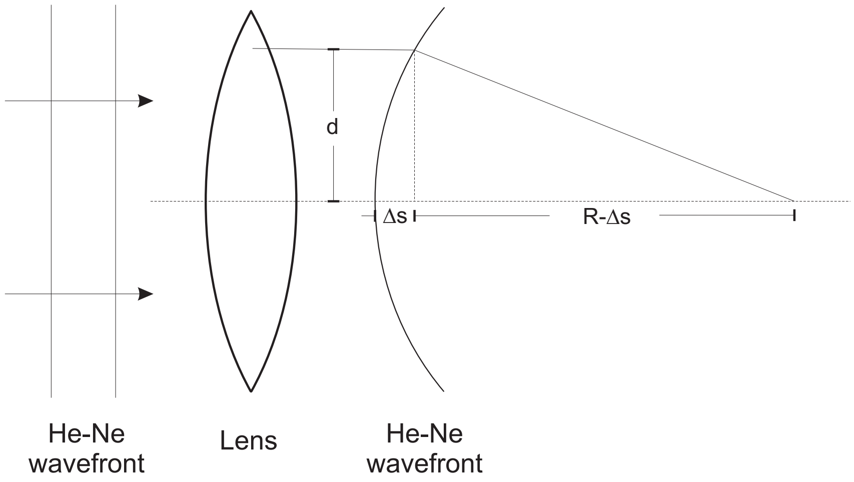

Figure 7.7: Diagram illustrating how the thermal lens can be estimated by counting the number of fringes in the interferogram. In this picture, the slab is represented by the lens with aperture width *d*. Wavefronts from the He-Ne probe beam are incident upon the lens and ΔS is measured by the interferometer.

of the lenses in Figure 7.6 can be estimated as being approximately 125 cm and 60 cm, which is close to their known values of 100 cm and 50 cm respectively.

Measuring the thermal lensing in this way provides useful visual information of thermal distortions over the whole slab aperture. For example, if there are hot and cold spots across the slab or a thermal wedge is present, this will be observed in the interference pattern. In the next section, a different analysis technique is presented which provides more accurate values for the thermal lens focal length (as it does not require human counting of fringes) but it does not provide visual information overm the whole slab aperture.

Interferograms of the laser slab were taken when pumping with average powers of 25 W, 40 W, 55 W and 70 W for 25 μs pump pulses at a repetition rate of 800 Hz. Typical measurements are shown in Figure 7.8. For these measurements the laser was not lasing. Measurements taken while the laser was running and a comparison between the two sets of data are presented in Section 7.3.2.

From these figures it can be seen that the centre of the thermal lens does not coincide with the centre of the slab, indicating that a thermal wedge is being formed within the gain medium. The lens centre drifts towards the top of the slab, indicating that the top is slightly cooler than the bottom. The reason for this could be due to the top surface of the slab being slightly larger in area than the bottom (212 mm^2 vs 194 mm^2) due to the tilt introduced to combat parasitic oscillations (see Section 6.3.4) or due to variations in thermal contact. The larger area in contact with the top heat sink would result in more effective cooling through this surface.

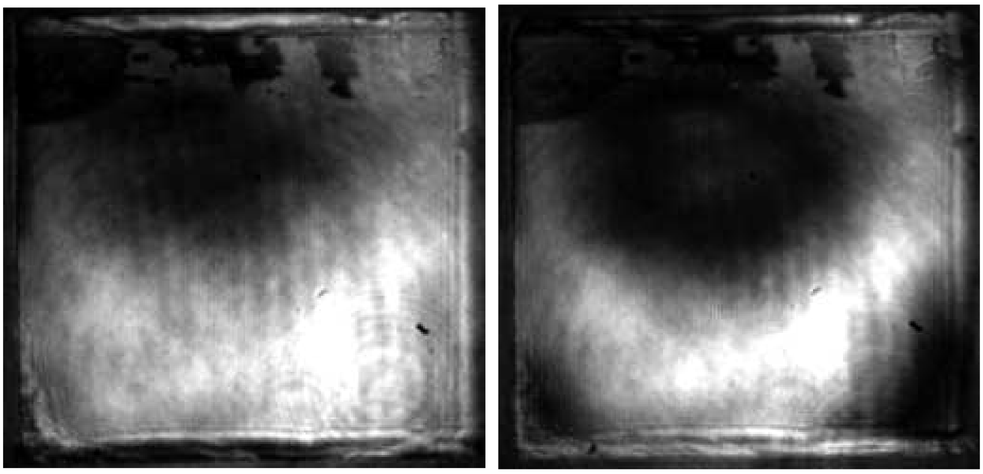

(a) 25 W, $f \approx 10$ m

(b) 40 W, $f \approx 6$ m

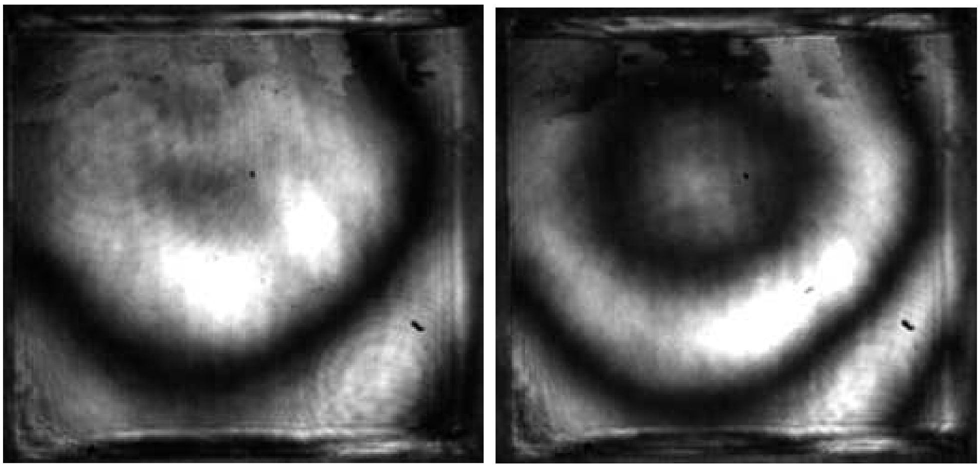

(c) 55 W, $f \approx 4$ m

(d) 70 W, $f \approx 3$ m

Figure 7.8: Interferograms of the laser slab under heat load when pumping with average powers of 25-70 W. The thermal lens focal length (stated beneath the figures) was estimated by counting fringes as described previously. A more accurate method of calculating the thermal lens value is presented in the next section. For these measurements the laser was not lasing.

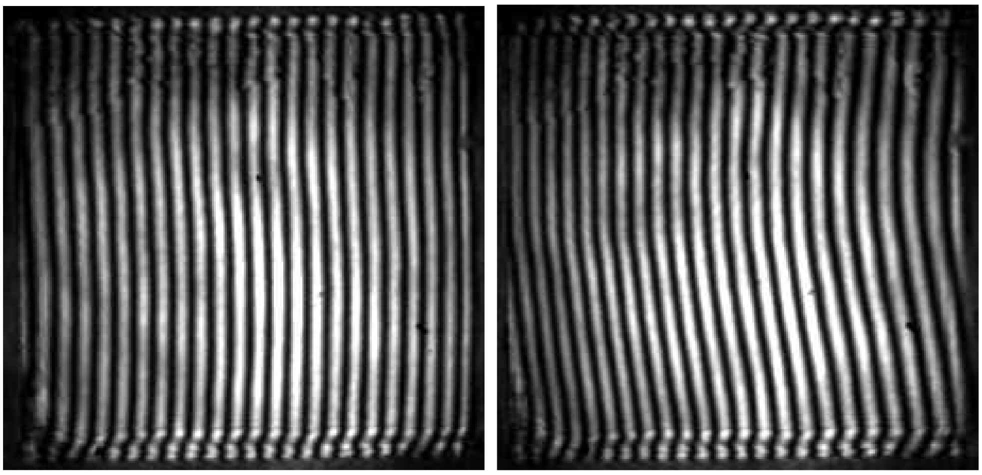

(a) 0 W pump (b) 70 W pump

Figure 7.9: Interferograms with a horizontal tilt in the reference arm mirror of the Mach-Zender interferometer.

7.3.2 Measurement of thermal focal power using a tilted wavefront

A more accurate measurement of the thermal focal power can be obtained by introducing a tilt in the reference arm, thereby creating an increased number of fringes and increasing the number of sample points across the wavefront.

Interferograms using a horizontal tilt in the reference arm mirror are presented in Figure 7.9. Figure 7.9(a) shows the slab with no heat load and Figure 7.9(b) is for an average pump power of 70 W. The image without heat load is used as a reference to subtract the effect of the tilt from the pumped image. This is accomplished by taking a 1-D slice thought the image, finding the maxima of the fringes and plotting the this data as shown in Figure 7.10(a). The slope of this plot is then subtracted from the data obtained from a slice through of the pumped image, giving the profile shown in Figure 7.10(b). This plot shows the change in phase across the slab aperture due to thermal distortion. The focal power of the lens is calculated by fitting a parabola of the form $a + c(x - b)^2$ and extracting the values of constants a, b and c, from which the focal power, f, can be calculated using[3]

$$f = \frac{1}{n\gamma \sin(\gamma L)} \tag{7.2}$$

---

[3] the focal length is given by $f = -\frac{1}{C}$ where C is the [2,1] (second row, first column) element of the ABCD matrix of a Gaussian lens duct representing the laser slab [88].

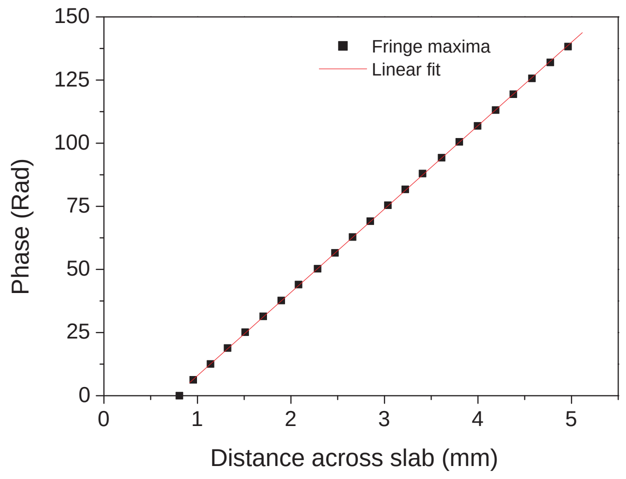

(a) 0 W pump

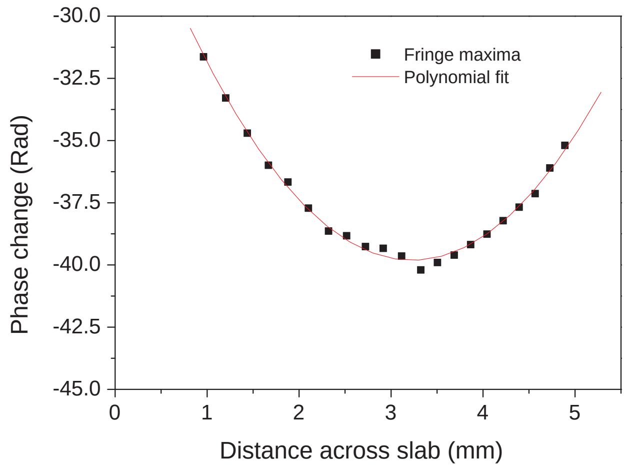

(b) 70 W pump

Figure 7.10: Plots showing the maxima of interference fringes from Figure 7.9. Part a) is with no pumping, and the slope of this plot is subtracted from part b) to remove the phase change introduced by the tilt. A parabola is fitted to part b) and used to calculate the value of the thermal lens.

Pump Power (W)	not lasing		lasing	
	f_h (m)	f_v (m)	f_h (m)	f_v (m)
25	13.7	27.1	18.3	48.4
40	6.0	9.5	8.5	11.2
55	4.2	5.5	5.8	9.5
70	3.1	4.2	3.7	5.2

Table 7.3: Measurements of the thermal lens in the horizontal, f_h and vertical, f_v directions for various pump powers. Measurements were taken when the slab was lasing (in multi-mode configuration) and also when not lasing.

where n is the refractive index of Nd:YAG (1.82), L is the length of the slab and

$$\gamma = \sqrt{\frac{c\lambda}{\pi L n}} \tag{7.3}$$

Measurements of the thermal lens focal lengths were taken with and without lasing. When lasing, a flat mirror and flat outcoupler were placed on either side of the slab as in Figure 7.5. For the not lasing measurements, these mirrors were removed. The results of the thermal lens measurements for both cases are presented in Table 7.3. The results show that the thermal focal power was around 20 % lower when the laser was lasing due to additional heat being removed by optical power when lasing. This value is consistent with the results of other groups [61]. The fact that the thermal lens is different when lasing in a multimode cavity (compared to when not lasing) also sugests that the thermal lens will be different when lasing TEM_{00}, see below.

Importantly, Table 7.3 show that the thermal lensing is weak and relatively symmetric in horizontal and vertical directions (the vertical direction is around 20 % weaker for high pump powers when the lens is significant). As was discussed in Chapter 5, a weak, symmetric thermal lens is essential for the simple, efficient incorporation of the laser head within a long, stable TEM_{00} resonator.

7.4 Injection mode-locked laser performance

7.4.1 Resonator design

The proof of principle laser described in Chapters 3 and 4 used a resonator designed for dynamic stability whereby the beam size in the laser slab was made insensitive to changes in the thermal lens focal length, as detailed in Section 3.1. While the proof of principle laser was operated only at low average power and so would not benefit significantly from

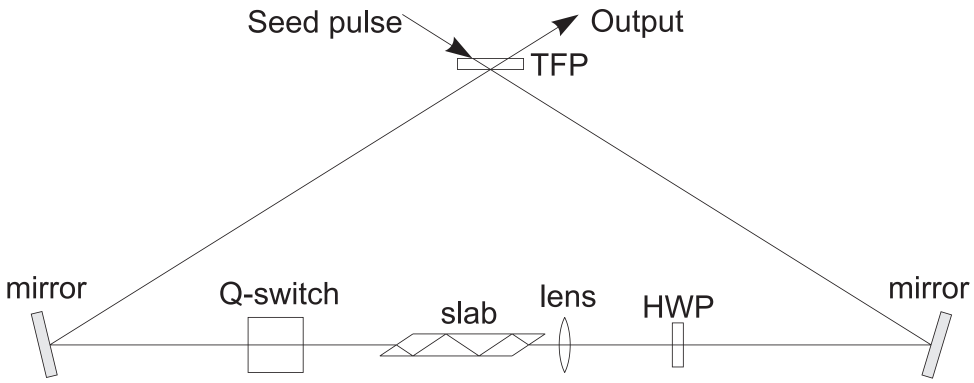

Figure 7.11: Resonator design for the injection mode-locked slave laser showing the single intra-cavity spherical lens used to compensate the thermal lens within the slab. The round trip length was made 4.2 m for dynamic stability as before.

the dynamic stability, the tests showed that the long resonator was simple to align and had good long term stability and efficiency. It was therefore decided to use the same resonator design for the high power laser(Figure 7.11). The only difference between the two lasers is the stronger thermal lensing measured in the high power laser due to the increased average pump power. As reported in the preceding section, the thermal focal length in the slab at 70 W pump power when lasing multimode is around $f = 4.5$ m (average of f_h and f_v). The effect of this lens can be compensated by altering the intra-cavity lens required for stability. If there was no thermal lensing, the value of this lens should be $f = 2.1$ m (half the round trip length) to make the trace of the resonator's round trip ABCD matrix zero as required for optimum stability. But with the thermal lens reported above, the value of this lens should be lengthened to $f = 3.9$ m to compensate.

High quality spherical lenses are available off-the-shelf with focal lengths of $f = 1$ m, 1.5 m, 2 m, 5 m and 10 m [60]. Using a combination of the longer focal length lenses can provide intermediate values.

When the resonator was assembled and tested in TEM$_{00}$ operation, it was found experimentally that an intra cavity lens of f =1.5 m was most effective, producing higher average powers and slope efficiencies than either the 1 m or 2 m lenses (performance results are presented in the next section). The reason for the difference between predicted and experimentally determined lenses can be attributed to a combination of two effects. Firstly, there are different thermal conditions present when running in TEM$_{00}$ mode as compared to the multimode conditions for which the thermal lens was measured (Section 7.3.2). In TEM$_{00}$ mode, less power is extracted from the wings of the slab, resulting in a hotter sides and a reduced thermal lens focal length. When lasing multimode with a flat-flat resonator design, there is more power extracted from the sides (where the pump density is highest) compared to the centre so a stronger lens was measured in Section 7.3.2. The long length of the ring resonator (4.2 m) made thermal lens measurements difficult when running a TEM_{00} mode due to fringe stability issues arising from the long object and reference arms. These measurements were not performed.

Another aspect that can affect the optimum focal length of the intra-cavity lens is the size of the beam passing through the slab. Modelling shows that an intra-cavity lens with with a focal length of 1.5 m will produce a slightly larger mode size within the slab than a lens with $f = 2\ m$. This could result in a more efficient sweep out of the laser gain and give higher output power.

7.4.2 Injection mode-locked laser power at 800 Hz PRF

A plot of the output from the injection mode-locked slave laser is presented in Figure 7.12, showing a maximum output energy of 12 mJ per macro-pulse is obtained at a PRF of 800 Hz. This equates to an average power of 9.4 W and ranks as one of the highest average powers reported for a single mode electro-optically Q-switched Nd:YAG laser system in a stable cavity. Other authors of similar, high average power systems have reported powers of 15 W [63], 11 W [64] and 10 W [62].

For pump powers higher than the maximum value displayed in Figure 7.12, the output of the slave laser was seen to roll off and was limited to 12 mJ. This is thought to be due to the thermal lens drifting towards the top heat sink of the slab as shown in Figure 7.8, from improper thermal contacts. One way to correct for this occurance is to have independent temperature control of the top and bottom heat sinks of the slab. This modification remains for future work.

The average power recorded from the 1064 nm laser is sufficient to satisfy two of the three power scaling design options presented in Section 2.6. The design options discussed in Section 2.6 were: using a MOPA to boost the average power of the slave oscillator to 50 W; having a system of five 10 W 589 nm laser systems that each generate one of the five beacons required for MCAO, and, having a single oscillator produce the entire 50 W in one step. The 1064 nm slave laser described in this chapter can meet the average power requirements of the first two of these design options.

7.4.3 Reproducibily of slab mounting

The maximum average power produced by the laser varied on successive rebuilds of the head. The variations were caused by the thermal contact between the Nd:YAG and heat sinks. As described in Section 6.4, indium foil was placed between the N:YAG and the

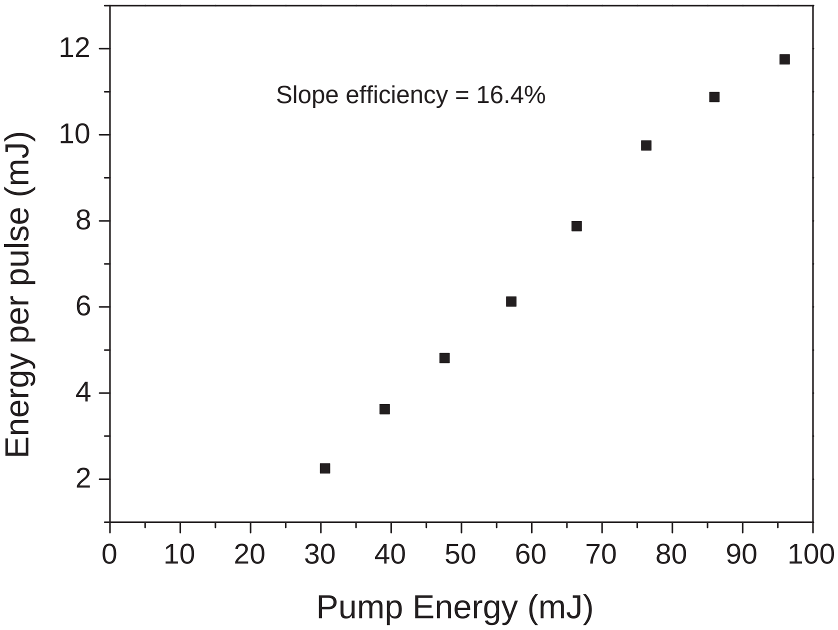

Figure 7.12: A plot of the injection mode-locked Q-switched single-transverse-mode output from the high power oscillator. These measurements were taken at a PRF of 800 Hz and show that a maximum average power of 9.4 W was obtained with a slope efficiency of 16.4 %.

copper heat sink to improve thermal contact. Any irregularities in indium thickness or the copper clamping pressure/uniformity will affect the performance. On successive rebuilds the laser produced 8.0 W, 3.3 W, 7.6 W, 9.4 W, 3.2 W and 8.0 W of injection mode-locked average power. 9.4 W was the maximum obtained and the results are plotted in Figure 7.12.

During each rebuild, the assembly technique was refined slightly to try to improve performance. Some of the experimentations performed were: bringing the top heat sink down squarely using a height feeler gauge; clamping the slab with a single screw pushing down on the centre of the top heat sink; rolling the indium first onto the slab and then crushing with the copper blocks. The final assembly technique was described in Section 6.4.

Experiments were also conducted with the indium. It was observed that when the indium is heated to close to its melting point (157°C) it becomes softer than at room temperature. It was hoped that this would help the indium flow into inhomogeneities of the slab/copper interface and reduce thermal impedance of the laser head. To test this hypothesis, the assembled laser head was heated in an oven to 152°C and held at this temperature for 4 hours. Unfortunately, this warped the laser head structure so that the top copper heat sink no longer slid down freely on the locating pins (Figure 6.12). Since heating, the laser head could not reproduce its former performance and the average power was limited to 2-5 W.

7.4.4 Q-switched pulse stretching

Q-switched pulse stretching was successfully demonstrated with the proof of principle laser by driving the Q-switch with a tailored high voltage waveform so as to vary the lasers output coupling fraction and control the build-up of the giant pulse. This technique was used to stretch the duration of a 10 mJ macro-pulse from 400 ns to 1.8 μs. The test laser was operated at 50 Hz PRF, but scaling the repetition rate is not expected to be a problem as the high voltage circuit was shown to work reliably at 800 Hz and the BBO Pockels cell did not show any ringing at this higher frequency.

It was observed, however, that the commercial QCW power supplies used to drive the laser diode arrays exhibited an un-expected variation in pulse width as shown in Figure 7.13. The variation in width was measured to be 1.5 μs, representing a 6 % variation in pump energy from the laser diodes. This variation has a large effect on the build up time of the giant pulse and consequently distorts the stretched macro-pulse shape as shown in Figure 7.14, as the level shift between low and high outcoupling fraction (time $t1$ in Figure 4.8) was triggered at a fixed time after the start of the Q-switch drive pulse. The observed variation in stretched macro-pulse shape is clearly not acceptable as it will

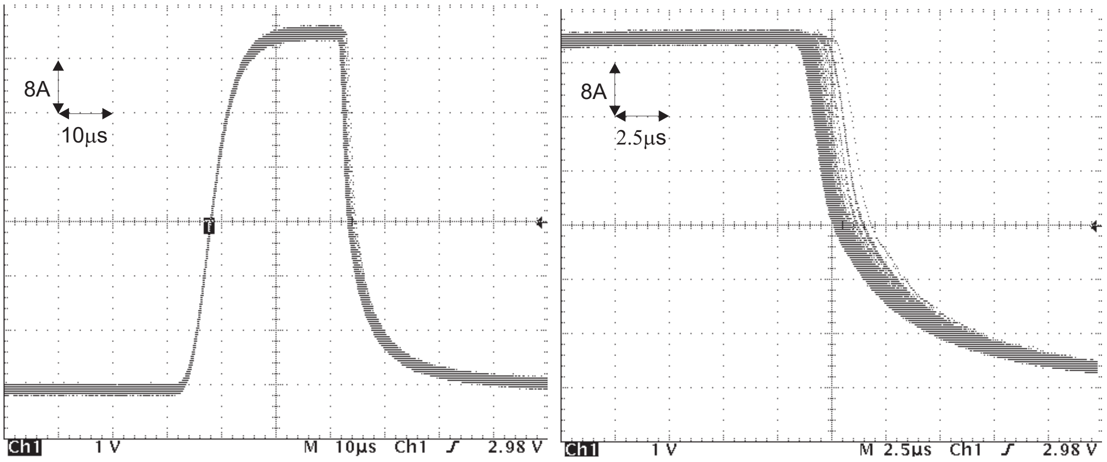

(a) (b)

Figure 7.13: Overlay of multiple current pulses from the laser diode driver (a). The measurement was taken with an oscilloscope set to trigger on the front edge of the pulse and the width of the back edge (b) shows the deleterious variation in pulse width.

reduce SFG efficiency from the mismatch between 1064 and 1319 nm macro-pulse shapes and could result in damage to intra-cavity optics if the giant pulse is allowed to build up too high before outcoupling.

This problem is caused by a fault in the laser diode driver control system and the manufacturer has agreed to attempt to fix the problem if the units are returned.

7.4.5 Beam quality measurement

Good beam quality is essential for guide star lasers at 589 nm as it enables a tight focus of the beam in the sodium layer, creating a bright, near-point-source beacon that can be detected by the wavefront sensor in the adaptive optics system with maximum signal-to-noise ratio. This minimizes the total average power required of the guide star laser source. Good beam quality is also essential for high SFG efficiency as it enables a tighter focus inside the SFG crystal, giving high peak powers. To achieve good beam quality at 589 nm, the 1064 nm and 1319 nm lasers must have good beam quality.

Laser beam quality can be measured using Hartmann or Shack-Hartmann wavefront sensors [116], by measuring the transmission through a mode-matched passive optical cavity [117] or by the approach recommended by the ISO Standard 11146 where the spot size of the beam is recorded at a focus and at points beyond the Rayleigh range. It was decided to use the later approach as this technique offers an accurate measurement using a simple experimental setup.

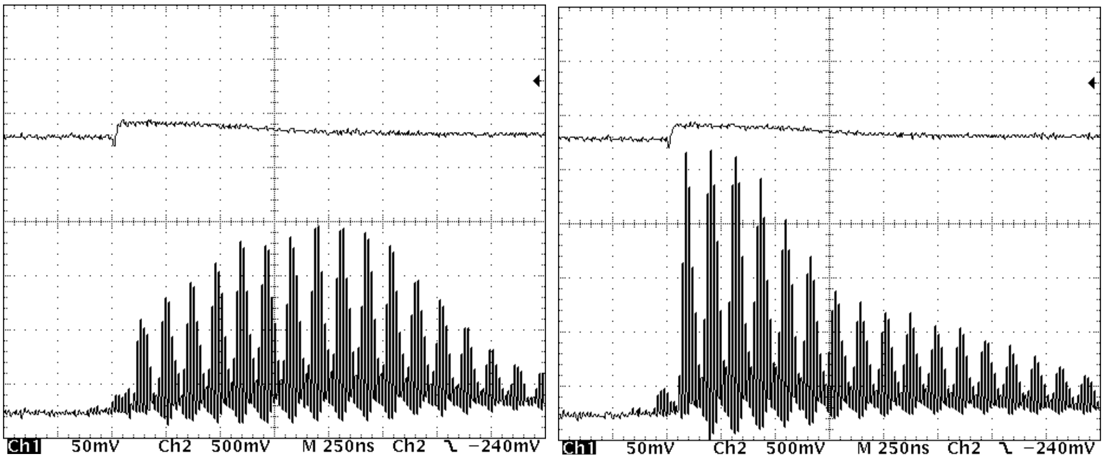

(a) (b)

Figure 7.14: Variation in the stretched macro-pulses (lower trace) resulting from the pump pulse-width jitter. The upper trace shows part of the Q-switch drive waveform. These are single-shot measurements recorded using a digital oscilloscope and some aliasing is present due to insufficient sampling of the micro-pulses. The overall pulse shape can still be observed in these figures, however.

The injection mode-locked output of the slave laser was focused to a waist as depicted in Figure 7.15 and the spot-size of the beam was sampled at multiple points both around the waist region and outside the Rayleigh range. The beam propagation factor, M^2, can then be obtained by fitting a curve of the form

$$\omega(z)^2 = \omega_0^2 + \theta^2 z^2 \tag{7.4}$$

and using the fit to obtain values of the waist spot-size, ω_0, and far field divergence angle, θ. The beam propagation factor, M^2, can then be calculated using

$$M^2 = \frac{\omega_0 \theta \pi}{\lambda} \tag{7.5}$$

For increased accuracy, the spot-size of the beam should be sampled at many points; at least five times within the Rayleigh range to obtain an accurate value for ω_0 and at least five times at $> \pm 2$ Rayleigh ranges to obtain an accurate value of θ.

The definition of spot-size used in Equations 7.4 and 7.5 assumes a near-gaussian profile with $\omega(z)$ being the radius that encloses $1/e^2$ or 86.5 % of the beam energy. For beams that are far from diffraction limited, the $1/e^2$ definition of spot-size becomes less meaningful and alternative definitions can be used [118]. Since the laser beam in this case has a Gaussian intensity shape (see results section) the $1/e^2$ definition was adopted.

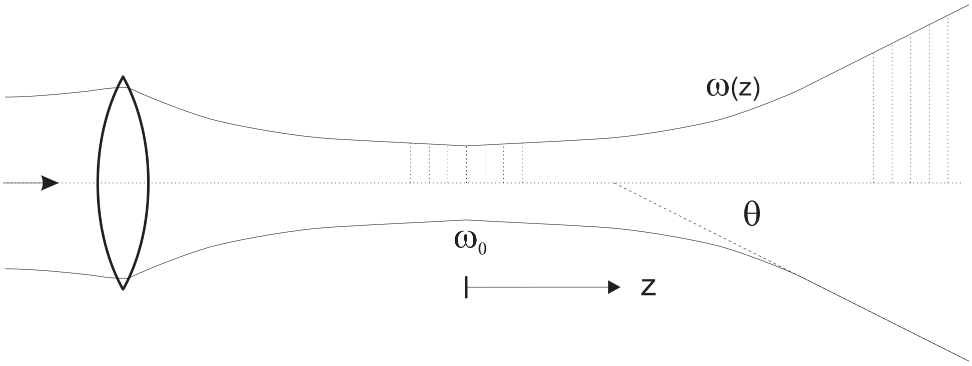

Figure 7.15: To measure the beam quality of the slave laser, the beam is focused by a lens and the spot-size, $\omega(z)$, is measured at various location, z. For greatest accuracy, multiple measurements should be taken near the waist (ω_0) and in the far field.

Avg. Power	M_x^2	M_y^2
2 W	1.05±0.05	0.98±0.05
7 W	1.05±0.05	1.02±0.05

Table 7.4: Measurements of beam quality for the injection mode-locked slave laser showing near-diffraction limited performance in both x- and y-directions. The measurement uncertainty is due to the accuracy of the translation stage used to measure the beam waist.

The spot-size was measured by translating a knife-edge across the beam and recording the distance travelled to block 10 % then 90 % of the beam power and multiplying this value by 0.781 to obtain the spot-size [119].

Measurements of the injection mode-locked slave laser beam quality were recorded at output power levels of 2 W and 7 W. Plots of the spot-size data, together with a least squares fit to the data using Equation 7.4 are displayed in Figure 7.16.

The beam propagation factor, M^2, was measured independently for the x and y-axes (horizontal and vertical respectively) and the results are summarized in Table 7.4. The near-diffraction-limited beam quality measured for both axes at the high power levels stated in Table 7.4 shows that the laser performs in excess of the requirement set for advanced guide star sources ($M^2 < 1.2$).

7.4.6 Laser bandwidth measurements

As in Section 3.6.4, bandwidth control of the high power injection mode-locked slave laser was measured by injecting a variable-width seed pulse and recording the bandwidth of the output using a scanning Fabry-Perot interferometer. The Fabry-Perot recordings were

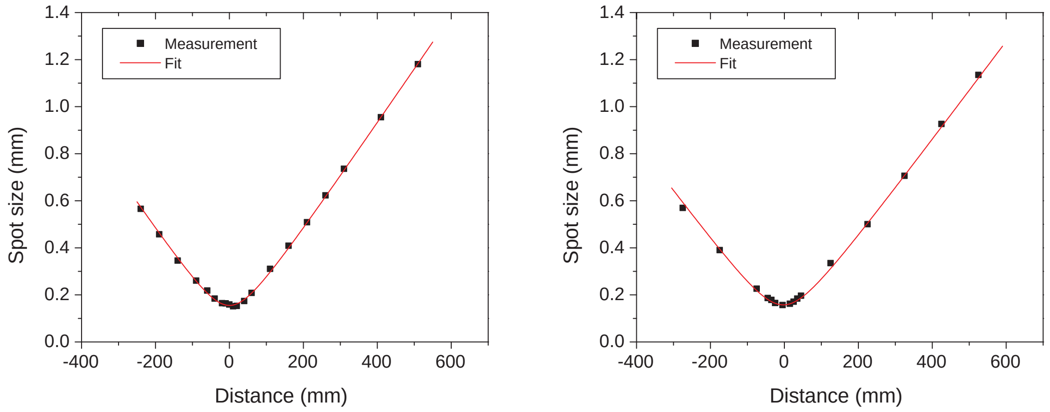

(a) 2 W, $M_x^2 = 1.05$

(b) 2 W, $M_y^2 = 0.98$

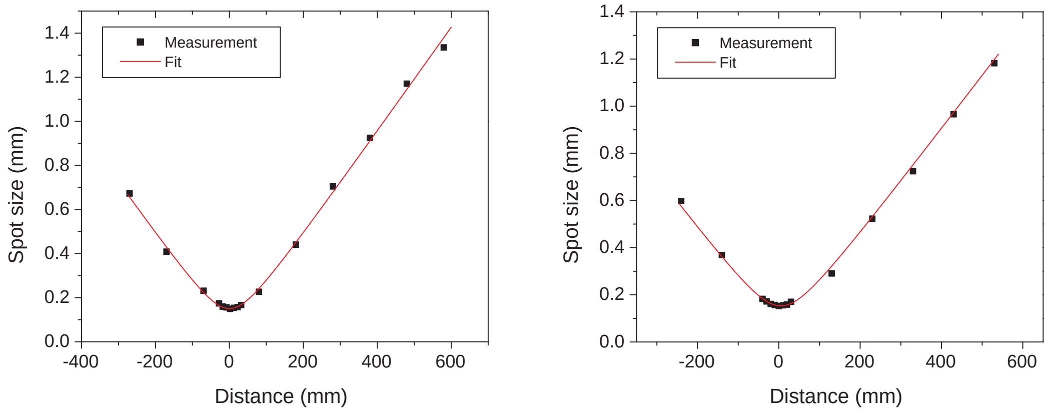

(c) 7 W, $M_x^2 = 1.05$

(d) 7 W, $M_y^2 = 1.02$

Figure 7.16: Measurement of laser beam quality showing the measured points and a least squares fit to the data.

integrated over many macro-pulses, giving spectra as shown in Figure 7.17. The results are summarized in the plot of Figure 7.18(a).

Comparing these results with the low power laser head (Figure 7.18(b)), we see good agreement, with a time bandwidth product 0.91 in each case. The range of bandwidth measurements was extended in Figure 7.18(a) by generating seed pulses of width 1.99-2.67 ns by swapping HV pulsers in the pulse slicer. Previously (Section 3.4), the 1 ns HV pulser was used to drive the first Pockels cell (creating the leading edge of the seed pulse) then the 2.7 ns HV pulser created the trailing edge of the seed pulse using the second Pockels cell. Hence the maximum seed pulse width was 1 ns (the length of the drive pulse to PC1) resulting in a minimum bandwidth of 840 MHz. Longer seed pulses were obtained by swapping the HV drivers, giving the narrower bandwidths in Figure 7.18(a).

The narrower bandwidths in Figure 7.18(a) may be beneficial for the final guide-star laser if sodium bleaching is not significant for the given pulse format and power level. Either way, the broad range of bandwidths achievable and the ability to adjust the bandwidth to maximise photon return makes the injection mode-locked laser system ideally suited to guide star applications.

7.5 Conclusions

This Chapter presented the results of a new high-average-power injection mode-locked slave laser, optimised for efficient SFG and advanced guide star laser systems. The laser uses a side pumped, conduction cooled Nd:YAG slab design and was able to demonstrate power levels of up to 10 W with near-diffraction limited beam quality. The lasers spectral-width was shown to be adjustable over a range of 0.36-2 GHz by controlling the width of the injected seed pulse. These properties, combined with the inherent low timing jitter and wavelength control of injection mode-locking, demonstrate that the laser design is able to meet all requirements of the 1064 nm slave oscillator for advanced SFG guide star systems on ELT's. A power amplifier is planned to follow the slave oscillator to boost the power levels to 50 W as discussed in Chapter 2.

One remaining issue is the fault discovered in the commercial laser diode drivers. It was found that substantial pulse jitter exists in the current pulses produced by these devices. This prevented the use of Q-switched pulse stretching due to the variation in build up time of the giant pulse. The pulse stretching technique of Chapter 4 was, however, demonstrated with macro-pulses of the same energy as reported in this Chapter and the pulse stretching electronics is capable of running at an 800 Hz PRF, so pulse stretching

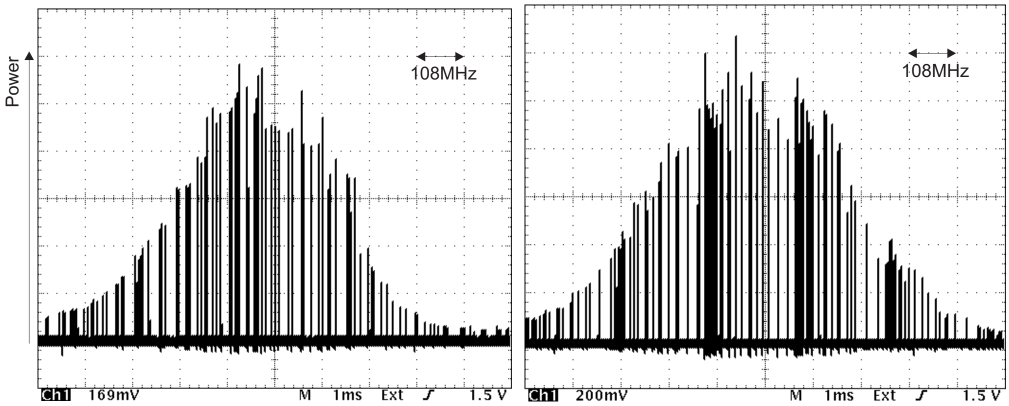

(a) 364 MHz (b) 466 MHz

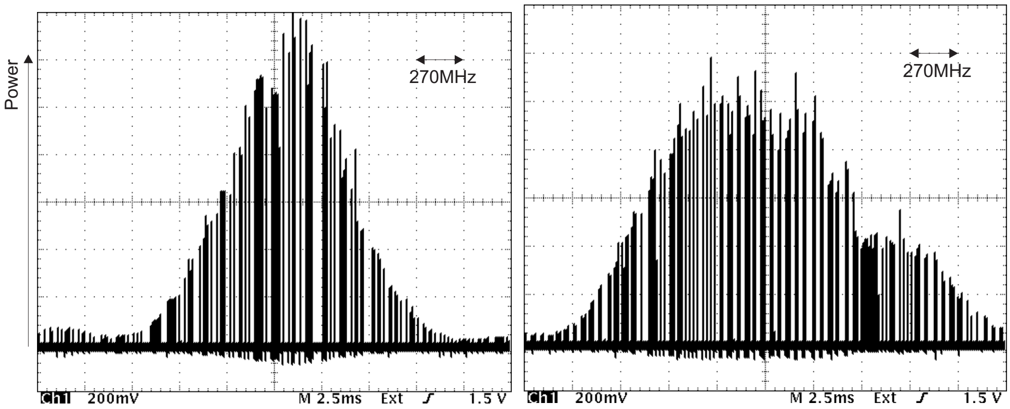

(c) 842 MHz (d) 1423 MHz

Figure 7.17: Measurements of bandwidth of the slave laser output taken with a scanning Fabry-Perot interferometer. One horizontal division represents 108 MHz in part a) and b) and 270 MHz for part c) and d). The gaps seen in the spectra are due to the limited sampling rate of the oscilloscope used to record the measurements. The stated bandwidth (BW) is the FWHM of a Gaussian fit to the data. The duration of the injected seed pulse was 2.7 ns for part a) 2.2 ns for b), 1.1 ns for c) and 0.6 ns for part d).

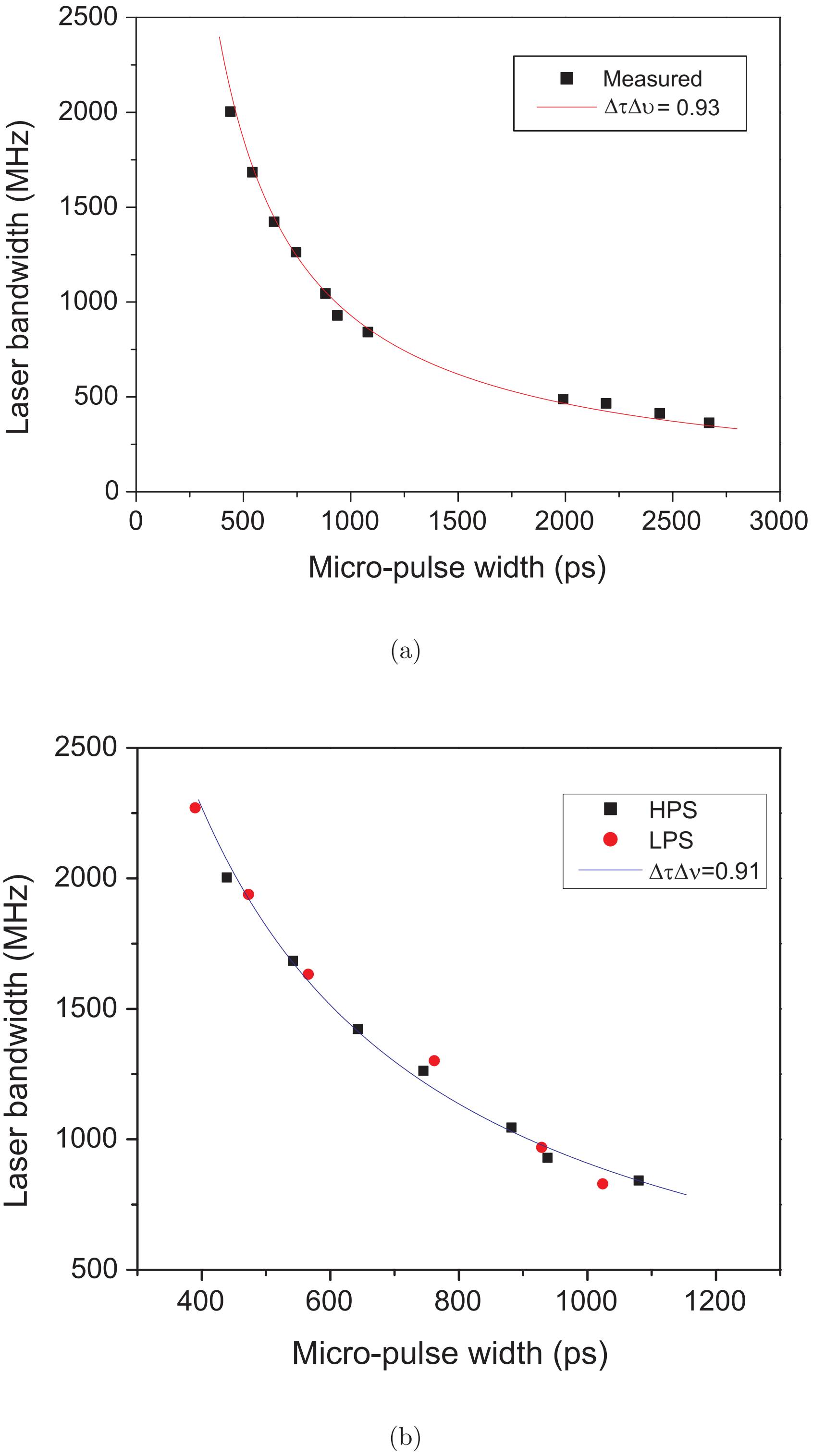

(a)

(b)

Figure 7.18: Plots showing the range of bandwidth tunability of the high power injection mode-locked oscillator. Part a) shows the full range of bandwidth tuning while part b) shows the high power slave measurements (black) overlaid with the measurements from the low power slave (red) with the same measurement range as Figure 3.17

is not expected to be a problem if a suitable replacement driver is obtained.

Chapter 8

Conclusions

This thesis presents the design and development of a new type of guide star laser source, capable of producing a pulse burst waveform that can essentially meet all of the requirements for next generation adaptive optics systems. The pulse burst contains short duration micro-pulses whose width can be adjusted to set the lasers bandwidth and the Q-switched macro pulse duration is optimised to avoid star elongation and reduce sodium bleaching. The 1064 nm experiments presented in this thesis have proven that the design works, in that the lasers spectral requirements can be achieved, and the average power can be scaled to a level that is sufficient to produce a guide star system composed of five subscale (10 W) systems, or to saturate an amplifier stage to boost the average power to the required 50 W.

Details of the laser system design were presented in Chapter 2. The design uses SFG of 1064 nm and 1319 nm Nd:YAG lasers to achieve the sodium wavelength and includes the novel concept of injection mode-locking as a robust way to control the lasers wavelength, bandwidth and timing for SFG. The design uses a new ring resonator, which allows both injection mode-locking and efficient Q-switched pulse stretching. The high peak power and low timing jitter of the short micro-pulses allow a simple, efficient single pass SFG stage to be used, simplifying the design.

A low average power injection mode-locked 1064 nm laser was assembled to test key design features and the results of these experiments were presented in Chapter 3 and published in ref. [32]. The seed pulses for injection mode-locking were produced using a double Pockels cell switch that was capable of producing short duration pulses with a variable duration ranging from 0.3 to 2.7 ns. The wavelength of the seed pulse is used to set the wavelength of the slave laser which can be locked to the sodium absorption line. The width of the seed pulse is adjusted to match the lasers spectral bandwidth to the Doppler broadened linewidth of atmospheric sodium.

A new method for stretching the duration of Q-switched laser pulses was described in Chapter 4. The method uses a tailored high voltage waveform to drive the Q-switch which rapidly varies the resonator outcoupling fraction to slowly release the energy stored in the gain medium and lengthen the output pulses. This technique is facilitated by a novel ring resonator design that uses all modulated energy as the laser output, thus enabling near-unity efficiency to be achieved by this technique. Furthermore, the rapid control of the outcoupling enabled shaping of the macro-pulses and flat-topped pulses were generated that were stretched by a factor of 4.5 to 1.8 μs.

Chapters 5, 6 and 7 presented the design, construction and development of a new high average power Nd:YAG laser head, optimised for use in the guide star system. The design uses a zigzag Nd:YAG laser slab, pumped from each side by a pair of un-collimated laser diode arrays. The diode light is transported to the slab via a custom built, low-loss waveguide that mixes up the pump light to reduce inhomogenaeities and condenses the light to match the slab aperture. The pumping and cooling geometry was selected to minimize thermal distortions within the slab and enable scaling to high average powers. Measurements of the thermal lensing under pumping showed that the thermal focal length was kept low, enabling the simple integration of the laser head into a long length resonator. Injection mode-locking was demonstrated with this laser for a PRF of 800 Hz as required of the final guide star design. The lasers spectral control was seen to be identical to the lower PRF proof of principle laser and bandwidth measurements were taken showing adjustability over a useful range of 0.36 - 2 GHz. Power scaling experiments showed that this laser was capable of generating a maximum output of 10 W with an injection mode-locked pulse burst at 800 Hz PRF with near diffraction limited beam quality. This power level is comfortably sufficient to saturate an amplification stage to further boost the average power to the 50 W level required by the system design.

Further work is currently in progress to develop the 1064 nm system, reported in this thesis, into a complete field deployable unit that can be operated remotely at a large aperture observatory. This work includes the replication and optimisation of the laser for 1319 nm operation. This task will involve replacing the 1064 nm resonator optics with optics coated at 1319 nm and conducting experiments to determine the maximum output available at 1319 nm using the current slab and resonator design. Modifications may have to be made to the laser slab and resonator design to boost the gain if it is found that there is insufficient energy produced at this wavelength. The high average power MOPA and SFG stages also remain for future work, although a discussion of design options were presented in Chapter 2. Finally, to complete the laser system, the laser must be adapted for automated control and undergo extensive reliability and field testing. Detailed designs and proof of concept experiments for these systems remain to be done, but some work has already been demonstrated by previous authors, including the realization of high average power MOPAs [69], SFG [18] and remotely operated Nd:YAG systems [19].

Appendix A

Publications

Several papers were prepared for publication in peer reviewed journals from material directly related to the work presented in this thesis. This section presents copies of these papers for the readers convenience.

The papers contained in this section are:

- T. P. Rutten, P. J. Veitch, C. d'Orgeville and J. Munch, "Injection mode-locked guide star laser concept and design verification experiments," Opt. Express vol. 15 (5), pp. 2369-2374 Mar. 2007.
- T. P. Rutten, N. Wild and P. J. Veitch, "Fast rise time, long pulse width, kilohertz repetition rate Q-switch driver," Rev. Sci. Instrum. vol. 78, 073108 Jun. 2007.
- T. P. Rutten, P. J. Veitch and J. Munch, "Efficient pulse stretching of Q-switched lasers," IEEE J. Quantum Electron. vol. 44 (10), pp. 911-915 Oct. 2008.
- J. Munch, T. P. Rutten, N. Simakov, M. Hamilton, C. d'Orgeville and P. Veitch, "A new guide star laser using optimized injection mode-locking," Proc. SPIE, vol. 7015, June 2008

Injection mode-locked guide star laser concept and design verification experiments

Thomas P. Rutten[1], **Peter J. Veitch**[1], **Céline d'Orgeville**[2] **and Jesper Munch**[1]

[1]*Department of Physics, The University of Adelaide, Adelaide SA 5005, Australia*
[2]*Gemini Observatory, Colina el Pino s/n, Casilla 603, La Serena, Chile*
jesper.munch@adelaide.edu.au

Abstract: Injection mode-locking combined with stretched Q-switching of a ring resonator are proposed and demonstrated as a promising approach for advanced, guide star lasers. The concept uses two Nd:YAG lasers, producing a macro-micro pulse-burst output, optimized for efficient sum-frequency generation. We demonstrate wavelength, bandwidth and timing control required to maximize the atmospheric Na fluorescence.

OCIS codes: (140.3580) Lasers, solid-state; (010.1080) Adaptive optics.

References and links

1. P. W. Milonni, “Resource letter: AOA-1: Adaptive optics for astronomy,” Am. J. Phys. **67**, 476 (1999).
2. N. Ageorges and C. Dainty, *Laser Guide Star Adaptive Optics for Astronomy* (Kluwer Academic Publishers, 2000).
3. N. Hubin, B. L. Ellerbroek, R. Arsenault, R. M. Clare, R. Dekany, L. Gilles, M. Kasper, G. Herriot, M. Le Louarn, E. Marchetti, S. Oberti, J. Stoesz, J. P. Veran and C. Vérinaud, “Adaptive optics for Extremely Large Telescopes,” in *Proceedings IAU Symposium No. 232*, 60-85 (2005).
4. R. Foy and A. Labeyrie, “Feasibility of adaptive telescope with laser probe,” Astron. Astrophys. **152**, 29 (1985).
5. Requirements from Gemini RFP no. N231397, Dec. 2003.
6. C. E. Max, K. Avicola, J. M. Brase, H. W. Friedman, H. D. Bissinger, J. Duff, D. T. Gavel, J. A. Horton, R. Kiefer, J. R. Morris, S. S. Olivier, R. W. Presta, D. A. Rapp, J. T. Salmon and K. E. Waltjen, “Design, layout, and early results of a feasibility experiment for sodium-layer laser-guide-star adaptive optics,” J. Opt. Soc. Am. A. **11**, 813 (1994).
7. T. H. Jeys, A. A. Brailove and A.Mooradian, “Sum frequency generation of sodium resonance radiation,” Appl. Opt. **28**, 2588 (1989).
8. A. Tracy, A. Hankla, C. Lopez, D. Sadighi, N. Rogers, K. Groff, I. McKinnie and C. d'Orgeville, "High-Power Solid-State Sodium Beacon Laser Guidestar for the Gemini North Observatory," Proc. SPIE **5490**, 998-1009 (2004).
9. D. M. Pennington, R. Beach, J. Dawson, A. Drobshoff, Z. Liao, S. Payne, D. Bonaccini, W. Hackenberg and L. Taylor, “Compact fiber laser approach to generating 589 nm laser guide stars,” in *Proceedings of Conference on Lasers and Electro-Optics Europe*, 730 (2003).
10. D. Bonaccini Calia, W. Hackenberg, C. Araujo, I. Guidolin and J. L. Alvarez, "Laser guide star related activities at ESO," Proc. SPIE **5490**, 974-980 (2004).
11. E. J. Kibblewhite and F. Shi, “Design and field test of an 8 watt sum-frequency laser for adaptive optics,” Proc. SPIE **3353**, 300-309 (1998).
12. Response to Gemini RFP no. N231397, Jan 2004.
13. T. P. Rutten, P. J. Veitch and J. Munch, “Development of a Sodium Laser Guide Star for Astronomical Adaptive Optics Systems,” presented at the *Australasian Conference on Optics, Lasers and Spectroscopy*, Rotorua, New Zealand, 5-9 Dec. 2005.
14. A. J. Alcock, P. B. Corkum and D. J. James, “A simple mode-locking technique for large-aperture TEA CO2 lasers,” Appl. Phys. Lett. **30**, 148 (1977).
15. J. E. Murray and W. H. Lowdermilk, “ND:YAG regenerative amplifier,” J. Appl. Phys. **51**, 3548 (1980).
16. Australian Patent PCT/AU2006/ 001852, Dec. 2006.
17. T. J. Kane and R. L. Byer, “Monolithic, unidirectional single-mode Nd:YAG ring laser,” Opt. Lett. **10**, 65 (1985).
18. J. C. Bienfang, C. A. Denman, B. W. Grime, P. D. Hillman, G. T. Moore and J. M. Telle, “20 W of continuous-wave sodium D2 resonance radiation from sum-frequency generation with injection-locked lasers,” Opt. Lett. **28**, 2219 (2003).

#79105 - $15.00 USD Received 18 January 2007; revised 19 February 2007; accepted 22 February 2007

19. D. C. Hanna, C. G. Sawyers and M. A. Yuratich, "Telescopic resonators for large-volume TEM00-mode operation," Opt. Quantum Electron. **13**, 493 (1981).
20. J. J. Degnan, "Theory of the Optimally Coupled Q-Switched Laser," IEEE J. Quantum Electron. **25**, 214 (1989).
21. C. A. Denman, P. D. Hillman, G. T. Moore, J. M. Telle, J. E. Preston, J. D. Drummond and R. Q. Fugate, "Realization of a 50-watt facility-class sodium guidestar pump laser," Proc. SPIE **5707,** 46-49 (2005)

1. Introduction

The use of lasers to create artificial guide stars for adaptive optics is currently revolutionizing ground based astronomy by permitting correction of the optical aberrations due to the atmosphere and allowing near diffraction limited performance of large aperture, ground based telescopes when no natural guide star is available near the science object [1, 2]. Light emitted at 589 nm is used to excite sodium fluorescence in the upper atmosphere, thereby creating an artificial point-like source of light, or guide star, which can be used as a source for adaptive optics in a telescope to correct for aberrations in the intervening atmosphere. For extremely large ground based telescopes (ELTs) in the 30 m to 100 m diameter class [3], a single Na guide star does not provide sufficient sampling of the atmosphere [4] and a more complex approach is required using multiple laser guide stars distributed across the aperture of the telescope to allow tomography of the intervening atmospheric aberrations [2]. This approach has resulted in the need to develop improved laser sources. There is thus a demand for increased power and improved pulse burst formats to maximize utility and efficiency [3]. The particular requirements for our work are summarized in Table 1 [5] and include a total optical power ≥ 50 W and a waveform consisting of pulses of duration less than 3 µs, operating at pulse repetition frequencies (PRF) up to 800 Hz. Furthermore, the emission must be exactly tunable to the D_2 line of Na, and have a bandwidth that can be optimized between 1 GHz and 3 GHz to enable use of all the Doppler broadened Na available and maximize photon return [1]. Finally, engineering requirements of reliability, robustness and efficiency are important for applications of lasers to telescopes situated on remote mountain tops.

Table 1. Laser Performance Requirements

Output power	≥ 10 W per beam, 5 beams
Temporal format	Pulsed, PRF variable 600 Hz -800 Hz Pulse length 1-3 µs
Wavelength	Na D_2 with ability to tune on/off
Bandwidth	1-3 GHz
Beam quality	< 1.2 x diffraction limited

Approaches to the laser include the first generation dye lasers [6], the more reliable sum-frequency generation (SFG) using solid state lasers [7,8] and recently fiber lasers [9,10], combined with various laser waveform techniques ranging from cw to mode-locking [11]. However, to the best of our knowledge no single approach has fully satisfied all the requirements simultaneously. We have proposed a novel approach [12, 13] using injection mode- locking [14,15] that has the potential to satisfy the above requirements. The concept is summarized below and we also describe critical design verification experiments to demonstrate the viability of the concept.

2. Injection mode-locked guide star laser concept.

Our approach uses sum-frequency generation of two mode-locked Nd:YAG lasers to achieve the desired Na wavelength, similar to previous designs [7,8,11]. Our major contribution is the application of injection mode-locking [14, 15] as a robust method for simultaneous control of the absolute wavelength, bandwidth and timing for SFG. An additional feature is the use of a novel, efficient resonator involving stretched Q-switching [16]. Together, these two techniques are used to produce a burst of high peak power micro-pulses optimized for efficient SFG and contained in longer macro-pulses, separately optimized to minimize bleaching of the sodium in the upper atmosphere. While injection mode-locking using a single

#79105 - $15.00 USD Received 18 January 2007; revised 19 February 2007; accepted 22 February 2007

injected pulse has previously been used to create single short pulses in CO_2 [14] and Nd:YAG [15] lasers, to the best of our knowledge it has not previously been used to produce a long macro-pulse consisting of many micro-pulses with simultaneous control of the bandwidth.

The overall concept is shown in Fig. 1. It uses two cw non planar ring oscillator (NPRO) lasers [17], each stabilized accurately to the wavelengths near 1064 nm and 1319 nm required to produce the Na wavelength by SFG [7]. For robust operation and control we propose using an active servo to accomplish this as shown, but in practice this may not be necessary due to the inherent stability of the NPROs [18]. From the output of each of these cw lasers, we slice a pulse of about 1 ns duration to inject into the slave power resonator for injection mode-locking. Accurate control of the width of the injected pulse is used to control the bandwidth of the micro-pulses of the injection mode-locked output. Precise timing of the two injected pulses is required for efficient single-pass SFG. This is ensured by operating both pulse slicers in series from the same high voltage pulser, thus minimizing timing jitter between the 1064 nm and the 1319 nm micro-pulses.

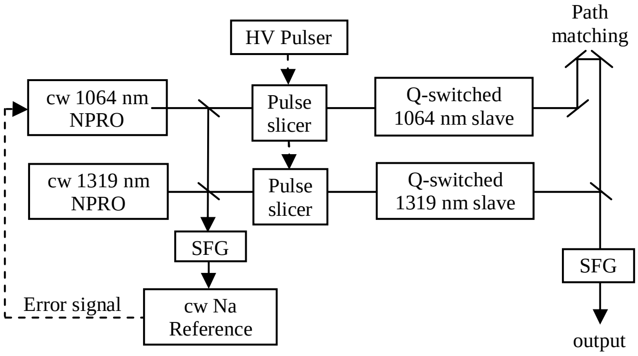

Fig. 1. Overall design concept. Two cw NPRO lasers provide the absolute wavelength control and tuning, and synchronized pulse slicers provide timing and bandwidth control of injection mode-locked slave lasers for subsequent SFG at the Na wavelength.

3. Design verification experiments using a subscale, 1064nm laser.

3.1 Seed pulse production

To investigate bandwidth control by injection mode-locking, we have assembled a versatile pulsed seed source consisting of an NPRO master laser followed by two 50 ohm Pockels cells between linear polarizers. Two independent high voltage avalanche transistor pulsers are used to provide fast rise time (100 ps) electrical pulses to the Pockels cells. This setup allows complete control of the optical pulse width, by using one Pockels cell to turn on the pulse and the other to turn it off, with an adjustable time delay between the two events.

Using this pulse slicer, we have produced optical seed pulses of peak power up to 0.5 W, and pulse duration continuously adjustable between 1 ns and 200 ps, with examples shown in Fig. 2. The near-cw light rejected by the pulse slicer would be used to lock the master lasers to the sodium wavelength by cw SFG, if required. The jitter between the trigger of the high voltage pulse generators and the output of the mode-locked laser (see below) was measured, using a fast sampling oscilloscope, to be < 10 ps rms. This low jitter proves that timing of the output micro-pulses is determined by the input pulse, as required for efficient SFG of two mode-locked lasers, and allows for very precise control of the pulse width in our design verification experiments.

#79105 - $15.00 USD Received 18 January 2007; revised 19 February 2007; accepted 22 February 2007

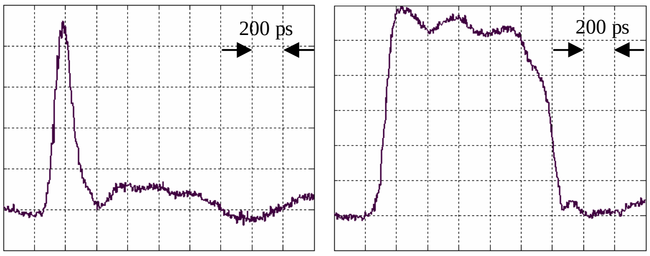

Fig. 2. Optical pulses of variable duration produced by our double Pockels cell switch.

3.2 Slave laser

The slave laser (Fig. 3) was assembled for use in the design verification experiments only. It uses a conduction cooled Nd:YAG zigzag slab, 4.00 mm x 4.32 mm x 36.14 mm, which is side pumped in the zigzag plane by pulsed semiconductor lasers. The laser makes use of a 3.5 m long ring oscillator incorporating a Q-switch, a thin film polarizer (TFP) for injection and extraction and a half wave plate (HWP). Together, these elements allow the efficient production of stretched Q-switched pulses [16]. Telescopes were included to provide resonator stability while creating a large size TEM_{00} mode (ω = 1.2 mm) inside the zigzag slab [19]. This configuration permits efficient extraction of the stored energy, avoids damage to optics from the high peak power micro-pulses and reduces the optical gain per round trip, which lengthens the output macro-pulse width [20].

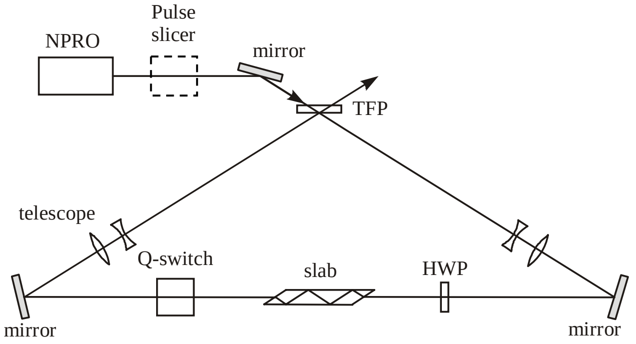

Fig. 3. Slave laser configuration, showing pulse injection into a traveling ring oscillator via a polarizing beam splitter (TFP), and the arrangement of polarizing elements (HWP) and Q-switch required to stretch the macro-pulse formed.

For injection mode-locking, a π-polarized seed pulse is injected into the resonator through the TFP. For the first pass, the seed pulse polarization is converted to σ by the HWP, and with no voltage applied to the Q-switch the seed pulse passes through without a change in polarization. It is thus completely reflected by the TFP and then converted to π polarization by the HWP. Voltage has meanwhile been applied to the Q-switch rotating the polarization back to σ thus trapping the pulse within the ring and enabling development of the giant pulse. Once the pulse has built up sufficiently, the voltage applied to the Q-switch is reduced slightly, allowing a controlled out-coupling fraction of the TFP. By varying this voltage the stretching of the output pulse can be controlled. Thus the Q-switch in our resonator produces no polarization rotation losses during build-up of the pulse and, instead of being opened completely to cavity dump the pulse as in conventional regenerative amplifiers [15], it is used to stretch the output pulse. Due to the broad bandwidth of the injected seed pulse, no servo was required to keep the slave locked to the master oscillator.

#79105 - $15.00 USD Received 18 January 2007; revised 19 February 2007; accepted 22 February 2007

3.3 Design verification results.

Initial experiments were done to investigate injection mode-locking with no pulse stretching. The slave laser produced a near diffraction limited ($M^2 = 1.06$) 1064 nm beam. A typical output of the injection mode-locked slave resonator is shown in Fig. 4. The optimized output was 20 mJ per macro-pulse at 50 Hz PRF, limited by the pump lasers used. This is the energy per macropulse of a laser with average power of 16 W operating at 800 Hz PRF, and our initial result is thus already of significance to conventional laser guide star requirements. Each macro-pulse consists of more than 30 micro-pulses separated by 12 ns, the round trip time of the slave resonator. This could be adjusted in terms of the 16 ns Na fluorescence life time [1,7] to minimize bleaching and thus optimize the photon return from the guide star. The waveform shown was obtained on every pulse without the need for any feedback to the slave oscillator and it was observed that the shape of each micro-pulse from the slave laser closely resembled that of the input seed pulse.

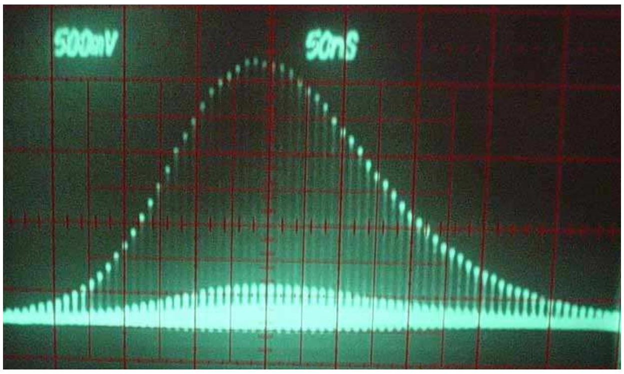

Fig. 4. A single macro-micro pulse output, consisting of a train of injection mode-locked micro-pulses. The time scale is 50 ns per half cm, or 0.9µs across the whole picture.

The input pulse width was measured using a sampling oscilloscope and a fast detector with an overall detection bandwidth of 12 GHz, with typical seed pulse shapes obtained as shown in Fig. 2. The bandwidth of the output of the slave laser was measured by integrating the output of a scanning Fabry-Perot interferometer over many macro-pulses. An example of one of these bandwidth measurements is shown in Fig. 5(a). While the resolution of the Fabry-Perot is 40 MHz, longitudinal laser modes can not be resolved in this figure due to the drift of modes within the envelope of the lasers spectrum, caused by changes in the slave cavity length from thermal expansion. The irregular shape of the spectrum is believed due to the irregular shape of the injected seed pulse (Fig. 2). A plot of the FWHM of a Gaussian fit to each spectrum is shown as a function of the injected seed pulse width in Fig. 5(b). We thus succeeded in controlling the bandwidth of the output from 0.8 GHz to 2.3 GHz. The bandwidth of the final SFG is expected to be approximately twice that of the fundamental wavelengths [7] and the results obtained thus essentially satisfy the system requirements. It is not expected to be difficult to modify the temporal shape of the seed pulse or to increase its duration slightly if a lower bandwidth is desired.

The BBO Q-switch was driven by a specially designed pulser, capable of pulse stretching as discussed. Excellent throttled Q-switching and resulting macro-pulse stretching with no loss in pulse energy was achieved as shown in Fig. 6. The tendency towards a flat top envelope will facilitate subsequent SFG optimization.

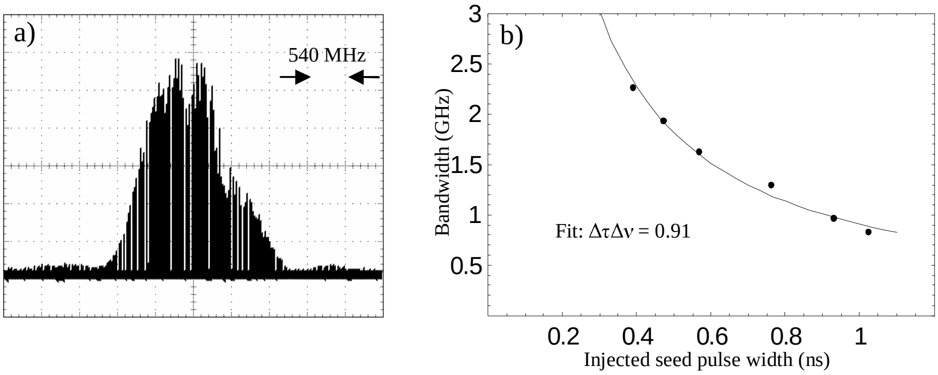

Fig. 5. (a). Spectrum of the slave output corresponding to a seed pulse width of 760 ps. The FWHM bandwidth is 1.3 GHz. (b) Plot of measurements of slave laser bandwidth versus the width of the seed pulse. The curve is a fit to the data with a time-bandwidth product of 0.91 as shown.

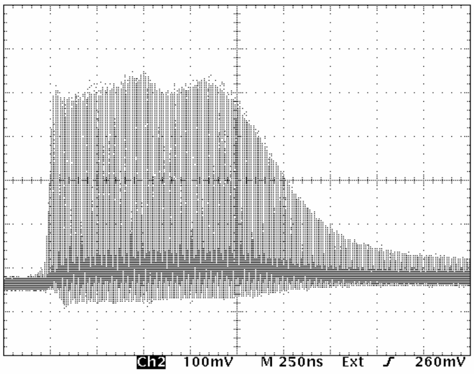

Fig. 6. Example of a stretched macro-pulse, 10 mJ per pulse, 50 Hz. The un-stretched macro-pulse in this case is similar to Fig. 4, but with FWHM width of 300ns.

4. Discussion and conclusion

We have proposed a new concept for sodium guide star lasers that appears to satisfy most critical requirements for planned telescope designs. Our design verification experiments have demonstrated the viability of our approach, including demonstrating a preferred pulse burst waveform, detailed bandwidth control, wavelength control and low timing jitter. Additional work is in progress to demonstrate the concept at 1319 nm and to optimize the concept at the power and wavelengths for the Na guide star. This optimization will include a simplified pulse slicer, optimized laser sources, the possible use of additional laser power amplifiers and optimized SFG. Detailed designs and proof of concept experiments for our approach remain to be done, but some critical design issues have already been demonstrated by others such as the operation of simple extra cavity SFG using mode-locked pump lasers [11] and the realization of 50W class SFG Na guide star lasers [21].

Acknowledgments

This paper is based upon work supported by the National Science Foundation under Cooperative Agreement No. AST0084699. We thank B. Ellerbroeck and J. C. Shelton for useful discussions and R. F. Wuerker, B. Middlemiss and N. Wild for technical contributions.

Rutten, T.P., Wild, N. and Veitch, P.J. (2007) Fast rise time, long pulse width, kilohertz repetition rate Q-switch driver.
Review of Scientific Instruments, v.78 (7), pp. 073108-1-073108-2, 2007

Rutten, T.P., Veitch, P.J. and Munch, J. (2008) Efficient pulse stretching of *Q*-switched lasers
IEEE Journal of Quantum Electronics, v.44 (10), pp. 911-915, October 2008

Munch, J., Rutten, T.P., Simakov, N., Hamilton, M., d'Orgeville, C. and Veitch, P.J.
(2008) A new guide star laser using optimized injection mode-locking.
Proceedings of SPIE, v.7015, pp. 70150K-1 – 70150K-9, June 2008

Appendix B

Zero jitter picosecond delay generator

As was discussed in Section 3.4, a seed pulse source was constructed to generate the low energy seed pulses required for injection mode-locking. Seed pulses were generated by gating the output of a cw NPRO master laser using the dual Pockels cell (PC) switch shown in Figure 3.7. To create the seed pulse, a fast rise time flat-topped high voltage electrical pulse is delivered to the first PC in the pulse slicer to create the leading edge of the seed pulse, then after a short delay, voltage is given to the second PC to create the trailing edge of the seed pulse. The length of the delay between firing PCs sets the width of the seed pulse. The delay needs to be in the range of 300 ps - 3 ns and adjustable to produce a suitably short seed pulse to provide the spectral bandwidths required for the guide star laser (1-3 GHz). Hence there was a need to design and construct a delay generator to delay the arrival time of the trigger pulse to the high voltage Pockels cell driver on the second PC in the pulse slicer, to control the seed pulse width. This delay generator was designed and built by the author and is shown in Figure B.1. It consists of a series of mechanical switches and lengths of coaxial cable to implement the delay. The trigger pulse enters the delay box through the top BNC connector shown in Figure B.1 and exits through the bottom. When all switches are turned "off" the minimum delay is set and the trigger pulse travels through the shorted right hand side of the switches. When a switch is turned on, the trigger pulse is redirected through a short length of coaxial cable on the left hand side of the switch which delays the pulse arrival time. The speed of an electrical signal in coaxial cable is 0.695 c (for RG174), so a cable length of 1 cm represents a delay of 43 ps. By switching various combinations of switches, the delay box shown in Figure B.1, can produce delays of up to 3 ns in 100 ps increments. An important feature of this device is that the delay is generated passively and does not

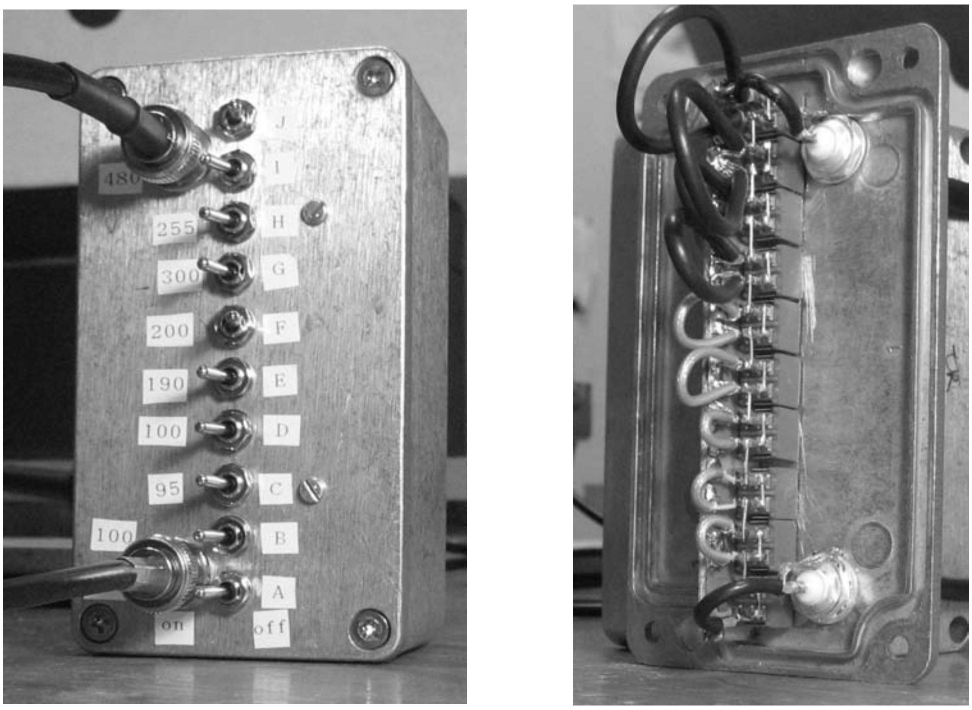

Figure B.1: A photograph of the delay generator used to control the width of the seed pulses required for injection mode-locking. Lengths of coaxial cable are switched into or out of the dignal path to control the length of the time delay.

introduce any timing jitter to the trigger pulse. Electronic devices, that generate a delay using a timing circuit, invariably introduce significant timing jitter that will introduce micro-pulse width jitter in the guide star system resulting in sub-optimum bandwidth matching to the Doppler broadened Sodium absorption line.

Appendix C

High voltage high bandwidth attenuator

To measure the voltage pulses generated by the avalanche transistor circuits (HV pulsers) that were used to drive the fast Pockels cells in the seed pulse source (Section 3.4) a high voltage, high bandwidth attenuator was designed and constructed.

The HV pulsers generate 4 kV pulses with 1 or 3 ns duration and a have rise time of approximately 100 ps. To view these pulses on a sampling oscilloscope, the voltage needs to be reduced to around 1 V (a reduction of 72 dB) to avoid damaging the instrument. The attenuator must also have a high bandwidth of at least 2 GHz to prevent distortion of the pulse shape. Commercial high voltage attenuators are generally low bandwidth devices (tens of MHz) due to the difficulty in maintaining the characteristic impedance of a transmission line over high voltage resistors in a voltage divider (attenuating) network.

A simple high voltage high bandwidth attenuator was constructed in house out of a series of lengths of coaxial cable and T-junctions as shown in Figure C.1. This device uses the cable reflections at the T-junctions to attenuate the pulse, rather than a resistive voltage divider, thereby providing improved bandwidth. At each T-junction, the cable impedance changes from 50 ohms to 25 ohms (two 50 ohm lines in parallel) and hence there is a 30 % reflection loss at each junction. The attenuator consisted of a total of 5 junctions resulting in a total of 18 dB attenuation.

To test the attenuator, a 10 V pulse from a commercial pulse generator was observed before and after attenuation. A comparison is shown in Figure C.2, showing that the attenuation is approximately 18 dB.

This method of attenuation results in only a short time interval with which to view the pulse before the signal is distorted by the arrival of back-reflections from alternate T-junctions. After a time equal to twice the delay time of the shortest length of coaxial

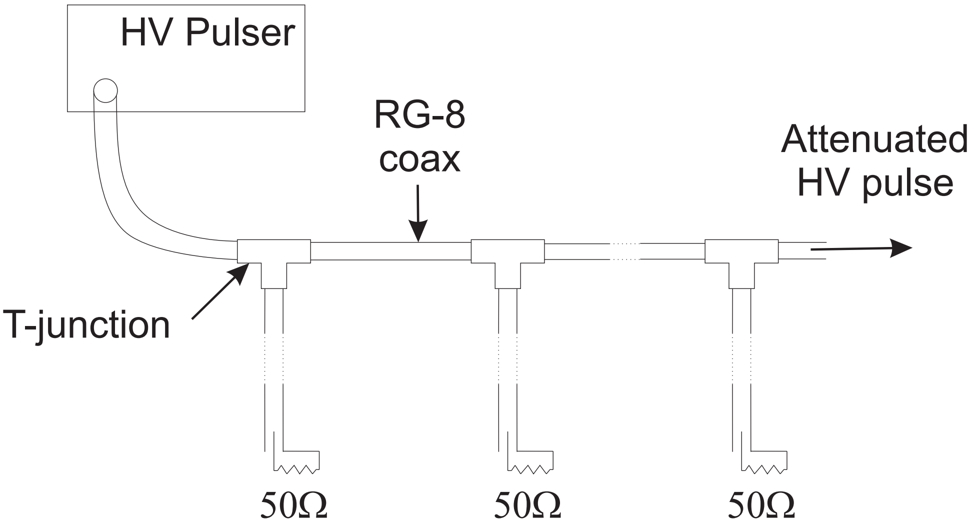

Figure C.1: The high voltage attenuator makes use of the 30 % reflection loss occurring at each T-junction to provide attenuation while maintaining signal bandwidth.

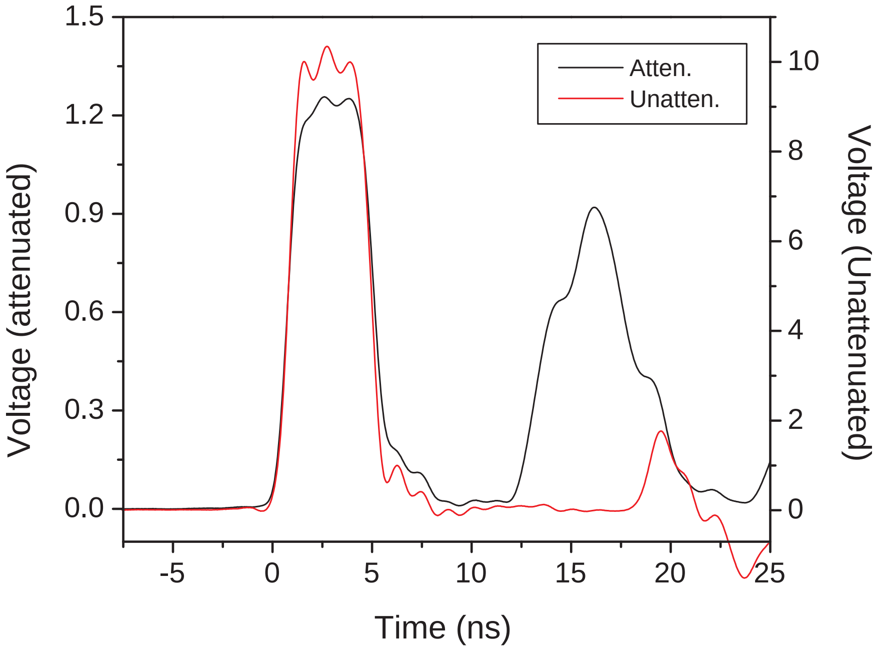

Figure C.2: An overlay plot showing a voltage pulse before and after passing through the attenuator. The pulse amplitude is reduced from 10 V to 1.2 V (approx 18 dB). At time= 12 ns, back-reflections from the T-junctions in the attenuator are detected in the attenuated signal. Any signal recorded past this time is not representative of the true pulse shape.

cable (12 ns in our case), the signal back-reflected from neighbouring T-junctions will arrive at the output of the attenuator. By making the lengths of coaxial cable between T-junctions longer, the viewing period will be increased.

Following the high voltage high bandwidth attenuator of Figure C.1 a series of 3 commercial, low voltage 20 dB 20 GHz attenuators were used to further reduce the voltage to below 1 V. The bandwidth of the attenuator is limited by the inherent frequency response of the coaxial cable. The Rg-8 cable used has an attenuation of 0.135dB/m for 400 MHz frequencies, .262 dB/m at 1 GHz, .525 dB/m at 3 GHz and .886 dB/m at 5 GHz frequencies. The total length of cable used between the HV pulser and oscilloscope was 7.7 m resulting in a bandwidth limit of approximately 2 GHz for the attenuator constructed for this work. Using higher bandwidth cable will improve the frequency response of the attenuator. The output of the HV pulsers after passing through the high voltage attenuator can be seen in Figure 3.8.

Appendix D

Pulse stretching model parameters

In Section 4.3 a theoretical model is described that predicts the Q-switched pulse shapes from an injection mode-locked laser. Inputs to the model include the cross-sectional area, A, of the laser mode inside the slab and the round trip loss, l, of the resonator. This section presents an estimation of the real values of mode size and loss expected for the ring resonator of Figure 4.1. The values used in the model were $A = 5.5$ mm^2 and $l = 5$ %.

The size of the laser mode just outside the slab is ω =1.2 mm (see Figure D.1). Inside the slab, the size of the mode is larger, 1.2 mm (horizontal) and 2.42 mm (vertical) due to magnification from the Brewster-angled window, as shown in Figure D.1. This gives a mode area of 9.1 mm^2 inside the slab if the beam size is defined by the $1/e^2$ radius (ω). If the beam size is defined by the FWHM, the beam area is 3.6 mm^2.

The theoretical model of Section 4.3 assumes that the beam profile has a rectangular "top-hat" intensity distribution. The laser used for these experiments is near diffraction limited and hence has a Gaussian intensity profile. Hence the beam size used in the model should be an approximation to the real beam size. A value of A = 5.5 mm^2 was used

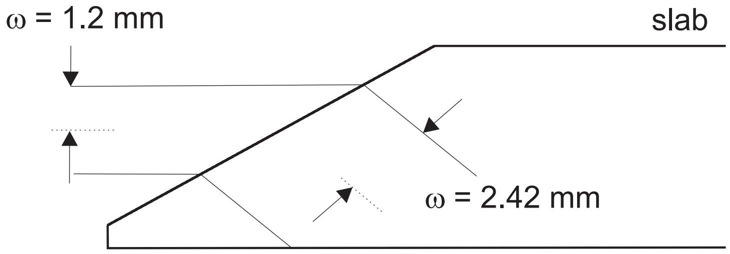

Figure D.1: This sketch shows the size of the laser outside and inside the laser slab. In the vertical direction the mode size expands by a fact of approximately 2 due to the angle of the slab window. In the horizontal direction (into the page) the mode size is 1.2 mm both outside and inside the slab.

in the model which is between the $1/e^2$ and FWHM values. This gives good agreement between predicted and measured data, as shown in Figure 4.3.

The round trip resonator loss, l, is made up of the sum of the losses from scatter and absorption at each resonator optic (Q-switch, slab, TFP, mirrors and lens) and also diffraction losses caused by the surface error of each of these optics. The loss from surface errors will manifest when the laser is running in a TEM_{00} resonator and surface errors will transfer energy to higher order modes that will suffer losses from clipping on intra-cavity apertures (the slab window).

The scatter and absorption losses were measured by recording the transmission or reflection of a cw NPRO probe beam incident upon an optic in question. Using this technique, the loss of the Q-switch was measured to be 0.6 % ± 0.06, the slab was 1.6 % ± 0.2, the TFP was 0.6 % ± 0.06, the mirrors were 0.5 % ± 0.05 and the lens was 0.6 % ± 0.06, giving a total loss for scatter and absorption of 4.4 % ± 0.6. The measurement uncertainty is from the accuracy of the laser power meter used.

Round trip losses caused by surface errors and resonator misalignment were not measured.

Appendix E

Laser slab and waveguide schematic diagrams

This section contains the schematic diagrams and specifications that were sent to the manufacturer for the procurement of the Nd:YAG slab and waveguides. The Nd:YAG material was obtained from Scientific Materials Corp. [120] and the cut and polishing of the slab and waveguides was done by BAE Systems [121]. All specifications and tolerances were calculated and then subsequently drawn up by the author.

The University of Adelaide, Department of Physics

Requirements of Nd:YAG blank, Page 1 of 1.

MATERIAL
·Yttrium Aluminium Garnet doped with Neodymium to one atomic percent (1.0% Nd:YAG).
·SP grade - high purity suitable for laser slabs.
·Material must be cut from the boule with crystallographic direction shown in diagram opposite.

SPECIFICATIONS
·Un-finished blank.
·Minimum dimensions shown in diagram below.

Nd:YAG Boule (Top View)

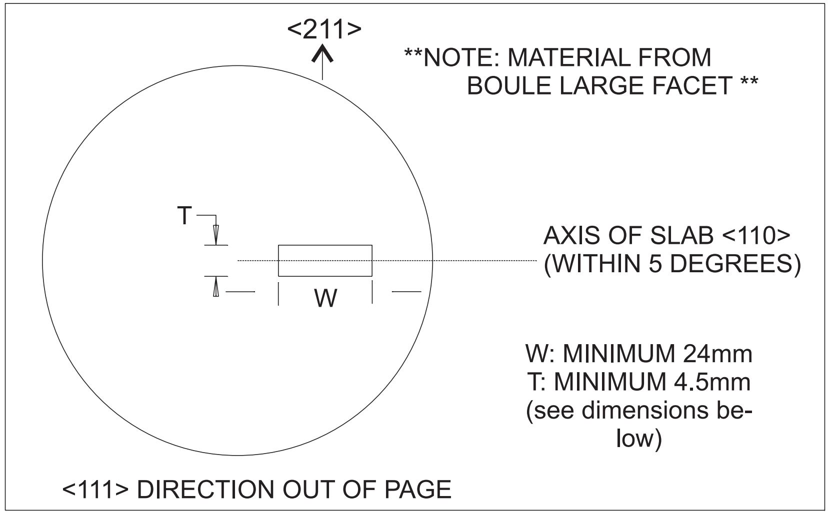

Minimum Dimensions:

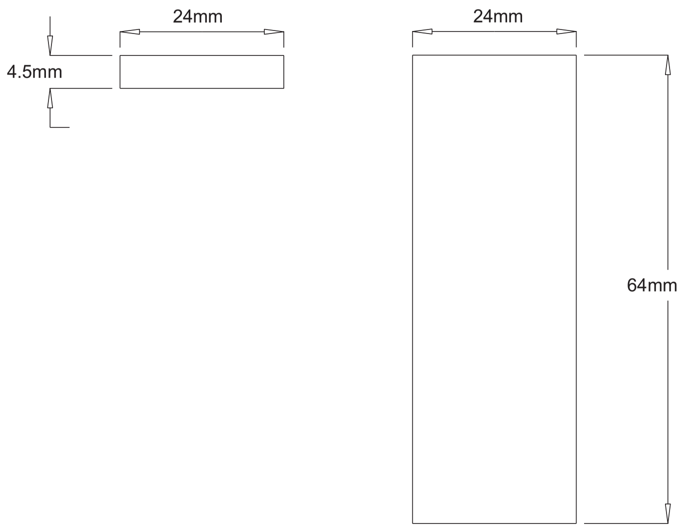

The University of Adelaide, Department of Physics
Laser Slab, page 2 of 2

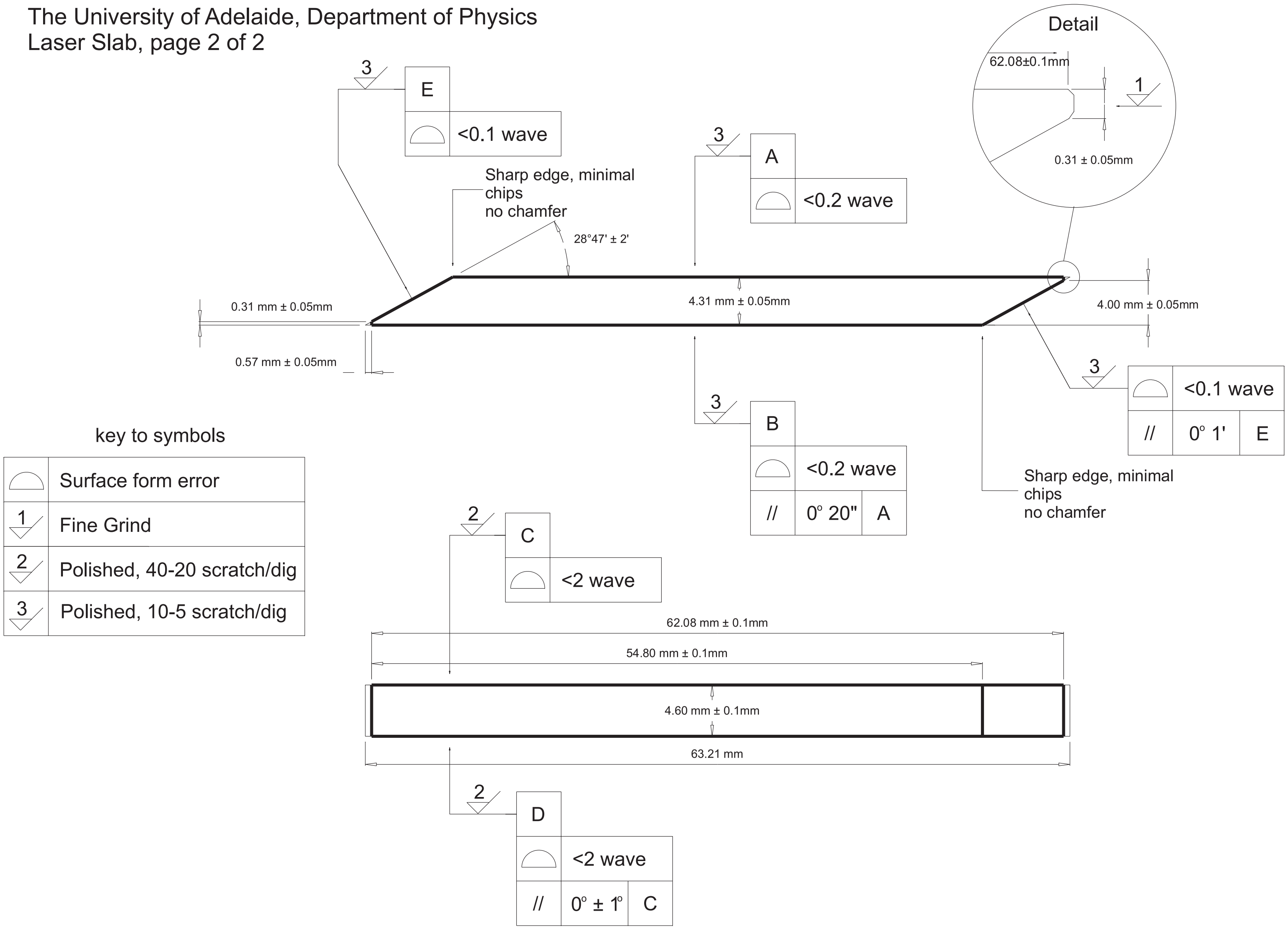

The University of Adelaide, Department of Physics

Waveguide to deliver pump light from laser diode array
to Nd:YAG slab. Page 1of 1.

MATERIAL:
·BK 7

QUANTITY:
·Five

MANUFACTURE REQUIREMENTS:
·All polished surfaces to have 2-wave flatness
·Edges bordering side C chamfered, 45 degrees
·All other edges sharp with minimal chipping, especially
  edges bordering side D
·Side C and D broad angle AR coat for 808nm - coating
  determined previously

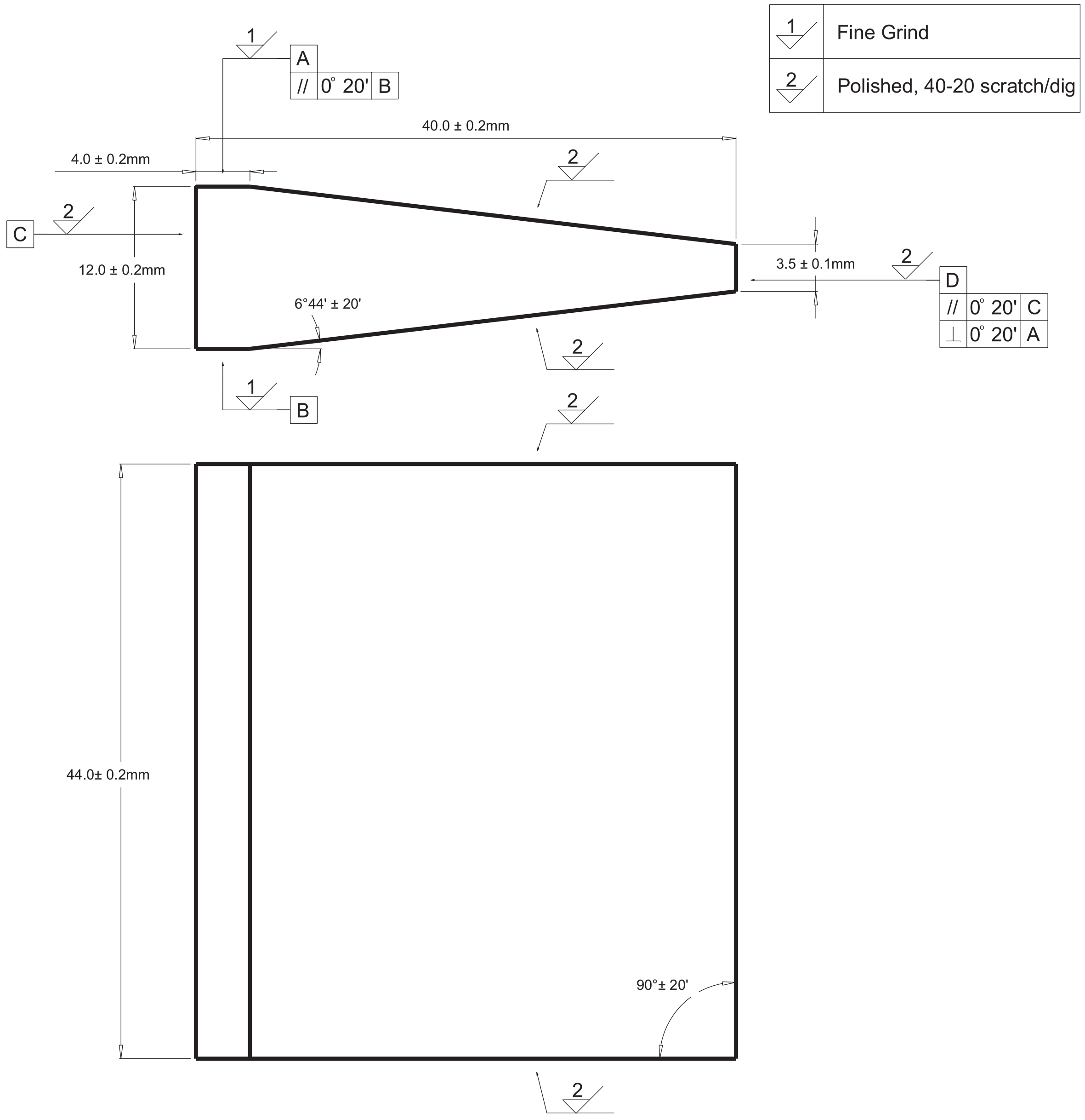

Bibliography

[1] P. A. Knutsson and M. Owner-Petersen, “Emulation of dual-conjugate adaptive optics on an 8-m class telescope,” *Opt. Express*, vol. 11, no. 18, pp. 2231–2237, 2003.

[2] D. L. Fried, “Limiting Resolution Looking Down Through the Atmosphere,” *J. Opt. Soc. Am.*, vol. 56, pp. 1380–1384, 1966.

[3] H. M. Dyck and R. R. Howell, “Seeing measurements at Mauna Kea from infrared speckle interferometry,” *Publ. Astron. Soc. Pac.*, vol. 95, pp. 786–791, 1983.

[4] H. W. Babcock, “The possibility of compensating astronomical seeing,” *Publ. Astron. Soc. Pac.*, vol. 65, p. 229, 1953.

[5] D. P. Greenwood, “Bandwidth specification for adaptive optics systems,” *J. Opt. Soc. Am.*, vol. 67, pp. 390–393, 1977.

[6] L. A. Thompson and C. S. Gardner, “Experiments on laser guide stars at Mauna Kea Observatory for adaptive imaging in astronomy,” *Nature*, vol. 328, pp. 229–231, 1987.

[7] R. Q. Fugate, D. L. Fried, G. A. Ameer, B. R. Boeke, S. L. Browne, P. H. Roberts, R. E. Ruane, G. A. Tyler, and L. M. Wopat, “Measurement of atmospheric wavefront distortion using scattered light from a laser guide-star,” *Nature*, vol. 353, pp. 144–146, 1991.

[8] C. A. Primmerman, D. V. Murphy, D. A. Page, B. G. Zollars, and H. T. Barclay, “Compensation of atmospheric optical distortion using a synthetic beacon,” *Nature*, vol. 353, pp. 141–143, 1991.

[9] R. V. Shack and B. C. Platt, “Production and use of a lenticular Hartmann screen,” *J. Opt. Soc. Am.*, vol. 61, p. 656, 1971.

[10] R. K. Tyson, *Introduction to adaptive optics.* Bellingham, Washington 98227-0010: SPIE press, 1st ed., 2000.

[11] J. M. Beckers, "Adaptive optics for astronomy - Principles, performance, and applications," *Annu. Rev. Astron. Astrophys.*, vol. 31, pp. 13–62, 1993.

[12] R. Foy and A. Labeyrie, "Feasibility of adaptive telescope with laser probe," *Astron. Astrophys*, vol. 152, no. 2, pp. L29–L31, 1985.

[13] R. A. Humphreys, C. A. Primmerman, L. C. Bradley, and J. Herrmann, "Atmospheric-turbulence measurements using a synthetic beacon in the mesospheric sodium layer," *Opt. Lett.*, vol. 16, pp. 1367–1369, 1991.

[14] W. Happer, G. J. MacDonald, C. E. Max, and F. J. Dyson, "Atmospheric-turbulence compensation by resonant optical backscattering from the sodium layer in the upper atmosphere," *J. Opt. Soc. Am. A*, vol. 11, p. 263, 1994.

[15] H. W. Friedman, G. V. Erbert, T. C. Kuklo, T. Salmon, D. A. Smauley, G. R. Thompson, J. G. Malik, J. N. Wong, V. K. Kanz, and K. P. Neeb, "Sodium beacon laser system for the Lick Observatory," in *Proc. SPIE*, vol. 2534, p. 150, 1995.

[16] C. E. Max, S. S. Olivier, H. W. Friedman, J. An, K. Avicola, B. V. Beeman, H. D. Bissinger, J. M. Brase, G. V. Erbert, D. T. Gavel, K. Kanz, M. C. Liu, B. Macintosh, K. P. Neeb, J. Patience, and K. E. Waltjen, "Image Improvement from a Sodium-Layer Laser Guide Star Adaptive Optics System," *Science*, vol. 277, no. 5332, pp. 1649–1652, 1997.

[17] T. H. Jeys, A. A. Brailove, and A.Mooradian, "Sum frequency generation of sodium resonance radiation," *Appl. Opt.*, vol. 28, no. 13, pp. 2588–2591, 1989.

[18] C. A. Denman, P. D. Hillman, G. T. Moore, J. M. Telle, J. E. Preston, J. D. Drummond, and R. Q. Fugate, "Realization of a 50-watt facility-class sodium guidestar pump laser," in *Proc. SPIE*, vol. 5707, pp. 46–49, 2005.

[19] A. Tracy, A. Hankla, C. Lopez, D. Sadighi, N. Rogers, K. Groff, I. McKinnie, and C. d'Orgeville, "High-power solid-state sodium beacon laser guidestar for the Gemini North Observatory," in *Proc. SPIE*, vol. 5490, pp. 998–1009, 2004.

[20] E. J. Kibblewhite and F. Shi, "Design and field test of an 8 watt sum-frequency laser for adaptive optics," in *Proc. SPIE*, vol. 3353, pp. 300–309, 1998.

[21] M. Duering, V. Kolev, and B. Luther-Davies, "Generation of tuneable 589nm radiation as a Na guide star source using an optical parametric amplifier," *Opt. Express*, vol. 17, no. 2, pp. 437–446, 2009.

[22] D. Georgiev, V. P. Gapontsev, A. G. Dronov, M. Y. Vyatkin, A. B. Rulkov, S. V. Popov, and J. R. Taylor, "Watts-level frequency doubling of a narrow line linearly polarized Raman fiber laser to 589nm," *Opt. Express*, vol. 13, pp. 6772–6776, 2005.

[23] D. M. Pennington, R. Beach, J. Dawson, A. Drobshoff, Z. Liao, S. Payne, D. Bonaccini, W. Hackenberg, and L. Taylor, "Compact fiber laser approach to generating 589 nm laser guide stars," in *Proceedings of Conference on Lasers and Electro-Optics Europe*, p. 730, 2003.

[24] N. Hubin, B. L. Ellerbroek, R. Arsenault, R. M. Clare, R. Dekany, L. Gilles, M. Kasper, G. Herriot, M. L. Louarn, E. Marchetti, S. Oberti, J. Stoesz, J. P. Veran, and C. Verinaud, "Adaptive optics for Extremely Large Telescopes," in *in Proceedings IAU Symposium No. 232*, pp. 60–85, 2006.

[25] F. Rigaut, "Ground-Conjugate Wide Field Adaptive Optics for the ELTs," *in Beyond Conventional Adaptive Optics*, 2001. Venice.

[26] Requirements from Gemini RFP no. N231397, Dec. 2003.

[27] J. M. Beckers, "Overcoming perspective elongation effects in laser-guide-star-aided adaptive optics," *Appl. Opt.*, vol. 31, no. 31, pp. 6592–6594, 1992.

[28] J. Cabannes, J. Dufay, and J. Gauzit, "Sodium in the Upper Atmosphere," *Astrophys. J.*, vol. 88, pp. 164–172, 1938.

[29] P. W. Milonni, R. Q. Fugate, and J. M. Telle, "Analysis of measured photon returns from sodium beacons," *J. Opt. Soc. Am. A*, vol. 15, no. 1, pp. 217–233, 1998.

[30] T. H. Jeys, R. M. Heinrichs, K. F. Wall, J. Korn, T. C. Hotaling, and E. Kibblewhite, "Observation of optical pumping of mesospheric sodium," *Opt. Lett.*, vol. 17, pp. 1143–1145, 1992.

[31] Response to Gemini RFP no. N231397, Jan 2004.

[32] T. P. Rutten, P. J. Veitch, C. d'Orgeville, and J. Munch, "Injection mode-locked guide star laser concept and design verification experiments," *Opt. Express*, vol. 15, no. 5, pp. 2369–2374, 2007.

[33] J. Munch, T. P. Rutten, N. Simakov, M. Hamilton, C. d'Orgeville, and P. J. Veitch, "A new guide star laser using optimized injection mode-locking," in *Proc. SPIE*, vol. 7015, p. 70150K, 2008.

[34] C. E. Max, K. Avicola, J. M. Brase, H. W. Friedman, H. D. Bissinger, J. Duff, D. T. Gavel, J. A. Horton, R. Kiefer, J. R. Morris, S. S. Olivier, R. W. Presta, D. A. Rapp, J. T. Salmon, and K. E. Waltjen, "Design, layout, and early results of a feasibility experiment for sodium-layer laser-guide-star adaptive optics," *J. Opt. Soc. Am. A.*, vol. 11, no. 2, pp. 813–824, 1994.

[35] D. B. Calia, W. Hackenberg, C. Araujo, I. Guidolin, and J. L. Alvarez, "Laser guide star related activities at ESO," in *Proc. SPIE*, vol. 5490, pp. 974–980, 2004.

[36] Y. Feng, S. Huang, A. Shirakawa, and K. Ueda, "589 nm light source based on Raman fiber laser," *Jap. J. Appl. Phys.-2*, vol. 43, pp. L722–L724, 2004.

[37] M. Frede, B. Schulz, R. Wilhelm, P. Kwee, F. Seifert, B. Willke, and D. Kracht, "Fundamental mode, single-frequency laser amplifier for gravitational wave detectors," *Opt. Express*, vol. 15, pp. 459–465, 2007.

[38] H. J. E. A. Haase and R. Menzel, "100-watt average output power 1.2 diffraction limited beam frompulsed neodymium single-rod amplifier with sbs phase conjugation," *IEEE J. Quantum Electron.*, vol. 31, pp. 1265–1269, 1995.

[39] H. Moosmüller and J. D. Vance, "Sum-frequency generation of continuous-wave sodium D2 resonance radiation," *Opt. Lett.*, vol. 22, pp. 1135–1137, 1997.

[40] A. J. Alcock, P. B. Corkum, and D. J. James, "A simple mode-locking technique for large-aperture TEA CO2 lasers," *Appl. Phys. Lett.*, vol. 30, no. 3, pp. 148–150, 1977.

[41] J. C. Bienfang, C. A. Denman, B. W. Grime, P. D. Hillman, G. T. Moore, and J. M. Telle, "20 W of continuous-wave sodium D2 resonance radiation from sum-frequency generation with injection-locked lasers," *Opt. Lett.*, vol. 28, no. 22, pp. 2219–2221, 2003.

[42] J. H. Eberly and P. W. Milonni, *Lasers.* Springer, Berlin: John Wiley and Sons Inc, 1st ed., 1988.

[43] J. E. Murray and W. H. Lowdermilk, "ND:YAG regenerative amplifier," *J. Appl. Phys.*, vol. 51, no. 7, pp. 3548–3554, 1980.

[44] Australian Patent no. PCT/AU2006/001852, Dec. 2006.

[45] Specification from OFR VHP series isolators at 1064 nm, website: www.ofr.com.

[46] R. Lovberg, E. Wooding, and M. Yeoman, “Pulse stretching and shape control by compound feedback in a Q-switched ruby laser,” *IEEE J. Quantum Electron.*, vol. QE-11, no. 1, pp. 17–21, 1975.

[47] G. Harigel, C. Baltay, M. Bregman, M. Hibbs, A. Schaffer, H. Bjelkhagen, J. Hawkins, W. Williams, P. Nailor, R. Michaels, and H. Akbari, “Pulse stretching in a Q-switched ruby laser for bubble chamber holography,” *Appl. Opt.*, vol. 25, no. 22, pp. 4102–4110, 1986.

[48] P. Heinz, W. Kriegleder, and A. Laubereau, “Feedback control of an actively-passively mode-locked Nd:Glass laser,” *Appl. Phys. A*, vol. 43, pp. 209–212, 1987.

[49] J. J. Degnan, “Theory of the optimally coupled Q-switched laser,” *IEEE J. Quantum Electron.*, vol. 25, no. 2, pp. 214–220, 1989.

[50] T. P. Rutten, P. Veitch, and J. Munch, “Efficient pulse stretching of Q-switched lasers,” *IEEE J. Quantum Electron.*, vol. 44, no. 10, pp. 911–915, 2008.

[51] R. W. Boyd, *Nonlinear Optics.* Academic Press, 2nd ed., 2003.

[52] J. A. Armstrong, N. Bloembergen, J. Ducuing, and P. S. Pershan, “Interactions between Light Waves in a Nonlinear Dielectric,” *Phys. Rev.*, vol. 127, no. 6, pp. 1918–1939, 1962.

[53] C. L. Tang and L. K. Cheng, *Fundamentals of Optical Parametric Processes and Oscillators.* Newark, NJ, United States: Harwood academic publishers, 1st ed., 1996.

[54] D. A. Roberts, “Simplified characterization of uniaxial and biaxial nonlinearoptical crystals: a plea for standardization of nomenclature andconventions,” *IEEE J. Quantum Electron.*, vol. 28, no. 10, pp. 2057–2074, 1992.

[55] A. Smith, ”SNLO software package”, retrieved May, 2008, http://www.as-photonics.com/?q=SNLO.

[56] A. Liu, M. A. Norsen, and R. D. Mead, “60-W green output by frequency doubling of a polarized Yb-doped fiber laser,” *Opt. Lett.*, vol. 30, pp. 67–69, 2005.

[57] D. Eimerl, L. Davis, S. Velsko, E. K. Graham, and A. Zalkin, "Optical, mechanical, and thermal properties of barium borate," *J. Appl. Phys.*, vol. 62, pp. 1968–1983, 1987.

[58] A. V. Smith, W. J. Alford, T. D. Raymond, and M. S. Bowers, "Comparison of a numerical model with measured performance of a seeded, nanosecond KTP optical parametric oscillator," *J. Opt. Soc. Am. B*, vol. 12, pp. 2253–2267, 1995.

[59] A. V. Smith, "How to select nonlinear crystals and model their performance using SNLO Software," in *Proc. SPIE*, vol. 3928, pp. 62–69, 2000.

[60] CVI catalogue, 2005.

[61] W. Koechner, *Solid-State Laser Engineering.* New York: Springer-Verlag, 5th ed., 1999.

[62] E. Armandillo, C. Norrie, A. Cosentino, P. Laporta, P. Wazen, and P. Maine, "Diode-pumped high-efficiency high-brightness Q-switched ND:YAG slab laser," *Opt. Lett.*, vol. 22, no. 15, pp. 1168–1170, 1997.

[63] J. Richards, "Birefringence compensation in polarization coupled lasers," *Appl. Opt.*, vol. 26, no. 13, pp. 2514–2517, 1987.

[64] P. R. Stysley, D. Poulios, D. B. Coyle, and R. B. Kay, "Highly efficient dual head 100 mJ TEM00 Nd:YAG Oscillator," *Opt. Laser Technol.*, vol. 40, pp. 435–440, 2008.

[65] T. Y. Fan, "Heat generation in Nd:YAG and Yb:YAG," *IEEE J. Quantum Electron.*, vol. 29, no. 6, pp. 1457–1459, 1993.

[66] G. D. Goodno, S. Palese, J. Harkenrider, and H. Injeyan, "Yb:YAG power oscillator with high brightness and linear polarization," *Opt. Lett.*, vol. 26, no. 21, pp. 1672–1674, 2001.

[67] L. McDonagh, R. Wallenstein, R. Knappe, and A. Nebel, "High-efficiency 60 W TEM_{00} Nd:YVO4 oscillator pumped at 888 nm," *Opt. Lett.*, vol. 31, pp. 3297–3299, 2006.

[68] S. Saraf, K. Urbanek, R. L. Byer, and P. J. King, "Quantum noise measurements in a continuous-wave laser-diode-pumped Nd:YAG saturated amplifier," *Opt. Lett.*, vol. 30, no. 10, pp. 1195–1197, 2005.

[69] R. J. S. Pierre, D. W. Mordaunt, H. Injeyan, J. G. Berg, R. C. Hilyard, M. E. Weber, M. G. Wickham, G. M. Harpole, and R. Senn, "Diode array pumped kilowatt laser," *IEEE J. Sel. Top. Quantum Electron.*, vol. 3, no. 1, pp. 53–58, 1997.

[70] S. Amano and T. Mochizuki, "High average and high peak brightness slab laser," *IEEE J. Quantum Electron.*, vol. 37, no. 2, pp. 296–303, 2001.

[71] M. Ostermeyer, P. Kappe, R. Menzel, and V. Wulfmeyer, "Diode-pumped Nd:YAG master oscillator power amplifier with high pulse energy, excellent beam quality, and frequency-stabilized master oscillator as a basis for a next-generation lidar system," *Appl. Opt.*, vol. 44, no. 4, pp. 582–590, 2005.

[72] C. S. Gardner, "Sodium resonance fluorescence lidar applications in atmospheric science and astronomy," *Proc. IEEE*, vol. 77, no. 3, pp. 408–418, 1989.

[73] Laser head provided by TRW Space and Technology Group, 1 Space Park, Redondo Beach, California, 90278.

[74] T. S. Rutherford, W. M. Tulloch, S. Sinha, and R. L. Byer, "Yb:YAG and Nd:YAG edge-pumped slab lasers," *Opt. Lett.*, vol. 26, no. 13, pp. 986–988, 2001.

[75] T. J. Kane, J. M. Eggleston, and R. L. Byer, "The slab geometry laser−part II: Thermal effects in a finite slab," *IEEE J. Quantum Electron.*, vol. QE-21, no. 8, pp. 1195–1209, 1985.

[76] M. Frede, R. Wilheim, M. Brendel, C. Fallnich, F. Seifert, B. Willke, and K. Danzmann, "High power fundamental mode Nd:YAG laser with efficient birefringence compensation," *Opt. Express*, vol. 12, pp. 3581–3589, 2004.

[77] J. Eggleston, T.Kane, K. Kuhn, J. Unternahrer, and R. Byer, "The slab geometry laser−part I: Theory," *IEEE J. Quantum Electron.*, vol. 20, no. 3, pp. 289–301, 1984.

[78] D. C. Hanna, C. G. Sawyers, and M. A. Yuratich, "Telescopic resonators for large-volume TEM_{00}-mode operation," *Opt. Quantum Electron.*, vol. 13, pp. 493–507, 1981.

[79] D. C. Hanna, C. G. Sawyers, and M. A. Yuratich, "Large-volume TEM_{00} mode operation of Nd:YAG lasers," *Opt. Commun.*, vol. 37, no. 5, pp. 359–362, 1981.

[80] A. I. Bishop and P. F. Barker, "Subnanosecond Pockels cell switching using avalanche transistors," *Rev. Sci. Instrum*, vol. 77, p. 044701, 2006.

[81] Fastpulse Technology Inc. model 1112, www.fastpulse.com.

[82] Avalanche transistor pulsers custom made by Pulstek, www.pulsetek.com.

[83] ACME Engineering Co. Pty. Ltd. Coaxial cable catalogue.

[84] A. K. Dharmadhikari, J. A. Dharmadhikari, K. P. Adhi, N. Y. Mehendale, and R. C. Aiyer, "Low cost fast switch using a stack of bipolar transistors as a pockel cell driver," *Rev. Sci. Instrum.*, vol. 67, no. 12, pp. 4399–4400, 1996.

[85] S. A. Riley, S. May, and M. P. Augustine, "High-voltage pulse switching hardware for electro-optic studies of conducting aqueous solutions," *Rev. Sci. Instrum.*, vol. 73, no. 8, pp. 3080–3084, 2002.

[86] R. E. Continetti, D. R. Cyr, and D. M. Neumark, "Fast 8 kv metal-oxide semiconductor field-effect transistor switch," *Rev. Sci. Instrum.*, vol. 63, no. 2, pp. 1840–1841, 1992.

[87] T. P. Rutten, N. Wild, and P. J. Veitch, "Fast rise time, long pulse width, kilohertz repetition rate q-switch driver," *Rev. Sci. Instrum.*, vol. 78, p. 073108, 2007.

[88] H. Kogelnik and T. Li, "Laser beams and resonators," *App. Opt.*, vol. 5, no. 10, pp. 1550–1567, 1966.

[89] K. Avicola, J. M. Brase, J. R. Morris, H. D. Bissinger, J. M. Duff, H. W. Friedman, D. T. Gavel, C. E. Max, S. S. Olivier, R. W. Presta, D. A. Rapp, J. T. Salmon, and K. E. Waltjen, "Sodium-layer laser-guide-star experimental results," *J. Opt. Soc. Am. A.*, vol. 11, no. 2, pp. 825–831, 1994.

[90] W. R. Callen, R. H. Pantell, and J. Warszawski, "Pulse stretching of Q-switched lasers," *Opto-Elelectron.*, vol. 1, pp. 123–127, 1969.

[91] S. Seidel and G. Phillipps, "Pulse lengthening by intracavity stimulated Brillouin scattering in a Q-switched, phase-conjugated Nd:YAG laser oscillator," *Appl. Opt.*, vol. 32, no. 36, pp. 7408–7416, 1993.

[92] D. Kracht and R. Brinkmann, "Green Q-switched microsecond laser pulses by overcoupled intracavity second harmonic generation," *Opt. Commun.*, vol. 231, pp. 319–324, 2004.

[93] W. E. Schmid, "Pulse Stretching in a Q-switched Nd:YAG Laser," *IEEE J. Quantum Electron.*, vol. QE-16, no. 7, pp. 790–794, 1980.

[94] W. H. Lowdermilk and J. E. Murray, "The multipass amplifier: Theory and numerical analysis," *J. Appl. Phys.*, vol. 51, pp. 2436–2444, 1980.

[95] A. Giesen, H. Hügel, A. Voss, K. Wittig, U. Branch, and H. Opower, "Scalable concept for diode-pumped high-power solid-state lasers," *Appl. Phys. B*, vol. 58, p. 363, 1994.

[96] J. J. Zayhowski and A. Mooradian, "Single-frequency microchip Nd lasers," *Opt. Lett.*, vol. 14, no. 1, pp. 24–26, 1989.

[97] G. D. Goodno, Z. Guo, R. J. D. Miller, I. J. Miller, J. W. Montgomery, S. R. Adhav, and R. S. Adhav, "Investigation of $\beta - BaB_2O_4$ as a Q-switch for high power applications," *Appl. Phys. Lett.*, vol. 66, no. 13, pp. 1575–1577, 1995.

[98] K. Du, N. Wu, J. Xu, J. Giesekus, P. Loosen, and R. Poprawe, "Partially end-pumped Nd:YAG slab laser with a hybrid resonator," *Opt. Lett.*, vol. 23, pp. 370–372, 1998.

[99] S. C. Tidwell, J. F. Seamans, and M. S. Bowers, "Highly efficient 60-W TEM00 cw diode-end-pumped Nd:YAG laser," *Opt. Lett.*, vol. 18, pp. 116–118, 1993.

[100] N. Uehara, K. Nakahara, and K. Ueda, "Continuous-wave TEM00-mode 26.5-W-output virtual-point-source diode-array-pumped Nd:YAG laser," *Opt. Lett.*, vol. 20, no. 16, pp. 1707–1709, 1995.

[101] R. A. Fields, T. S. Rose, M. E. Innocenzi, H. T. Jura, and C. L. Fincher, *Diode laser end-pumped neodymium lasers: The road to higher powers*. OSA, 301-308, 1st ed., 1989.

[102] D. Mudge, P. J. Veitch, J. Munch, D. Ottaway, and M. W. Hamilton, "High-Power Diode-Laser-Pumped CW Solid-State Lasers Using Stable-Unstable Resonators," *IEEE J. Sel. Top. Quantum Electron.*, vol. 3, no. 1, pp. 19–25, 1997.

[103] Private correspondence with Cutting Edge Optronics, 20 Point West Boulevard St. Charles, MO 63301. Website: http://www.st.northropgrumman.com/ceolaser.

[104] M. Ostermeyer, D. Mudge, P. J. Veitch, and J. Munch, "Thermally induced birefringence in Nd:YAG slab lasers," *Appl. Opt.*, vol. 45, no. 21, pp. 5368–5376, 2006.

[105] H. Statz and G. A. de Mars, *Quantum electronics*. New York: Columbia Univ. Press, 1960.

[106] A. E. Siegman, *Lasers.* University Science Books, 1986.

[107] N. P. Barnes, M. E. Storm, P. L. Cross, and M. W. S. Jr, “Efficiency of Nd laser materials with laser diode pumping,” *IEEE J. Quantum Electron.*, vol. 26, no. 3, pp. 558–569, 1990.

[108] T. S. Rutherford, W. M. Tulloch, E. K. Gustafson, and R. L. Byer, “Edge-pumped quasi-three-level slab lasers: design and power scaling,” *IEEE J. Quantum Electron.*, vol. 36, no. 2, pp. 205–219, 2000.

[109] D. B. Coyle, R. B. Kay, P. R. Stysley, and D. Poulios, “Efficient, reliable, long-lifetime, diode-pumped nd:yag laser for space-based vegetation topographical altimetry,” *Appl. Opt.*, vol. 43, no. 27, pp. 5236–5242, 2004.

[110] Polyscience recirculating chiller, model 6550T 21A130E.

[111] ”Optishield plus” corrosion inhibitor by Opti Temp.

[112] R. J. S. Jr., A. J. Alfrey, and R. L. Byer, “40-W cw, TEM00-mode, diode-laser-pumped, Nd:YAG miniature-slab laser,” *Opt. Lett.*, vol. 20, no. 5, pp. 459–461, 1995.

[113] Y. Durand, A. Culoma, R. Meynart, J. L. Pinsard, and G. Volluet, “Performance of high-power laser diode arrays for spaceborne lasers,” *Appl. Opt.*, vol. 45, no. 22, pp. 5752–5757, 2006.

[114] J. Murray, “Pulsed gain and thermal lensing of Nd:LiYF$_4$,” *IEEE J. Quantum Electron.*, vol. QE-19, no. 4, pp. 488–491, 1983.

[115] D. Mudge, M. Ostermeyer, P. J. Veitch, J. Munc, B. Middlemiss, D. J. Ottaway, and M. W. Hamilton, “Power scalable TEM$_{00}$ CW Nd:YAG laser with thermal lens compensation,” *IEEE J. Sel. Top. Quantum Electron.*, vol. 6, no. 4, pp. 643–649, 2000.

[116] J. D. Mansell, J. Hennawi, E. K. Gustafson, M. M. Fejer, R. L. Byer, D. Clubley, S. Yoshida, and D. H. Reitze, “Evaluating the Effect of Transmissive Optic Thermal Lensing on Laser Beam Quality With a Shack-Hartmann Wave-Front Sensor,” *Appl. Opt.*, vol. 40, pp. 366–374, 2001.

[117] P. Webels and C. Fallnich, “Highly sensitive beam quality measurements on large-mode-area fiber amplifiers,” *Opt. Express*, vol. 11, pp. 3346–3351, 2003.

[118] E. Siegman, "How to (Maybe) Measure Laser Beam Quality," Tutorial presentation at the Optical Society of America Annual Meeting, Long Beach, California, October 1997.

[119] N. Hodgson and H. Weber, *Laser Resonators and Beam Propagation: Fundamentals, Advanced Concepts and Applications* . Springer, Berlin: Springer series in optical sciences, 2nd ed., 2005.

[120] Scientific Materials Corp. 31948 East Frontage Road Bozeman, MT 59715.

[121] BAE Systems Australia, Taranaki Road Edinburgh Parks Edinburgh SA 5111 Australia.